

**Low Cycle Fatigue Properties of
Reduced Activation Ferritic/Martensitic Steel (JLF-1)
at Elevated Temperature**

Huailin LI

DOCTOR OF PHILOSOPHY

Department of Fusion Science
School of Physical Sciences
The Graduate University for Advanced Studies

2006 (School Year)

Abstract

One of the most important tasks in the 21th century is to develop a social system in which the environment and life on a global scale are protected. Central item to this issue is the development of economical energy sources with low emission of carbon dioxide because carbon dioxide leads to global warming and may cause more critical issue of abominable global climate. On the other hand, the supplement of fossil fuels is limited. The development of advanced energy is an important option concerning stable energy source in the century.

Among the fission, fusion, and other sources such as wind power, fusion has been actively considered as the 21st century energy source in major countries to meet the energy requirement of our society in the future, because it has potentially superior characteristics with respect to safety, environment acceptability, and resource availability. The structural integrity of fusion reactor depends on the properties of the structural materials. Thus, the development of reactor materials and power generating blanket system is a critical issue for early realization of fusion energy. Among the three materials for fusion applications—reduced activation ferritic/martensitic steel (RAF/M), V-alloy, and SiC/SiC composites, the RAF/M steel is considered as the leading candidate structural material for the first wall in fusion reactor as there exists a well-developed technology and a broader industrial experience with the ferritic-martensitic steels in fossil and nuclear energy technology.

Low cycle fatigue (LCF) behavior of RAF/M steel at elevated temperatures is necessary to design since the cyclic plastic deformation might be expected if the combined mechanical and thermal cyclic loading of the first wall is extremely high. In addition, mechanical properties of martensitic steels are strongly related to their complex microstructure.

Thus, the objective of this research is to study the LCF behavior of a candidate structural material of the first wall, JLF-1 steel, at elevated temperature with an engineering size specimen in vacuum. To avoid the shape, size, and environment effects, the LCF tests were carried out with engineering size (8 mm in diameter) round bar specimens in vacuum. The present research focuseses on;

- 1) temperature effect on the relationship between fatigue life and plastic strain range,
- 2) cyclic softening/hardening and the mechanism,

3) cyclic yield stress-strain curves and its application on design. To obtain basic information on RAF/M at elevated temperature, the tensile test was also carried out.

Tensile and LCF specimens were polished in the longitudinal direction with #1500 emery paper to remove the circumferential machining layers. The test system consisted of mechanical machine (load capacity of ± 98 kN), vacuum system ($\sim 10^{-3}$ Pa), and induction heating system (capacity of up to 973 K). The axial displacement of the specimen was measured by a Shinko 1501-93-20 extensometer (a differential transducer with gage length of 12.5 mm and capacity of ± 1 mm). Based on the temperature profile on the specimen, two thermocouples were welded in the gage length on the specimen for temperature control. One thermocouple was used for the control of the temperature and the other was to monitor the temperature during the test. The temperature difference in the two thermocouples was kept less than 3 K, which was stricter than the requirement of ASTM standard.

Tensile tests of JLF-1 steel were carried out from room temperature (RT) to 873 K at strain rate of 0.1%/s and 0.02%/s. The strain rate does not affect yield stress, ultimate tensile strength and reduction in area as far as the tests performed in this study. Strain hardening of JLF-1 steel decreased significantly above 673 K, almost no strain hardening was observed at 873 K. With strain hardening decreased, the aspect of fracture changed from shear type fracture below 673 K to dimple type fracture at 773 K and 873 K. Since a little strain hardening results in lower deformation resistance at 873 K, the deformation becomes larger and larger when the stress should be over the yield point.

LCF tests of JLF-1 steel were carried out in vacuum using a fully reversed push-pull strain controlled triangular wave with strain rate of 0.1 %/s at RT, 673 K, and 873 K. The fatigue life at elevated temperature was almost as same as that at RT when the life was plotted against the total strain range. But when the life was plotted against the plastic strain range, the fatigue life curves for RT, 673K and 873 K were on different lines, which is not in agreement with the Coffin's model. The TEM images showed that dislocation structure is dependent on temperature; dislocation rearrangements keeping high density at RT, dislocation decrease to medium level at 673 K, dislocation density decrease to low level at 873 K. Loss of dislocation pile up will result in reduction of strain hardening at high temperature. So, the loss of strain

hardening will be responsible for the increase of fatigue life at high temperature when plotted against the plastic strain range.

Cyclic softening was observed during LCF test at elevated temperature in vacuum, which was strongly related to reduction of the dislocation density, formation and loss of dislocation cell structure, and increment of lath width caused by partial annihilation of original lath boundaries. The correlation of Vickers Hardness and microstructure for the present experiment is investigated to obtain mechanistic understanding on the mechanical property change such as fatigue life and cyclic softening.

The cyclic stress-strain curve can be obtained from the fatigue stress-strain hysteresis curves around half life. Strain hardening decreased significantly at 873 K. The cyclic yield point was lower than the static one, especially at 873 K, that means cyclic deformation at elevated temperature will reduce the design margin. So, cyclic yield stress-strain curve of JLF-1 steel have to be applied for fatigue design and safety analysis.

In summary, this study has demonstrated that the fatigue life was dependent on temperature when plotted against the plastic strain range, which is not in agreement with the Coffin's model. The TEM images showed that dislocation structure is dependent on temperature: at RT, dislocation rearrangements keeping high density; at 673 K, dislocation decrease to medium level; at 873 K, dislocation density decrease to low level. Loss of dislocation pile up will result in reduction of strain hardening at high temperature. The loss of strain hardening will be responsible for this phenomenon. It is also indicated that the phenomenon of cyclic softening of JLF-1 steel is a one of important issues for design, which will cause the reduction in design margin significantly. The cyclic yield stress curve is a base for design and safety analysis. The design stress of $1/3 \sigma_{UTS}$ is acceptable at 873 K.

Contents

Chapter 1 Introduction	1
1.1 World energy composition and supplement.....	2
1.2 Fusion reactor.....	3
1.3 Candidate structural materials for blanket.....	11
1.4 Mechanical properties of RAF/M steels.....	15
1.5 Low cycle fatigue at elevated temperature.....	26
1.6 Objectives of present research.....	36
Chapter 2 Experimental Procedure	37
2.1 Chemical composition of JLF-1 steel and heat treatment.....	38
2.2 Tensile and fatigue specimens.....	39
2.3 Test system.....	40
2.4 Temperature profile of specimen.....	44
2.5 Test procedure.....	46
Chapter 3 Tensile Test and Microstructural Analysis	50
3.1 Tensile test results.....	51
3.2 Effect of static deformation on microstructural change.....	55
3.3 Discussion.....	59
3.4 Summary.....	62
Chapter 4 Fatigue Test and Microstructural Analysis	63
4.1 Temperature effect on fatigue life and the mechanism.....	65
4.2 Cyclic softening and the mechanism.....	84
4.3 Hardness test results.....	90
4.4 Summary.....	95
Chapter 5 Consideration for design base	96
5.1 Effect of strain hardening on the design base.....	97
5.2 Effect of cyclic softening on the fatigue design base.....	99
5.4 Summary.....	102
Chapter 6 Conclusions	103
REFERENCE	106
LIST of PAPERS	111
LIST OF PRESENTATION	112
ACKNOWLEDGEMENTS	113

Chapter 1 Introduction

1.1 World energy composition and supplement

Our world will face the need for new energy sources as the growth of population, the absence of fossil fuels and the development of society. Figure 1.1 shows the world primary energy sources in use in 2000 [1]. Fossil fuels accounted for about 80% of the primary energy consumption, while the renewable sources of hydro and new renewable ones merely represented 4.4% of the energy consumption. Fossil fuels are sources with many problems difficult to resolve, such as environmental degradation at the local, regional and global level. Burning fossil fuels to get energy produces CO₂ and causes air pollution, resulting acid rain. The release of CO₂ causes a critical environmental issue of “green house effect”, which results in global warming and may cause more critical issue of abominable global climate.

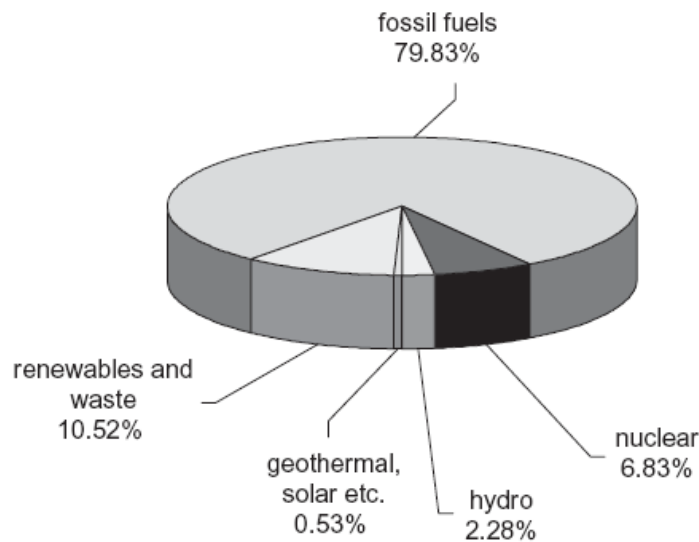


Fig. 1.1 World primary energy production by source in 2000 [1].

On another hand, the supplement of fossil fuels is limited. It was predicted by Donald L. Klass [2] that oil reserves will be used up within 20-70 years at an annual growth rate of 2.3% in consumption and 30-70 years for the natural gas at an annual growth rate of 3.2%. R. Toschi [3] reported in 1997 that the proven recoverable reserves of energy were 800, 200, 200 and 80TWY for coal, oil, natural gas and nuclear fuel, respectively, and could be used for about 300, 50, 80, 100 years at the consumption rate of the year. Thus new energy source should be found to meet the energy requirement of our society in the future.

1.2 Fusion reactor

The major energy source in the 21st century and beyond should satisfy global environmental protection requirements while being closely related to national economy and security. Among the fission, fusion, and other source such as wind power, fusion has been actively considered as the 21st century energy source in the world's major countries since fusion energy has potentially superior characteristics with respect to safety, environment acceptability, and resource availability [4]. Based on deuterium- tritium fusion reaction, there is an essentially unlimited fuel supply on the earth, deuterium from the ocean and tritium from transmutation of lithium by fusion neutron. On the other hand, global warming and acid rain will not happen as fusion will not produce CO₂ or SO₂.

1.2.1 Fusion reaction

The scheme of fusion reaction to produce fusion energy is schematically shown in Fig. 1.2.1-1 [5-8].

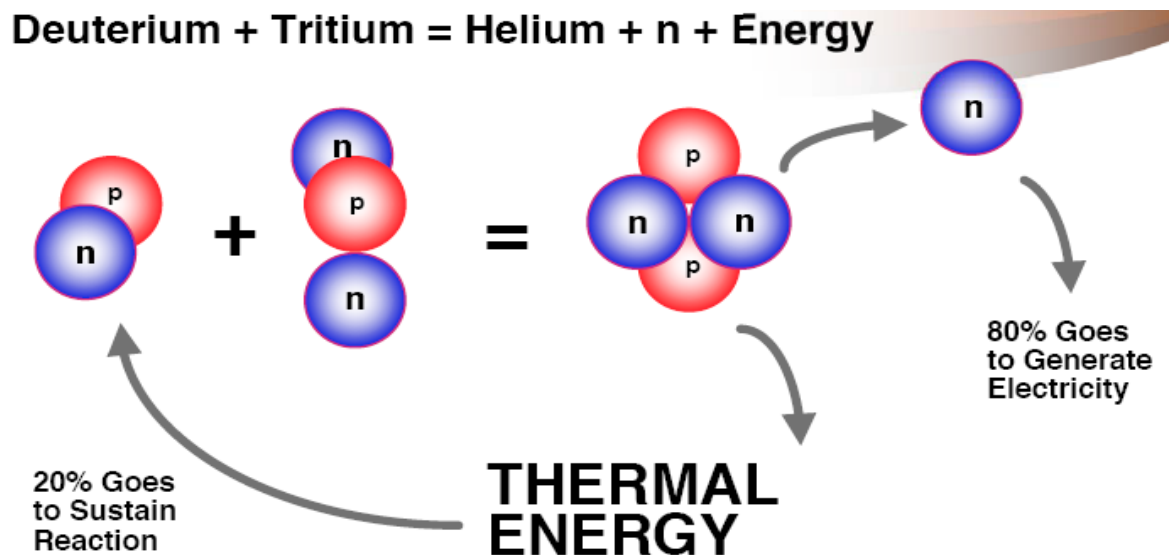


Fig 1.2.1-1 Scheme of D-T fusion reaction [6].

In contrary to fission, fusion reaction leads two light nuclei into one heavier nucleus with the release of substantial amounts of energy. There are many kinds of fusion reaction,

practical ones for energy on earth are shown on Fig. 1.2.1-2. The most suitable reaction occurs between the nuclei of two isotopes of hydrogen, deuterium (D) and tritium (T), at relatively the lowest ignition temperature since D-T reaction has the largest fusion cross-section among the reactions [8].

The mass loss is only 0.38% of the initial reactants for the D-T reaction. According to Einstein's famous equation,

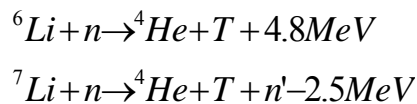
$$E = Mc^2 \quad (1.2.1-1)$$

where E is energy, M is mass and c is the speed of light (3×10^8 m/sec.), the total energy output for the D-T reaction is 17.6 MeV with 14.1 MeV carried by the neutron and 3.5 MeV by ^4He [7]. So the D-T reaction could be written as:



At the temperature required for the D-T fusion reaction, the fuel has changed its state from gas into plasma in which the electrons have been separated from the atomic nuclei and move freely. For the fusion reaction, the two nuclei of D^+ and T^+ should have very high kinetic energy enough to overcome the electrostatic repulsion between the two nuclei.

The fuels of fusion reaction, D and T, are essentially inexhaustible. D could be easily extracted from seawater. The D content in seawater is about 30 ppm, that is, one liter of seawater contains about 0.03 g deuterium. The total volume of the seawater on the earth is about 13.7 billion cubic km, thus the D in the seawater is in the level of several billion billion kg. Tritium is a low-energy beta emitter with a half-life of 12.4y and thus there are few resources on the earth. However, it can be bred by causing the n released by the D-T reaction to interact with isotopes of lithium as follows [8]:



Natural lithium consists of about 93% Li^7 and 7% Li^6 , and there is abundant Li in the earth's crust.

Besides D-T reaction, other reactions also receive attentions for possible energy

application (Fig 1.2.1-2) [6,7]. The D-D reaction eliminates the need for tritium breeding but has much higher ignition temperature and requirement for strong plasma energy confinement. Therefore it will require either a larger system or a more powerful method of plasma confinement. D-³He has a somewhat larger reaction cross-section, lower ignition temperature than D-D but is more difficult to use than D-T. The major concern is for the actual source of ³He fuel. This isotope is found in very small quantities on earth but there are adequate supplies in the near-surface crust of the moon due to deposits from solar wind over the ages. The feasibility and cost of recovery of such resources are serious issues. Other fusion reactions involving lithium have marginal or even negative net energy yields and are highly questionable as practical fusion power reactions [9].

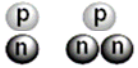
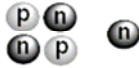

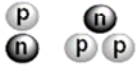
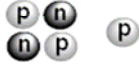

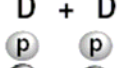
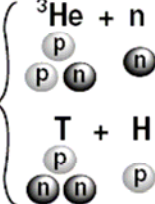


Reaction		Output Energy	Typical Fusion Temperature
Fuel	Product	(keV)	(millions of °K)
$D + T$ 	${}^4\text{He} + n$ 	 17,600	~50
$D + {}^3\text{He}$ 	${}^4\text{He} + p$ 	 18,300	350
$D + D$ 		 3,250	400
		 4,000	400

Fig 1.2.1-2 Fusion ignition temperature and output energy at different fusion action [7].

Fusion energy is clean and safe [9]. Different from fission reaction, fusion reaction in a device will stop immediately in case of an accident because in such case the fuel (plasma) will cool down rapidly. The waste gas of the fusion reaction is helium that is an inert gas without any impact on the environment, and does not cause greenhouse effect. And yet, no products of radioactive waste like that produced by the fission fuels. Another product of fusion reaction is

the 14MeV energetic neutron, which is the source of the fusion energy and is stopped in the blanket of a fusion reactor. It has little impact on the environment. The reactor wall will be activated by the neutron and the material becomes radioactive, but the half-life is many orders-of-magnitude lower than fission products. The radioactivity can be minimized by careful selection of low-activation structural materials.

1.2.2 Fusion reactor

There are two ways, Magnetic Confinement Fusion (MCF) and Inertial Confinement Fusion (ICF), to achieve the controlled reactions to produce electric power on earth [7,10].

- 1) MCF involves that ionized (charged) nuclei are controlled by so much strong magnetic field that the nuclei will orbit around the field line, gradually processing along it if the nuclei has some longitudinal velocity.
- 2) ICF uses intense energy beams (high-energized particle or laser) to compress and heat the tiny pellets in a reaction chamber, which will raise the temperature and density to sufficient condition of a fusion reaction.

These two methods have large difference in the standpoint of physics or engineering. The most promising approaches for fusion power is the MCF concept. Here only the introduction and study concerning MCF are mentioned. One of the promising confinements that mostly studied is the tokamak concept. In a tokamak device the magnetic field confines the plasma within a torus vessel and keeps the high-temperature plasma away from the vessel wall. The research on tokamak principle have been performed widely and got many achievements, such as TFTR in the U.S [11,12], JET in Europe [13] and JT-60U in Japan [14], et al. Now a tokamak type International Thermonuclear Experimental Reactor (ITER) is under design and is expected to have its first plasma at 2016 [5, 15-20]. Figure 1.2.2-1 shows the cutaway of ITER. The function of parts or system in ITER is as follow;

- 1) first wall and blanket absorb heat radiating from plasma, provide neutron shielding,
- 2) diverter exhausts the flow of energy from charged particles produced in fusion reactions and remove helium and other impurities,
- 3) vacuum vessel provide high vacuum boundary for the plasma and the first line of confinement against radioactive release within the vessel,

4) superconducting magnet systems, including the toroidal field (TF) coil, poloidal field (PF) coil and central solenoid (CS) coil, produce a strong magnetic field to confine the plasma,

5) cryostat keeps ultra-low temperature to superconducting magnet.

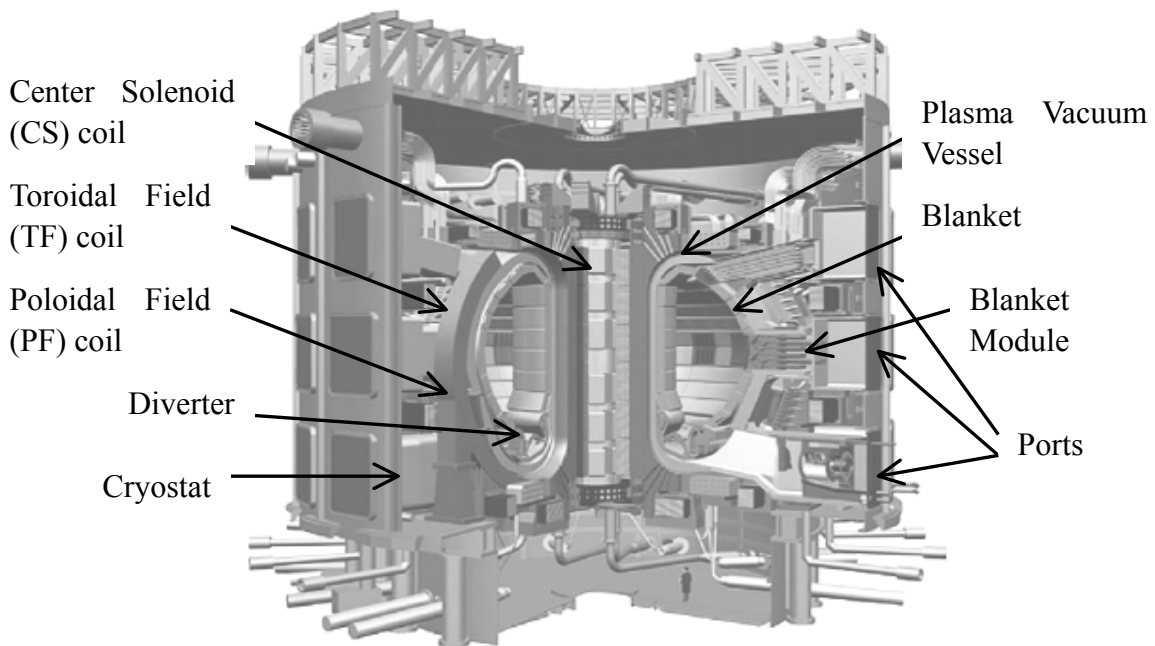


Fig. 1.2.2-1 ITER Tokamak cutaway [15].

The objectives of ITER are to demonstrate ignition and extended burns of D-T plasmas with steady-state as an ultimate goal, demonstrate the integration of technologies for reactors and serve as a test facility for advanced components such as blankets [21]. The fusion power is designed to 500 MW with a pulse mode operation [21-23].

Table 1.2.2-1 shows the general parameters of the future fusion devices [24], based on present knowledge in plasma and fusion technology. ITER is just an experimental reactor while the other two are reactors for power plants. In comparison, ITER has much lower fusion power and neutron wall load. For future fusion power reactors, the neutron wall load would be high up to 3 MW/m^2 , and hence advanced structural materials should be used. The integrated neutron wall load and the derived displacement damage will limit the lifetime of reactor components.

Table 1.2.2-1 General performance parameter for fusion devices [24].

	ITER	DEMO*	REACTOR
Fusion Power, GW	0.5-0.7	2-4	3-4
Neutron wall loading (first wall), MW/m ²	0.57-0.78	2-3	2-3
Integrated wall load (first wall)			
In MWy/m ²	~0.3-1	3-8	10-15
In displacements per atom (dpa)	1.7-5.5	30-80	100-150
Operation mode	Pulsed	Quasi-continuous	

DEMO: Fusion power demonstration reactor.

1.2.3 Blanket system

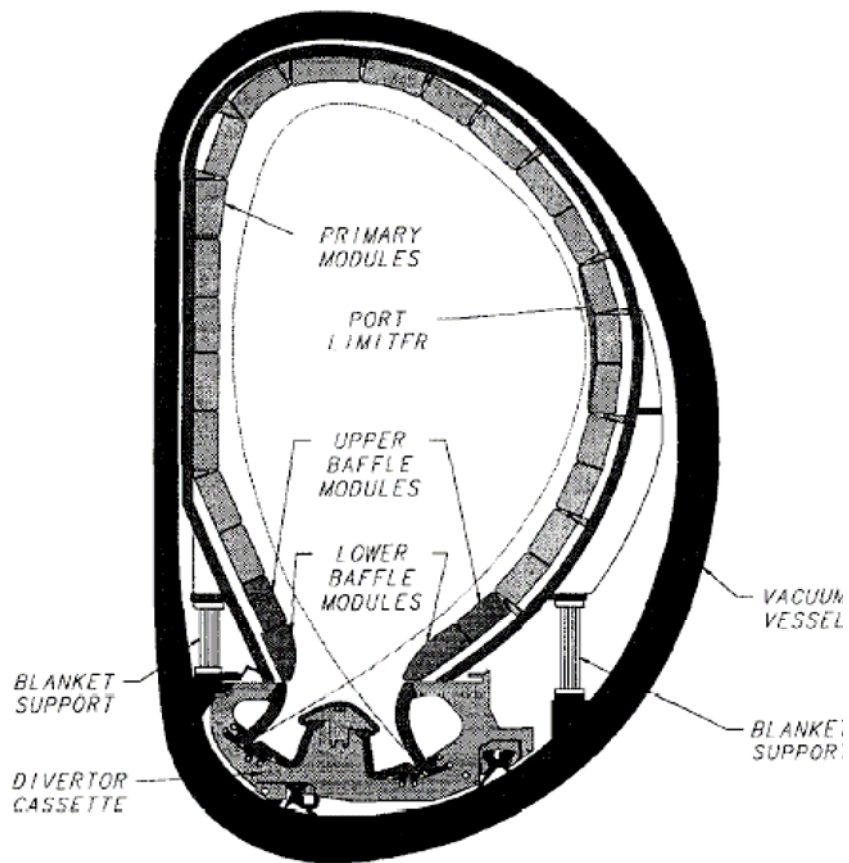


Fig. 1.2.3-1 View of ITER vacuum vessel [25].

The blanket is located between the plasma and vacuum vessel (Fig. 1.2.3-1). In the Basic

Performance Phase (BPP), ITER adopts a shielding blanket to provide the main thermal and nuclear shielding to the vessel and external machine components [25].

The breeding blanket concept in design is dependent on a number of parameters, such as neutron flux, safety, availability, tritium breeding ratio etc [26]. Based on these parameters, the materials selection and structure design can be performed.

The ITER blanket is operated at a low temperature (423-523 K) and lower integrated wall loading. Type 316LN austenitic steel is main structural materials for the ITER vacuum vessel and in-vessel components (shielding blanket, divertor cassette body) [27]. However, the maximum irradiation dose for type 316 stainless steel is about 5-7 dpa (for neutron wall loading about 1MW/m²) within the operation temperature range of ITER [28]. For DEMO and future reactor, the irradiation dose and operation temperature are higher than that in ITER (Table 1.2.2-1) [24,29], void swelling should be considered for type 316 stainless steel in such rigorous condition. So the type 316 stainless steel cannot be applied to design high power density blanket as its low thermal conductivity.

Several fusion reactor blanket concepts for DEMO were developed and will be tested and irradiated in ITER (Table 1.3.2-1). All of them could be classified with regard to the breeding materials into two categories [29-34]; solid ceramic and liquid metal breeders with the options of self-cooled or separately cooled versions.

Table 1.2.3-1 Major breeding blanket concepts [26, 29-34].

	Coolant	Tritium Breeder	Structural material	Neutron multiplier	Operation Temperature (K)
LiCe/FM/Be	He/H ₂ O	Li-ceramic	F/M	Be	523-823
LiCe/SiC/SiC/Be	He	Li-ceramic	SiC/SiC	Be	723-1223
Li/V	Li	Li	V-alloy	Li	623-1023
Pb-Li/FM	Pb-Li /H ₂ O	Pb-Li	F/M	Pb-Li	523-823
Flibe/FM	Flibe	Flibe	F/M	Be	723-823
Flibe/V	Flibe	Flibe	V-alloy	Be	823-973

LiCe – Lithium ceramic breeder materials such as Li₂O, Li₄SiO₄, Li₂ZrO₃ and Li₂TiO₃.

F/M: Ferritic/Martensitic steels.

Flibe: BeF₂+LiF.

The maximum temperature is limited by high temperature creep-rupture strength of structural material and/or its corrosion resistance to breeding materials or coolant. The possible low temperature or coolant inlet temperature is limited by irradiation hardening and embrittlement of structural materials. The thermal efficiency increases with the increase of the upper operation temperature, and could be further increased by use of more advanced material/technology and blanket concept.

The structural integrity depends on the properties of the structural materials. So, development of reactor materials and power generating blankets is a critical issue for early realization of fusion energy.

1.3 Candidate structural materials for blanket

1.3.1 Requirement for structural materials

The long-term goal of fusion materials researches is to develop structural materials that will permit fusion to be developed as a safe, environmentally acceptable, and economically competitive energy source. The safety of fusion power plant depends on the following items [35].

- 1) The structural integrity of the plant and the probability of its failure;
- 2) The radioactive decay heat generated in the absence of coolant; and
- 3) The paths for dispersion of radioactivity to the plant surrounding during accident.

The structural materials of the first wall in D-T tokamak reactor during service are subjected to the following [35-38].

- Mechanical and electromagnetic loading and alternating thermal stresses induced by the surface and volumetric heating and pulsed nature of operation.
- Irradiation with high energy (14.1 MeV) fusion neutrons producing displaced atoms and helium, hydrogen, and solid transmutation products, leading to changes in bulk properties.

Thus, the requirements for structural materials of the first wall of blanket in a fusion reactor is more difficult than that for any other energy system [4], including high fluxes of high energy (14MeV) neutrons, high surface heat fluxes and high temperature coolants and breeding materials. The blanket systems are large systems with combined thermal, hydraulic and mechanical loading, irradiation, corrosion etc. The common requirements for fusion structural materials are the followings [9].

- 1) The material could withstand high neutron wall loads under temperatures and coolant pressure conditions necessary to drive efficient thermodynamic cycles in a blanket.
- 2) The lifetime of structural material must be long enough to minimize the necessary replacements of near-plasma components.
- 3) The material should be of low activation in order to achieve the ultimate environmental attractiveness of fusion power.

It is the special requirement in the fusion reactor that the structural materials should be

"low activation" [4]. The fusion reaction does not produce radioactive nuclides. Any radioactivity produced in a fusion reactor derives from capture of neutrons in the structural materials, coolant, or tritium breeder. This leads to important potential advantages of fusion relative to fission in the key areas of safety and environmental impact and relative to fossil generation in the area of environmental impact. By careful selection of the chemical elements, the amount of long half-life radioactivity of structural materials can be reduced to the point that the materials are innocuous after as little as a 50 or 100 years decay period. Recycle of materials, which would tremendously reduce the amount of radioactive waste to be disposed of, may be a possibility.

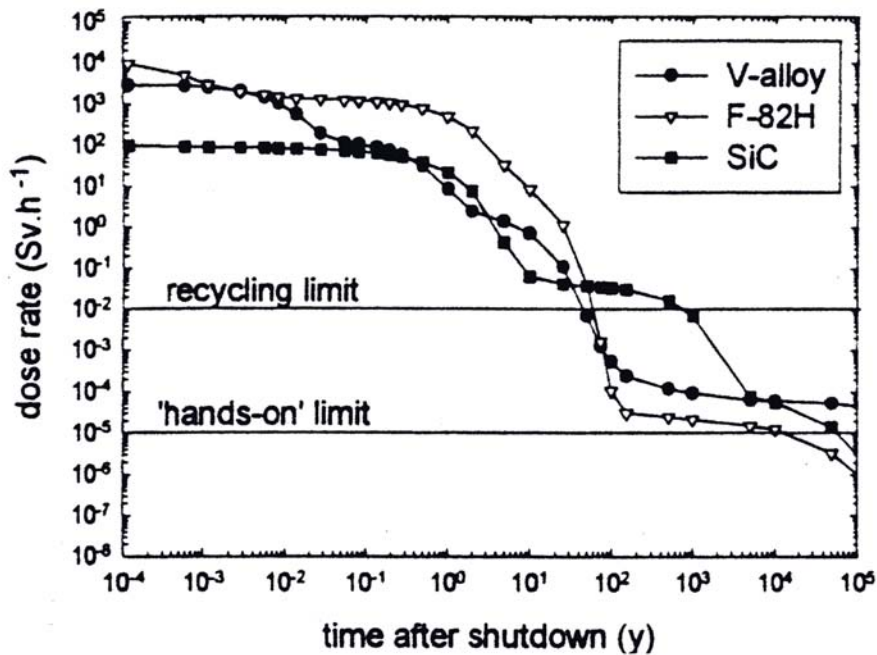


Fig. 1.3.1-1 Comparison of γ -dose rate for F82H, V-alloy and SiC/SiC composites [35].

There are reduced activation ferritic/martensitic (RAF/M) steels (F82H, JLF-1 and Eurofer 97 etc.), V-based alloys, and SiC composites for near-, mediate- and long-term applications in fusion reactor [36]. The level of long-term activation (γ -dose rate) for F82H, V-4Ti-3.3Cr and SiC/SiC composites, which determines the way of waste disposal and recycling after intermediate storage, is shown in Fig. 1.3.1-1. After 100 years decay time, γ -dose rate is in the range of low-level waste (less than 10 mSv/h) and can be recycled by

remote handling method. Especially V-alloy and RAFM steel have a potential to reach the hand-on limit (10 $\mu\text{Sv/h}$) within 100-1000 years.

1.3.2 Candidate structural materials for blanket

The initial choices for candidate low activation structural materials, SiC/SiC composites and V–Ti–Cr alloys, were developed in the United States in the early 1980s. Subsequently the possibility of developing RAF/M steel based on the idea of substituting W for Mo and using V and/or Ta in place of Nb as the carbide forming element(s) was developed [27]. Successful development of these materials will provide significant improvements relative to conventional materials.

SiC/SiC composites, developed for aerospace application and fossil power generation plants, are the activation material with potential for very high operating temperature because of their high temperature strength, strength to weight ratio and high corrosion resistance [39, 40]. However, SiC/SiC composites are still the least developed of the three candidate materials because of its remaining several critical issues. The remaining issues include the low thermal conductivity of most commercially available products, high-strength joining techniques leading to a high difficult for hermetic seals, chemical compatibility with potential liquid coolants, the need to develop engineering structural design criteria for ceramics, and so on. There are also concerns regarding high present-day fabrication costs and the limited industrial technology base for production of large-scale SiC composites [38, 40, 41].

Vanadium alloys are another attractive candidate materials for fusion reactor structure components due to their high-temperature strength, high thermal stress factor, and low induced activation characteristic [37,42]. V-4Cr-4Ti ternary alloy is considered to be a leading candidate material, especially the NIFS-HEAT shows various benefits by reducing the level of oxygen and other trace impurities [42]. Much of recent research has focused on vanadium alloys containing 4-5% Cr and 4-5% Ti, but a number of alternative composition and processing routes have been explored in an effort to achieve improved performance [43, 44]. There are several critical issues for the alloys used in a self-cooled blanket. The main one is the development of insulator coating to mitigate MHD pressure drop effects in liquid lithium coolant channels. Additional topics where further work is needed include investigation

of possible engineering solutions to the high tritium permeability in vanadium alloys, determination of irradiation creep behaviors at 674-973 K and the fundamental deformation mechanisms that control high temperature thermal creep, and the incomplete understanding of the influence of interstitial impurities such as C, N and O on tensile, creep and fracture properties. The lack of a widespread commercial infrastructure for production of vanadium alloys is also of concern [38, 45].

RAF/M steels, developed from 9-12% Cr with 1% Mo steel, are candidate materials for fusion reactor as its inherently good dimensional stability under intense irradiation conditions, and the chemical composition of such steels is suitable for commercial production of a reduced-activation composition without a large industrial investment [46-48]. Creep strength of 9-12% Cr steel is adequate to 823 –873 K, and they have been used at these temperature in power-generation and chemical and petrochemical industries. The technology for production and fabrication of 9-12% Cr steel exists. A major issue of this material is the radiation induced hardening/embrittlement and degradation of fracture properties [38].

Of the three materials for fusion applications, RAF/M steels are furthest in development. There exists a well-developed technology and a broad industrial experience with the ferritic-martensitic steels in fossil and nuclear energy technology. Also RAF/M steels have the advantage for construction of massive structure of a fusion power plant based on the past experience of the commercial 9-12% Cr steel. For both Vanadium alloys and SiC/SiC composites, the technique for constructing of such structure must still be developed.

Thus, the RAF/M steel is considered as the leading candidate structural material for the first wall in fusion reactor. To qualify and finally validate the application of RAF/M, a sufficient design database must be accumulated, including code approval aspects.

1.4 Mechanical properties of RAF/M steels

1.4.1 Development of RAF/M steels

The 9-12% Cr martensitic steels were originated in 1912 with the manufacture of 12% Cr-5% Mo steel for steam turbine blades in Germany [35]. Subsequently, the 9-12% Cr steels with lower carbon (0.1% max.) contents and additions of Mo, W, V, Nb, N and other elements, possessing higher creep-rupture strengths combined with good oxidation and corrosion resistance at elevated temperature, have been developed and used in petrochemical and chemical plant, gas turbine engineering, aircraft and aerospace industries, electrical power plants, and nuclear fission plants.

The 9-12% Cr ferritic/martensitic steels were introduced into the fusion materials programs about 30 years ago, after research in fast reactor programs demonstrated their superior swelling resistance and excellent thermal properties compared to austenitic stainless steels. But two types of problem are of concern with the use of a ferromagnetic material in the high magnetic field of fusion reactor:

- 1) The effect of the field perturbation caused by the ferromagnetic material on the plasma.
- 2) The magneto-static force on the ferromagnetic structure due to the magnet field.

Calculations showed that the field perturbation was small. The magnetic stress on ferritic steels was small but not negligible, and it was concluded that they must be incorporated in the stress analysis of design [35, 49, 50].

The first steels considered were conventional 9% and 12% Cr - Mo steels. Because of long radioactive decay times for some activated species in the steels (e.g., molybdenum and niobium), reduced-activation ferritic/martensitic steels has been developed in the 1980s in the EU, Japan, Russia and the US [38, 45-48].

The objective is to maximize the safety advantages of fusion and enable material and components maintenance, waste management and recycling scenarios to be established [51, 52]. The principal in this development are as follows:

- The replacement of radiologically undesirable Mo, Nb and Ni in the exiting commercial steels by elements such as W, V, Mn, Ta, and Ti, which have equivalent

or similar effects on the constitute and structure.

- The removal of the impurities that adversely influence the induced activities and dose rates when present in low concentration in the steel.

Since Fe–Cr–Mo steels were candidates for cladding materials in LMFBR, extensive irradiation database is available, which is useful for screening the Fe–Cr–W alloys. Based on a series of irradiation tests [52,53], 8–9% Cr was selected as an optimum level (see section 1.4.3). The comparative tests with Fe–Cr–Mo and Fe–Cr–W steels showed that the alloy properties of Fe–Cr–W were similar or superior to those of Fe–Cr–Mo. Especially, Fe–Cr–W steels were shown to have less shift of DBTT induced by irradiation compared to Fe–Cr–Mo steels (Fig. 1.4.1-1) [54].

Many kinds of composition of RAF/M were investigated in the European, US, and Japan. The development history of RAF/M is shown as bellow.

1960's : 9Cr-1Mo (British 9 Cr)

1970-80's: 9Cr-1MoNbV (ORNL, USA)

1980's: MANET (EU, 10Cr)

1980-90's: RAF/M (Rapid decay to recycle limits or hands-on limits, no Mo and Nb)

F82H (Japan, 8Cr-2W)

9Cr-2WVTa (USA, 9Cr-2W)

JLF-1 (Japan, 9Cr-2W)

Eurofer 97 (EU, 9Cr-1W)

The composition of the RAF/M steels, which appear to have stable microstructure and favorable combination of strength, toughness, and resistance to radiation damage, are summarized in Table 1.4.1-1.

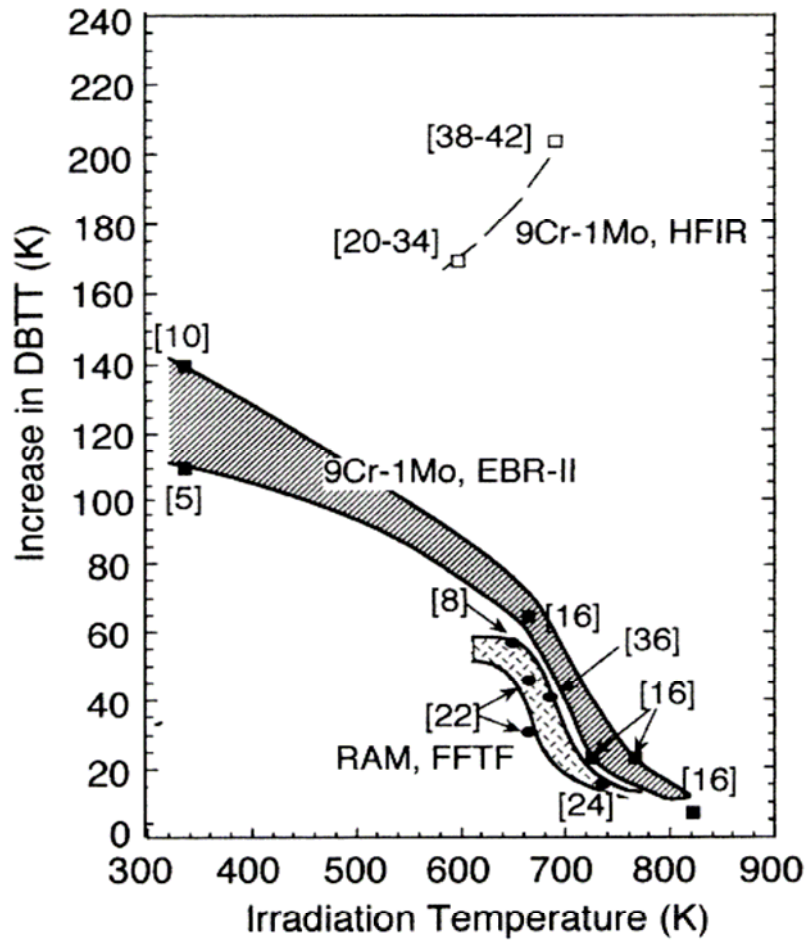


Fig. 1.4.1-1 Irradiation temperature effect on DBTT in ferritic steels [54]
 (The bracketed number indicate the dose in dpa).

Table 1.4.1-1 Typical composition (wt%) of RAF/M with favorable properties.

	C	Si	Mn	Cr	V	Ta	W	N	B	Ref.
F82H	0.10	0.20	0.50	~8.0	0.20	0.04	~2.0	<0.01	0.003	52,55,56
JLF-1	0.10	0.08	0.45	~9.0	0.20	0.07	~2.0	0.05		52,57,58
EUROFER	0.10-0.120	0.05	0.4-0.6	8.0-9.0	0.20-0.30	0.06-0.10	1.0-1.2	0.02-0.04	0.004-0.006	52, 59
9Cr-2WVTa	0.10	0.30	0.40	~9.0	0.25	0.07	~2.0			52, 60

1.4.2 Martensitic phase transformation

The 8-9% Cr steels are austenitic structure at austenitizing temperature in the range of 1123 K to 1473 K (850 to 1200°C in Fig. 1.4.2-1). The austenite phase transforms to martensite

during air cooling or rapid quenching to ambient temperature (Fig. 1.4.2-2), and the steels are subsequently tempered to obtain a good combination of strength, ductility, and toughness.

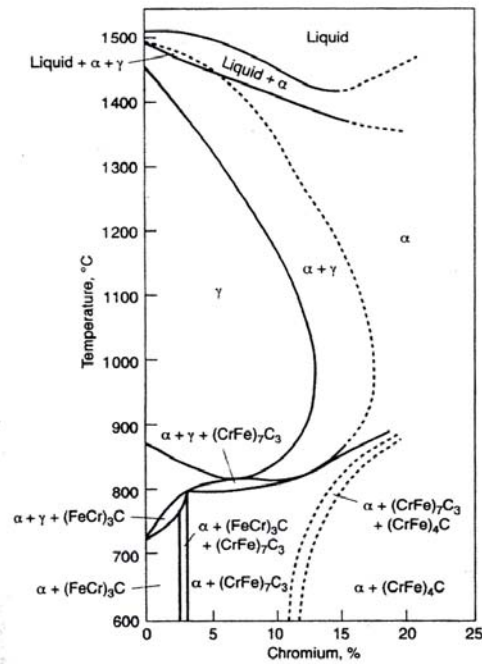


Fig. 1.4.2-1 Effect of Cr on Fe-Cr-C alloy containing 0.1% C [35].

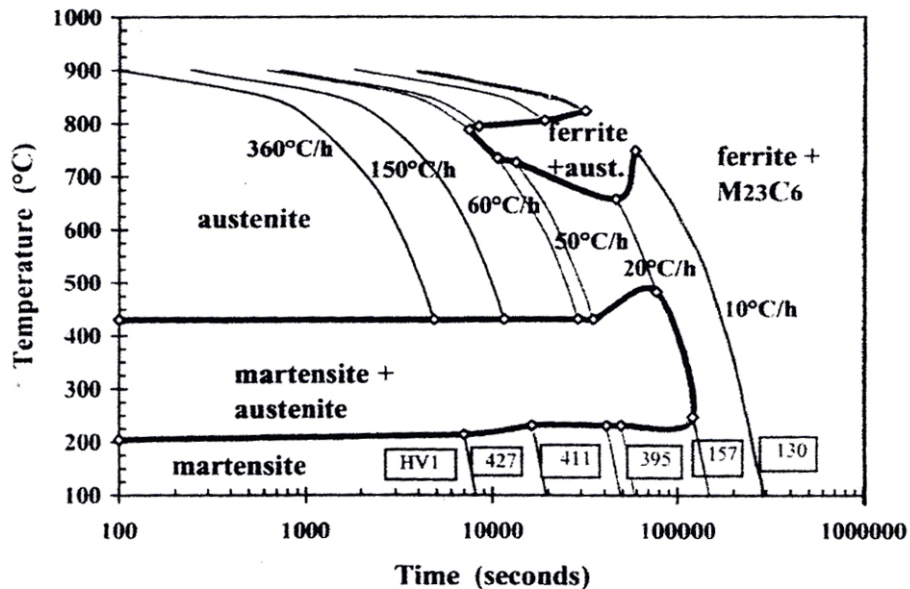


Fig. 1.4.2-2 Continuous cooling transformation (CCT) diagram for low carbon 7.5Cr-2WVTa (F82H) steel determined after austenitization at 1323 K for 0.5 h [61].

The martensitic transformation is a diffusionless phase transition in the solid state with a large deviatoric component, which proceeds by the nucleation and growth of the new phase. From the viewpoint of thermodynamics, the free energy is decreased during the transformation from austenite to martensite [62,63]. The relationship between free energy of austenite (γ) and martensite (M) phases with temperature is shown in Fig. 1.4.2-3. At temperature of M , the transformation is happened, the driving force is the energy difference between austenite and martensite:

$$\Delta G_{\gamma \rightarrow M} = G_{\gamma} - G_M \quad (1.4.2-1)$$

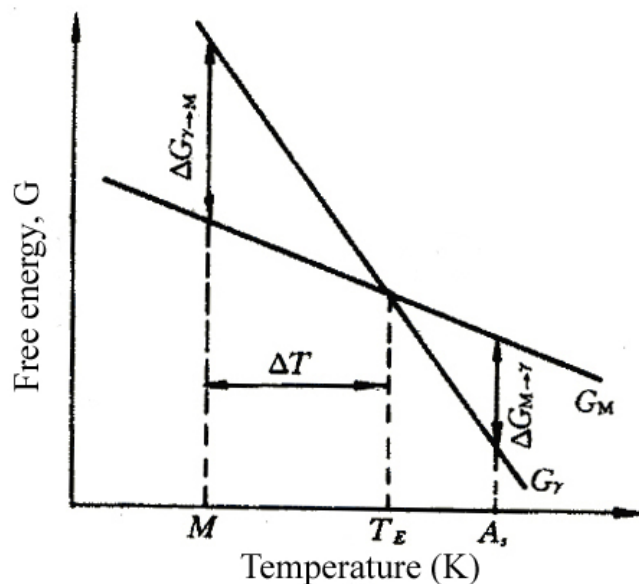


Fig. 1.4.2-3 Chang in free energy of γ and M phases with temperature [62].

The precise atomistic mechanism for the nucleation and growth of the martensite is unclear. Different models have been advanced for this in conventional martensites. But the fundamental is Bain mechanism [62]. The change in crystal lattice is shown in Fig. 1.4.2-3. The steels have a close-packed face centered cubic (fcc) structure at austenitizing temperature. On cooling this structure becomes unstable and transforms to a body-centered cubic (bcc) lattice as required by thermodynamics. The elementary bcc cell is a cube with the atoms on

the corners and with an additional atom in the center. The transformation from fcc to bcc can be considered as a homogeneous distortion. This can be made clear by Fig. 1.4.2-4. In this figure are drawn two fcc cubic cells, and within them a smaller cell containing an atom in the center. This is a body centered tetragonal (bct) cell. By a homogeneous compression in the vertical direction, indicated by the arrows, and an expansion in the plane normal to it, a cubic bcc lattice is created without the need to change the volume of the bct cell.

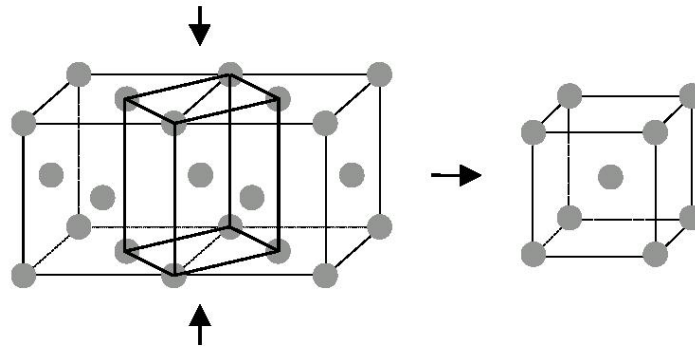


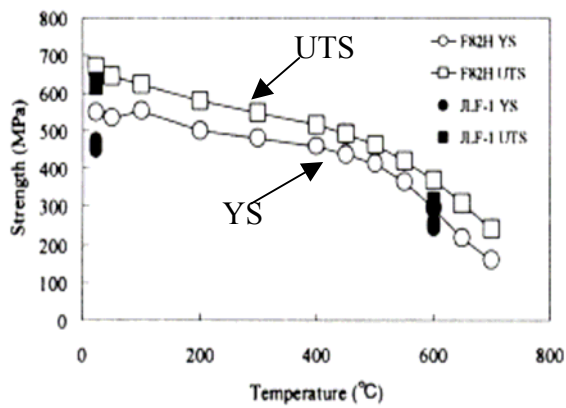
Fig. 1.4.2-4 Change in lattice structure during martensitic transformation [63].

Iron is the base of the steels that have good characters due to their strength and hardness. This is due to the presence of the small carbon atoms. They find sufficient space in the interstitial sites between the iron atoms in the fcc structure and therefore dissolve easily in large quantities at high temperatures. When this fcc ‘austenitic’ lattice transforms martensitically at sufficiently high cooling speeds to the bcc structure, the space for the carbon atom is reduced, and the carbon, having no time to diffuse to more convenient sites produces a high degree of distortion around it which makes the alloy very hard.

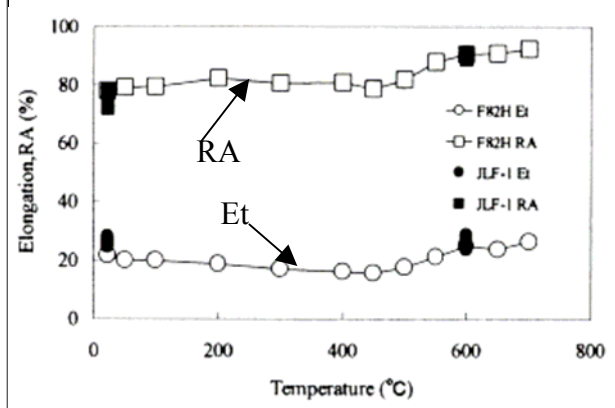
1.4.3 Basic mechanical properties of RAF/M

1.4.3.1 Tensile test results

The tensile results were reported in [52, 58, 64-69]. The tensile properties of JLF-1 and F82H are shown in Fig. 1.4.3.1-1, there were little difference in yield stress (YS), ultimate tensile strength (UTS), total elongation (Et) and reduction in area (RA) [58, 64].



(a) YS and UTS of JLF-1 and F82H.



(b) Et and RA of JLF-1 and F82H.

Fig. 1.4.3.1-1 Tensile property of JLF-1 and F82H [58,64].

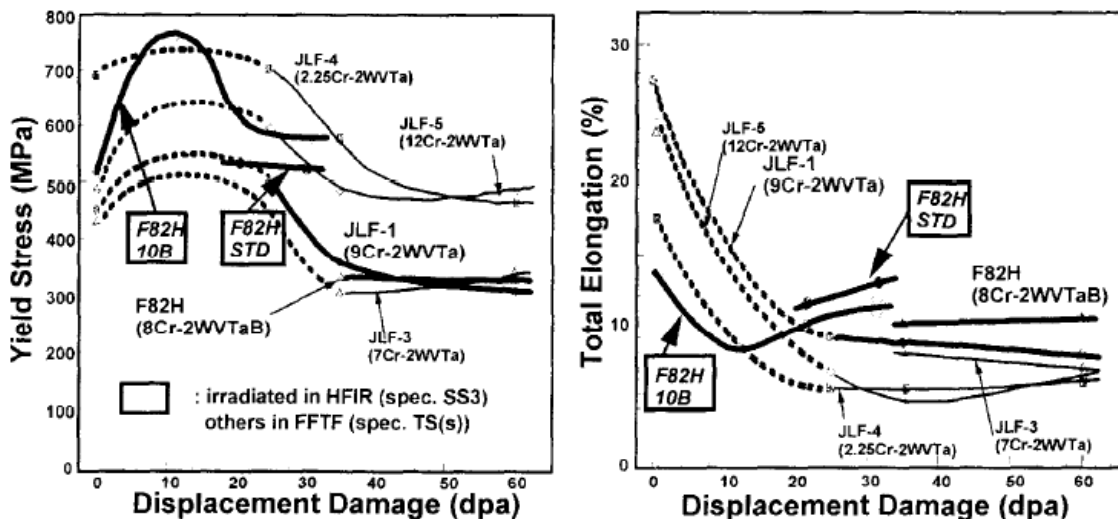


Fig. 1.4.3.1-2 Dose dependence of YS and Et following irradiation at 673 K [52].

Fig. 1.4.3.1-2 shows the irradiation effect on YS and Et at 683 K in FFTF/MOTA (Fast Flux Test Facility/Materials Open Test Assembly) and HFIR (High Flux Isotopic Reactor). Both JLF-1 and F82H showed rapid irradiation hardening in the early stage of displacement damage. Above 20 dpa, irradiation hardening decreased and then saturated at a lower strength level [52]. One explanation for the maximum in strength with the influence is that beyond the peak strength irradiation-enhanced softening (recovery) has proceeded [35].

The tensile results of EUROFER 97 without irradiation were reported in reference[67-69]. The UTS and Et of EUROFER 97 was similar to that of F82H.

1.4.3.2. Impact test results

Fig. 1.4.3.2-1 shows the charpy impact test results of JLF-1 and F82H. Little difference was observed between them.

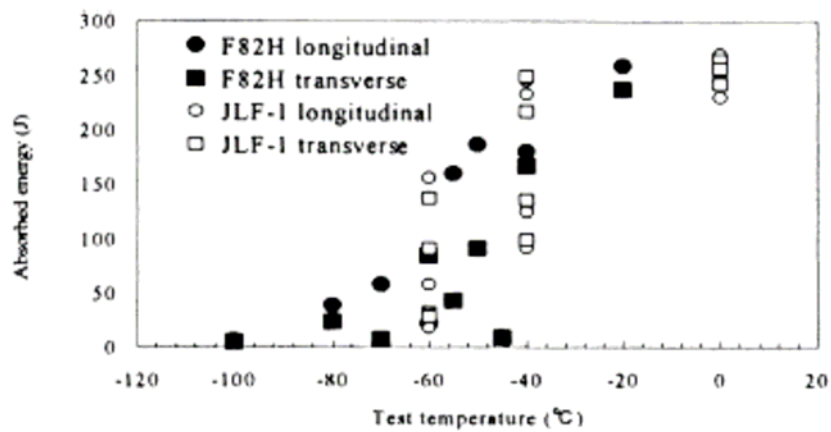


Fig. 1.4.3.2-1 Charpy impact properties compared with F82H [58].

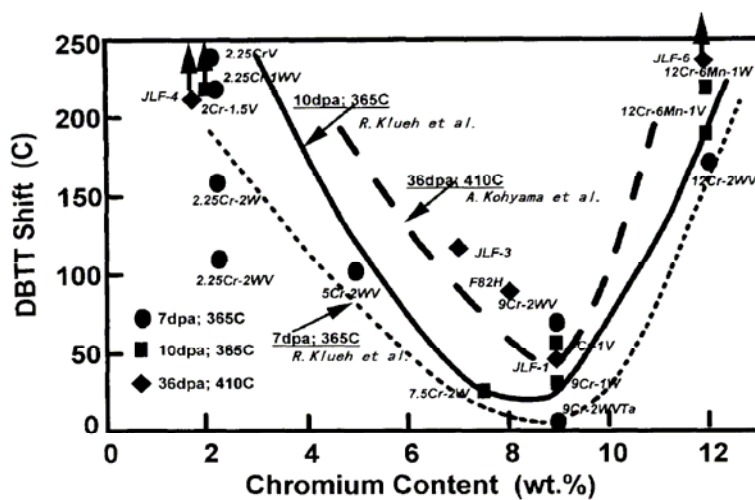


Fig. 1.4.3.2-2 Effect of Cr content on DBTT shift of RAF/M irradiated in the FFTF [52].

Fig. 1.4.3.2-2 shows the effect of Cr composition on the DBTT shift for Fe-CrWVTa

steels of various composition after irradiation in FFTF [52]. It appeared that there was a minimum in DBTT shift in the vicinity of 9 Cr. At the same time, the addition of W, V and Ta could reduce the DBTT shift in irradiation.

1.4.3.3 Creep test results

Fig.1.4.3.3-1 shows creep rupture strength of JLF-1 and F82H. The properties of JLF-1 was similar to those of F82H [58].

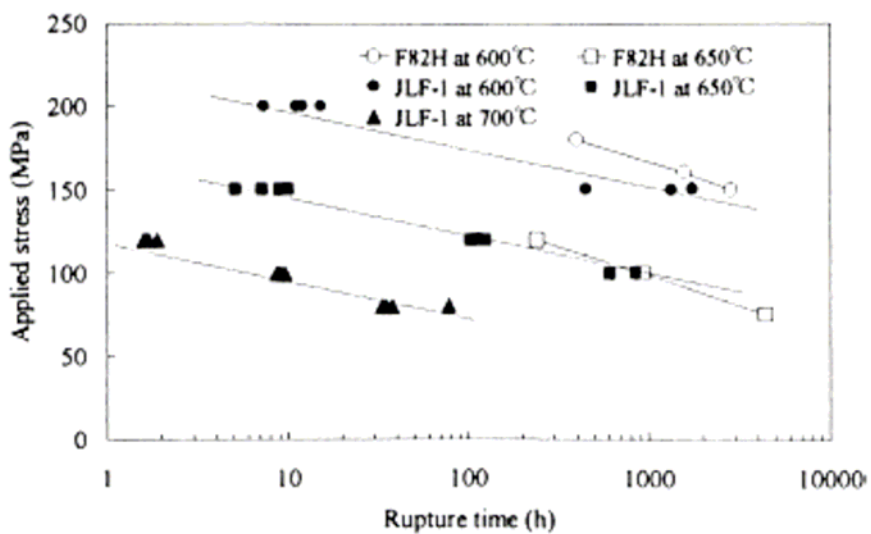


Fig.1.4.3.3-1 Creep rupture strength of F82H and JLF-1 [58].

Fig.1.4.3.3-2 shows average creep coefficient (B) for JLF-1 and F82H as a function of irradiation temperature to maximum dose of 62 dpa. The difference between F82H and JLF-1 at 793 K (520 °C) was concluded to be due to the lower tantalum and nitrogen in F82H compared to JLF-1. The higher coefficient for F82H at 873 K (600 °C) is due to the dominance of thermal creep [70].

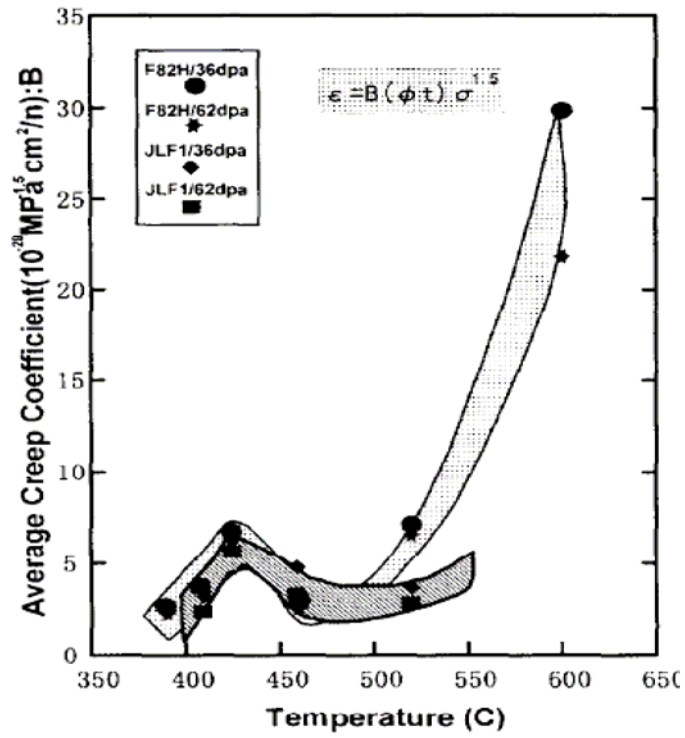


Fig.1.4.3.3-2 Temperature dependence of the average creep coefficient (B) for F82H and JLF-1 [52, 70].

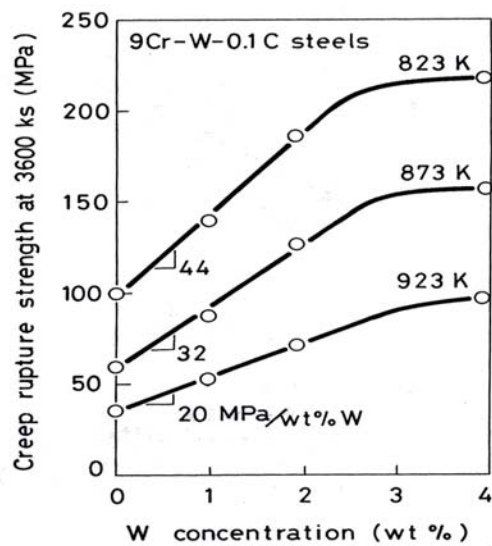


Fig. 1.4.3.3-3 Creep rupture strength of the 9Cr-W-0.1C as a function of W concentration [71].

The effect of tungsten on creep behavior of 9Cr-W-0.1C steels was investigated in reference [71]. The creep rupture strength of the steels was shown in Fig. 1.4.3.3-3 as a function of W concentration, the strength increase linearly when W concentration was lower than 3% where is the region of tempered martensite. When the W concentration is above 3%, the tendency of creep rupture strength was decreased because the steel consisted of tempered martensite and δ -ferrite.

Overall mechanical test results suggested that 9Cr-2W (JLF-1) steel has the best performance under irradiation, so JLF-1 is strong candidate of low activation ferritic/martensitic steel as a future fusion structural material at present.

1.5 Low cycle fatigue at elevated temperature

1.5.1 Fatigue

The most common type of mechanical failure is caused by fatigue, which means a machine part or a whole structure is loaded by cyclic external stress or strain, and a complete fracture may occur [35,72].

Fatigue tests are controlled either by stress (load) or strain (displacement). The majority of the early studies of metal fatigue were based on stress control testing, which is still adopted for design situation within elastic range and resulting endurance is high [high cycle fatigue (HCF)], fatigue life is over 10^5 cycles. However, the strain-controlled test is applied in design and evaluation of components whenever the load is high as in the vicinity of the notches where plastic deformation is significant. In this case, the response of the material is deformation dependent, the ductility is the dominant factor governing the fatigue behavior, and the number of cycles to failure is low [low cycle fatigue (LCF)], fatigue life is in the region $10^2 \sim 10^5$.

Fig. 1.5.1-1 shows the stress-strain hysteresis curve of LCF test, from which the total strain range ($\Delta\varepsilon_t$), plastic strain range ($\Delta\varepsilon_p$), elastic strain range ($\Delta\varepsilon_e$), total stress range ($\Delta\sigma$) and peak stress could be obtained.

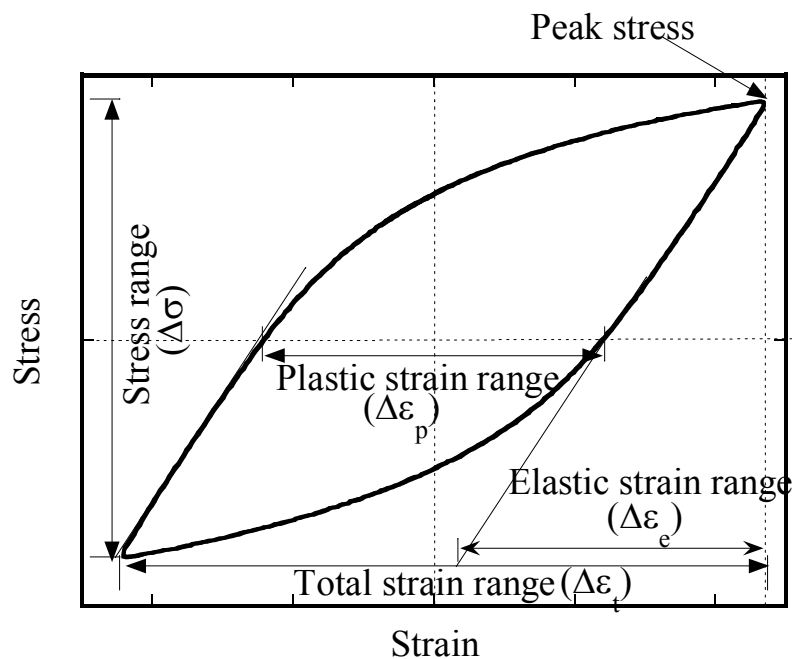


Fig. 1.5.1-1 Typical fatigue stress-strain hysteresis curve of LCF test

The plastic strain range ($\Delta\varepsilon_p$) and fatigue life (N_f) can be expressed by the Manson-Coffin's relation [72, 73]:

$$\Delta\varepsilon_p = A(N_f)^{-b} \quad (1.5.1-1)$$

where A and b are material constant.

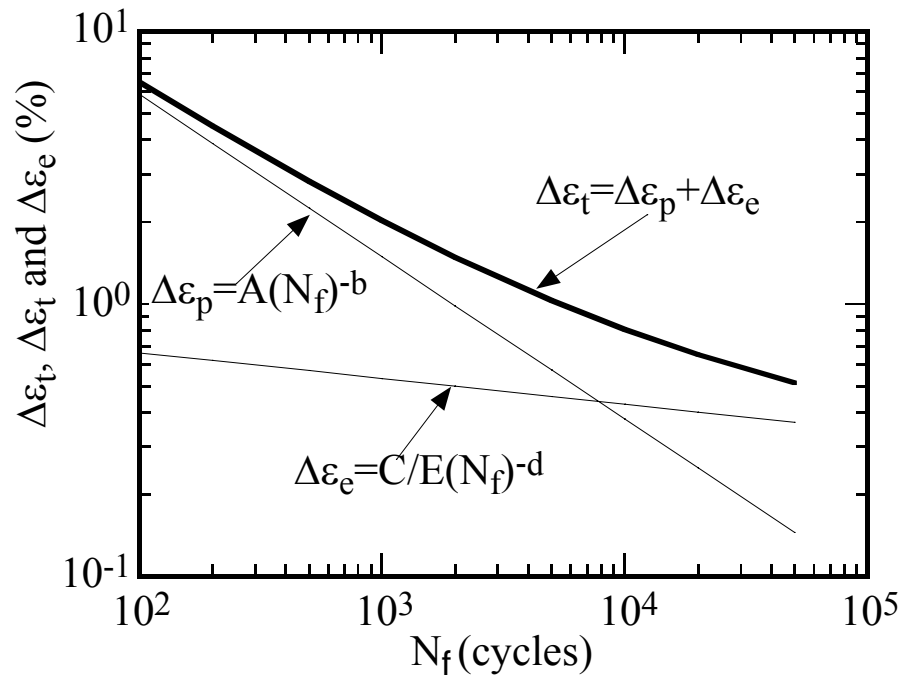


Fig. 1.5.1-2 Schematic drawing of $\Delta\varepsilon_t$, $\Delta\varepsilon_p$ and $\Delta\varepsilon_e$ versus N_f .

But many machine parts are practically working in the regime of constant total strain range. Fatigue tests are also very often advantageously performed under conditions of total strain range control. Total strain range ($\Delta\varepsilon_t$) consists of two components: plastic strain range ($\Delta\varepsilon_p$) and elastic strain range ($\Delta\varepsilon_e$).

$$\Delta\varepsilon_t = \Delta\varepsilon_p + \Delta\varepsilon_e \quad (1.5.1-2)$$

Elastic strain range ($\Delta\varepsilon_e$) is related to stress range ($\Delta\sigma$) by Hook's law.

$$\Delta\varepsilon_e = \frac{\Delta\sigma}{E} \quad (1.5.1-3)$$

The relationship between stress range ($\Delta\sigma$) and fatigue life (N_f) can be expressed as follows [72]:

$$\Delta\sigma = C(N_f)^{-d} \quad (1.5.1-4)$$

Thus, the $\Delta\varepsilon_t - N_f$ can be expressed as follow.

$$\Delta\varepsilon_t = \Delta\varepsilon_p + \Delta\varepsilon_e = A(N_f)^{-b} + C/E(N_f)^{-d} \quad (1.5.1-5)$$

Fig. 1.5.1-2 shows the total strain range ($\Delta\varepsilon_t$), plastic strain range ($\Delta\varepsilon_p$) and elastic strain range ($\Delta\varepsilon_e$) change with fatigue life (N_f).

Temperature is one of the important external parameters influencing fatigue life. The Manson-Coffin relation of steel A 286 in air and vacuum is shown in Fig. 1.5.1-3 [72]. In air, it is well known that fatigue is decrease with temperature. But in vacuum, as shown in Fig 1.5.1-3, the Manson-Coffin curves determined at room temperature (RT) and 866 K (593 °C) are — within limits of experimental scatter band — the same. Coffin [73] summarized the data of the LCF properties of several materials in vacuum or inert gas atmosphere and concluded that plastic strain range versus fatigue life curves of various steels, aluminum alloys and some refractory metals converged into a scatter band of 0.5 in factor, and that the degradation of fatigue life at high temperature did not occur when fatigue life plotted against the plastic strain range. Thus the reason for the strong temperature dependence of the Manson-Coffin curves in air is due mainly to oxidation, which changes the mechanism of crack nucleation and propagation [72]. From Fig. 1.5.1-3, the frequency effect is significant in air, but little in vacuum. That means the frequency effect is also primarily due to oxidation environment.

So the fatigue process at high temperatures is (with the exception in vacuum tests) always a corrosion fatigue process [72].

first wall in pulse D-T tokamak fusion system will undergo thermo-mechanical fatigue (TMF) as a result of the mechanical and electromagnetic loading, and the cyclic loading induced by temperature change during the plasma burn/dwell period. There are two approaches to estimate the fatigue life of structural materials under thermo-mechanical cycling. The first one is to get the relationship of cyclic loading and lifetime directly from TMF tests [76-80]. However, the acquisition of TMF data on materials by testing with simultaneously varying temperature and strain is experimentally difficult, time consuming and expensive, and the experimental procedures have not been standardized, further more the TMF data cannot be applied in design code [76]. Consequently most of relevant materials data has been generated by second approach of isothermal cyclic fatigue (ICF).

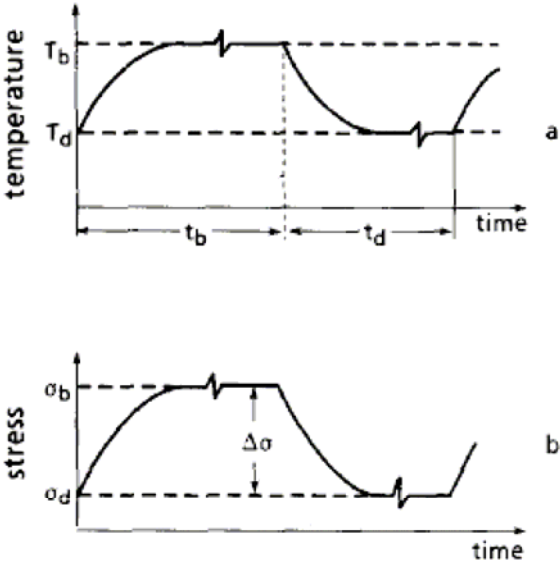


Fig 1.5.2-1 Temperature (a) and stress (b) variation during one burn/dwell cycle [75].

The change in stress during one burn/dwell cycle in Fig. 1.5.2-1 may be elastic. But time dependence swelling and creep effect lead to an addition change in stresses and strains. Furthermore, earthquake will incur the stress and strain larger than that at normal operation. In another hand, stress concentration of some parts of structure will also cause bigger stress in local position. If the combined mechanical and thermal cyclic loading is sufficient high, the cyclic plastic deformation will happen. Thus, the LCF property of structural material is necessary for design.

1.5.3 LCF behavior of RAF/M

Strain-controlled fatigue test of RAF/M steel with fully reversed triangular wave forms ($R = \frac{\varepsilon_{\min}}{\varepsilon_{\max}} = -1$, where ε_{\min} and ε_{\max} are minimum and maximum strain) have been carried out in air and vacuum at RT and elevated temperature.

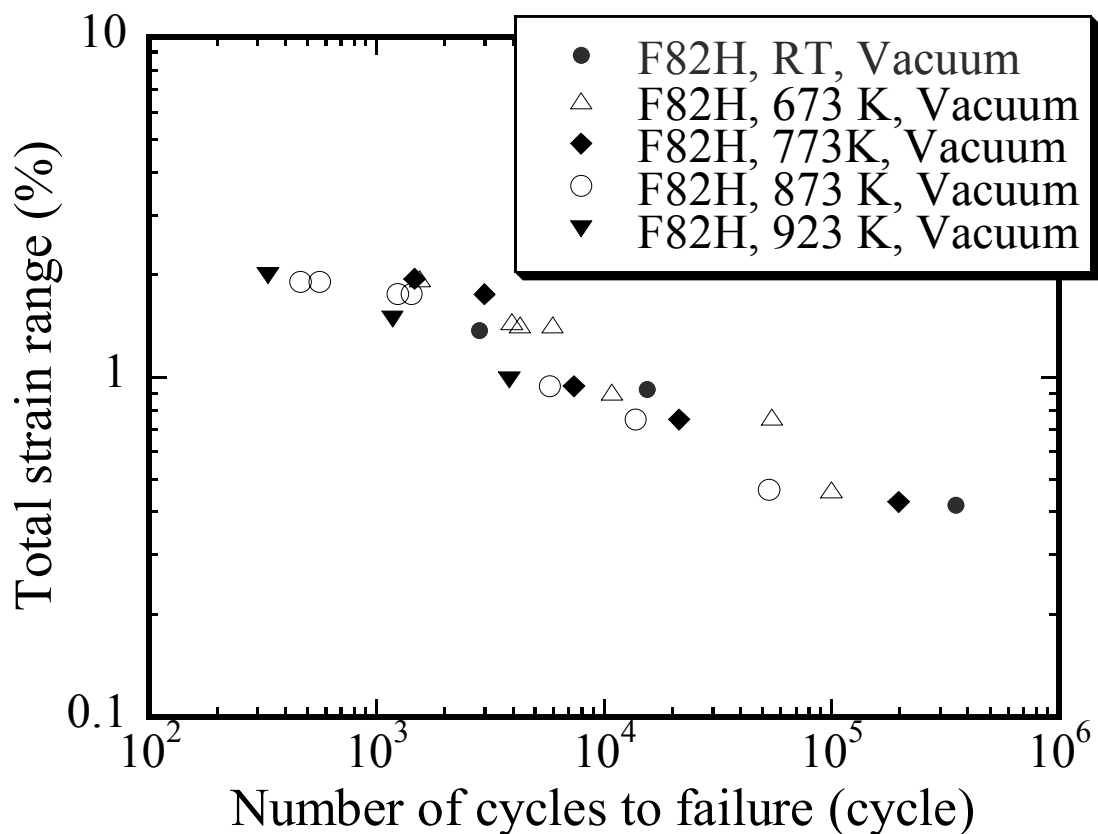


Fig. 1.5.3-1 $\Delta\varepsilon_t - N_f$ relationship of F82H at RT and elevated temperature in vacuum [81].

Figure 1.5.3-1 shows the $\Delta\varepsilon_t - N_f$ relationship of F82H [81]. No significant difference was observed when F82H tested below 773 K (500 °C), which means the $\Delta\varepsilon_t - N_f$ relationship of F82H was temperature independence at this temperature region. When temperature above 873 K (600 °C), a large reduction in fatigue life of F82H was observed. At

all test temperature, cyclic softening was observed (Fig. 1.5.3-2).

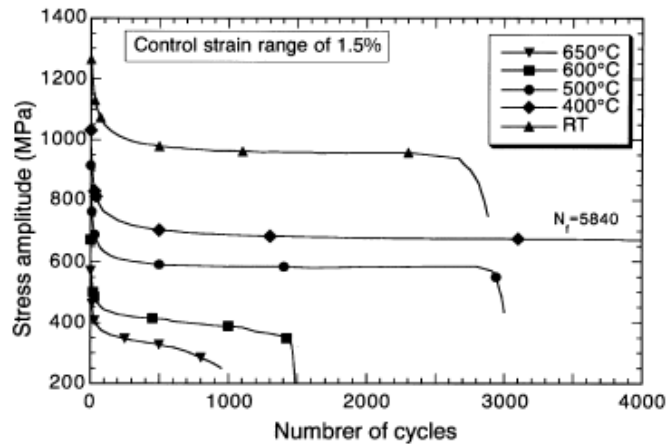


Fig. 1.5.3-2. Cyclic stress response curves for different temperatures at a control strain range of 1.5% of F82H [81].

The phenomenon that $\Delta\varepsilon_f - N_f$ relationship is temperature independence was also reported on MANET I from RT to 723 K, and Mod. 9Cr-1Mo from 755 K to 977 K [35]. The reason for this phenomenon is still unclear.

For JLF-1 steel, LCF test was carried out with round bar specimen (Fig. 1.5.3-3), mini-size and full-size hourglass specimen (Fig. 1.5.3-4) [83, 84]. The method to get the total strain range was different: the axial strain range ($\Delta\varepsilon_z$) was measured directly from the parallel part of round bar specimen; for hourglass specimen, the axial strain was converted from the diametral strain range ($\Delta\varepsilon_r$).

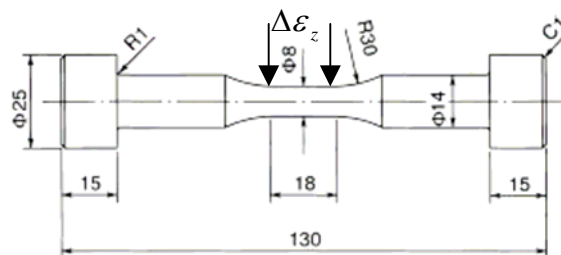


Fig. 1.5.3-3 Round bar specimen [83].

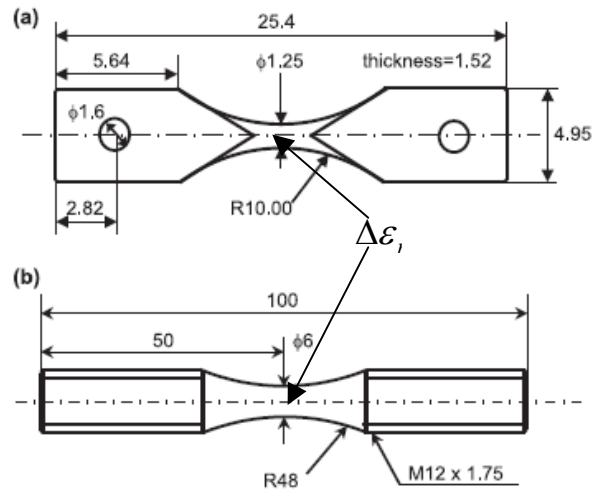


Fig. 1.5.3-4 Mini-size (a) and full-size (b) hourglass specimen [84].

The advantages and disadvantages of hourglass and round bar specimens are summarized in Table 1.5.3.1.

Table 1.5.3-1 Advantages and disadvantages of hourglass and round bar specimen.

	Hourglass specimen	Round bar specimen
Crack initiation	Center part	Random distributed along the parallel part
Deformation measurement	Diametral	Axial
Buckling	Resistance	Little resistance
Strain evaluation	Need conversion	Real

The shape and size effects on fatigue life are shown in Fig. 1.5.3-5. The $\Delta\varepsilon_t - N_f$ relationship of hourglass specimen is steeper than that of round bar specimen. For hourglass specimen, the size effect should be considered.

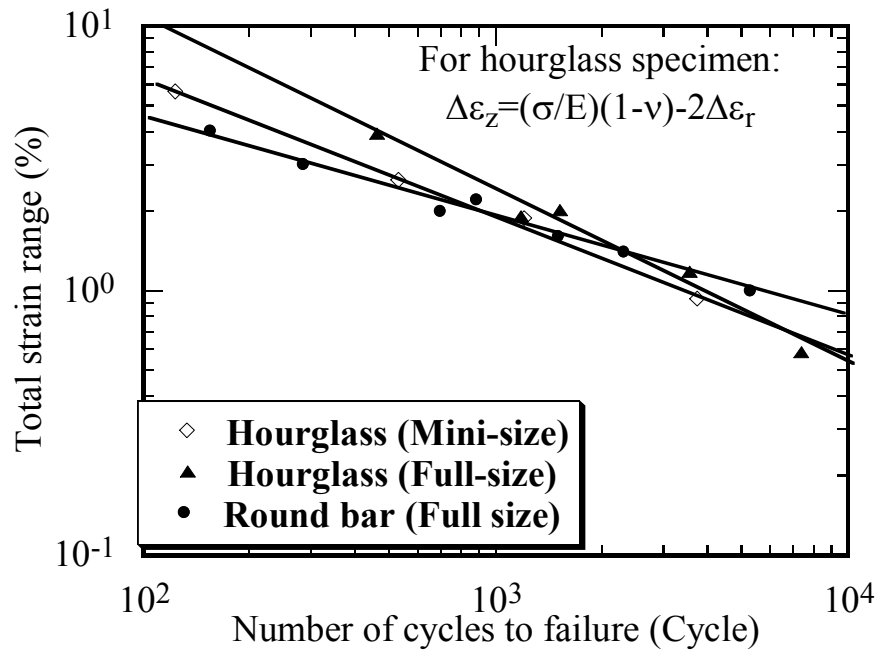


Fig. 1.5.3-5 Shape and size effects on fatigue life of JLF-1 steel at RT in air [83, 84].

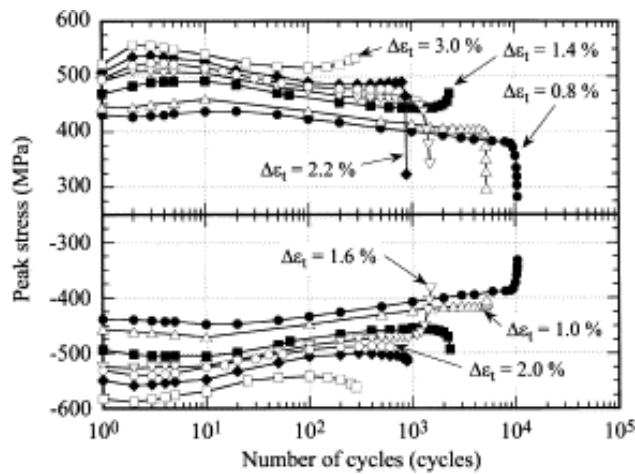


Fig 1.5.3-6. Change in peak stresses during fatigue tests of JLF-1 [83].

Same as F82H, cyclic softening of JLF-1 steel was observed at RT (Fig. 1.5.3-6). A little difference is that strain hardening was observed in initial cycles. That means dislocation was tangled at initial cycles, then dislocation annihilation occurred, so cyclic softening was observed.

The published paper on LCF of RAF/M steel is summarized in Table 1.5.3-2. The LCF

properties and microstructure evolution of JLF-1 steel at elevated temperature are necessary to be investigated.

Table 1.5.3-2 Published paper on LCF of RAF/M.

Temperature	Specimen type		JLF-1	F82H	Eurofer 97
RT	Round bar	Engineering sized	[83]	[81]	—
		Mini-sized	—	[82]	—
	Hourglass	Engineering sized	[84, 88]	—	—
		Mini-sized	[84]	[87]	—
Elevated	Round bar	Engineering sized	Necessary	[78, 81,86]	[78]
		Mini-sized	—	[68]	[68]
	Hourglass	Engineering sized	[85]	—	—
		Mini-sized	—	—	—

1.6 Objectives of present research

Among the fission, fusion, and other source such as wind power, fusion has been actively considered as the 21st century energy source in the world major countries. The structural integrity of fusion reactor depends on the properties of the structural materials. Thus, development of reactor materials and power generating blankets is a critical issue for early realization of fusion energy. Of the three materials for fusion applications (RAF/M, V-alloy, and SiC/SiC), the RAF/M steel is considered as the leading candidate structural material for first wall in fusion reactor as there exists a well-developed technology and a broad industrial experience with the ferritic/martensitic steels in fossil and nuclear energy technology. From the results of irradiation, JLF-1 is the strong candidate low activation ferritic/ martensitic steel as future fusion structural material.

LCF behaviors of JLF-1 steel at elevated temperature are necessary for plastic design since the cyclic plastic deformation will happen if the combined mechanical and thermal cyclic loading of first wall is sufficient high. To avoid the shape, size, and environment effects, the LCF test should be carried out with engineering size (6-8 mm in diameter) round bar specimen in vacuum.

Thus the objective of this research is to study the tensile and LCF behavior of a candidate material of first wall, JLF-1 steel, at elevated temperature with an engineering size specimen in vacuum. It includes the following contents:

- 1) Temperature effect on the relationship between fatigue life and plastic strain range.
- 2) Cyclic softening/hardening and its mechanism.
- 3) Cyclic yield stress-strain curves and its application on design.

To obtain basic information of RAF/M at elevated temperature, the tensile test was also carried out.

Chapter 2 Experimental Procedure

Action of development RAF/M steels for fusion reactor application has been carried out under IEA international collaboration. The 9Cr-2W ferritic steel, named JLF-1, was fabricated in Japan [52, 57]. The material in this research is the second heat JLF-1 steel plate, 25 mm and 15 mm in thickness.

2.1 Chemical composition of JLF-1 steel and heat treatment.

JLF-1 was designed to have good irradiation resistance, high temperature mechanical performance and high toughness as well. The chemical composition of the JLF-1 steel plate in wt% is shown in Table 2.1-1. The plate was 15 mm thick and had a heat treatment as follows: 1323 K/3.6 ks/air cooling (normalizing) and 1052 K/3.6 ks/air cooling (tempering) [83]. The microstructure is tempered martensite, to be shown in Fig. 3.2.2-1 (a).

Table 2.1-1 Chemical composition of JLF-1 (wt%) [83].

C	Si	Mn	P	S	Al	Cr	W	V	Ta	N	B	Ni	Cu	Mo	Nb
0.10	0.05	0.45	0.003	0.002	0.003	8.85	1.99	0.20	0.080	0.0231	0.0002	<0.01	<0.05	<0.001	<0.002

The addition of W (< 3%) improves creep strength in high Cr steel, but excess addition, more than 2~3%, cause toughness degradation due to δ -ferrite formation. V addition also improves the creep strength at elevated temperature, but excess V addition causes significant coarsening of carbides at high temperature, resulting in severe degradation of mechanical properties. Nb has similar role as V, but it is harmful element from the standpoint of low activation alloy design. Thus, Ta is chosen to be added for high temperature strength improvement as Ta has equivalent role as Nb. Ti additions is thought to suppress irradiation induced void formation. Small amount of N is considered to improve high temperature creep strength [70].

2.2 Tensile and fatigue specimens

According to ASTM standard [89-91], the shape and dimension of tensile and fatigue specimen was designed as Fig.2.2-1. To save material, 15mm×15mm×70mm sticks were cut from the JLF-1 steel plate, followed by welding two SM500 steel blocks with electron beam (EB) at the both ends of the stick, then, it was machined to the tensile and fatigue test specimens.

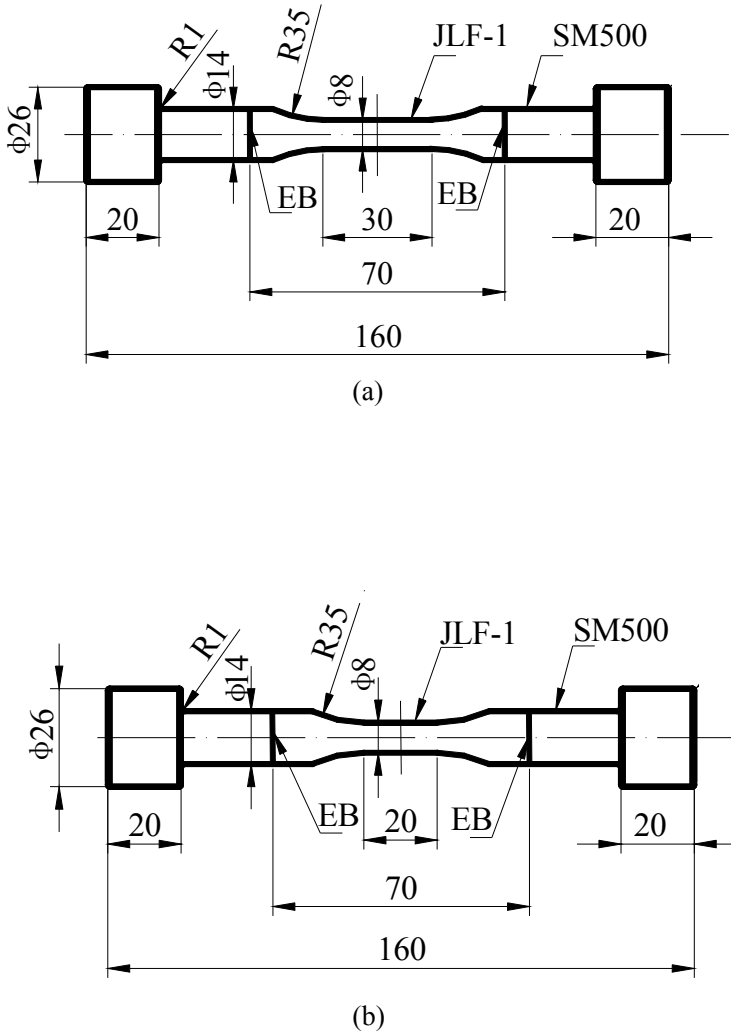


Fig. 2.2-1 Tensile (a) and fatigue (b) test specimen.

2.3 Test system

To avoid the oxidation effect, the tensile and fatigue specimens of JLF-1 steel should be tested in vacuum at elevated temperature. Testing system includes three parts: mechanical machine, vacuum system, and heating system. The schematic drawing of the testing system is shown in Fig. 2.3-1.

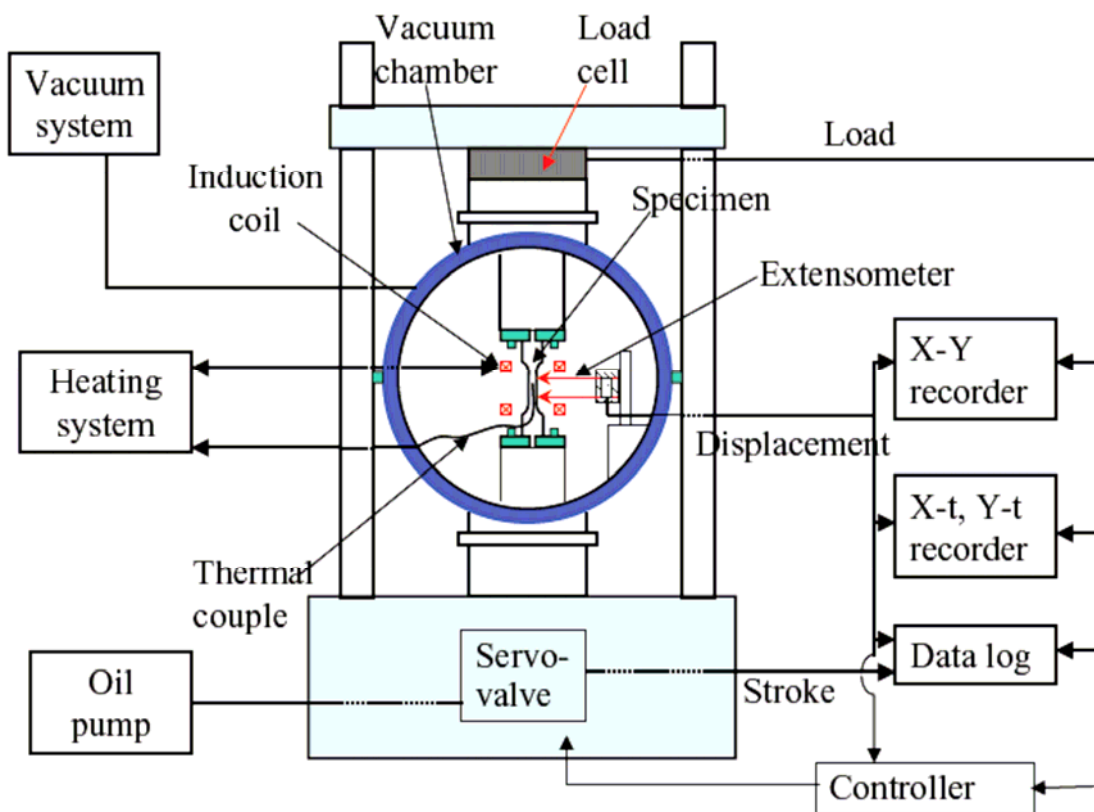


Fig. 2.3-1 Scheme of test system.

The specimens were tested in vacuum chamber. The temperature was measured by thermal couple, and the signal of thermal couple was feedbacked to heating system to control the temperature stable during test. The load and axial displacement were measured by the load cell and extensometer directly, and the signals were recorded by X-Y recorder, X-t and Y-t recorder, and Data logger.

- **Vacuum system**

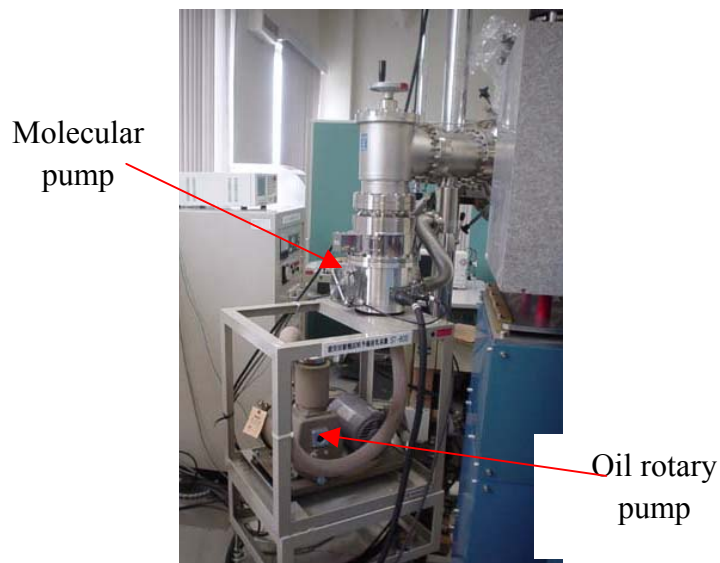


Fig 2.3-2 Vacuum system.

The vacuum system consisted of oil rotary pump, molecular pump (Fig 2.3-2), and vacuum chamber (Fig 2.3-3). The capacity of the vacuum system is $\sim 10^{-3}$ Pa.

- **Mechanical test machine**

The mechanical test machine is the Shimazu Servopulser with a dynamic load capacity of ± 10 tons. Specimens were tested in the vacuum chamber (Fig 2.3-3), and heated by an induction coil. Axial strain was measured by a Shinko 1501-93-20 extensometer, which has a differential transducer with gage length (G.L.) of 12.5 mm and the capacity of ± 1 mm. To reduce the noise generated from the induction coil and keep the temperature of extensometer stable during tensile and fatigue tests at elevated temperature, a water cooling jacket was installed.

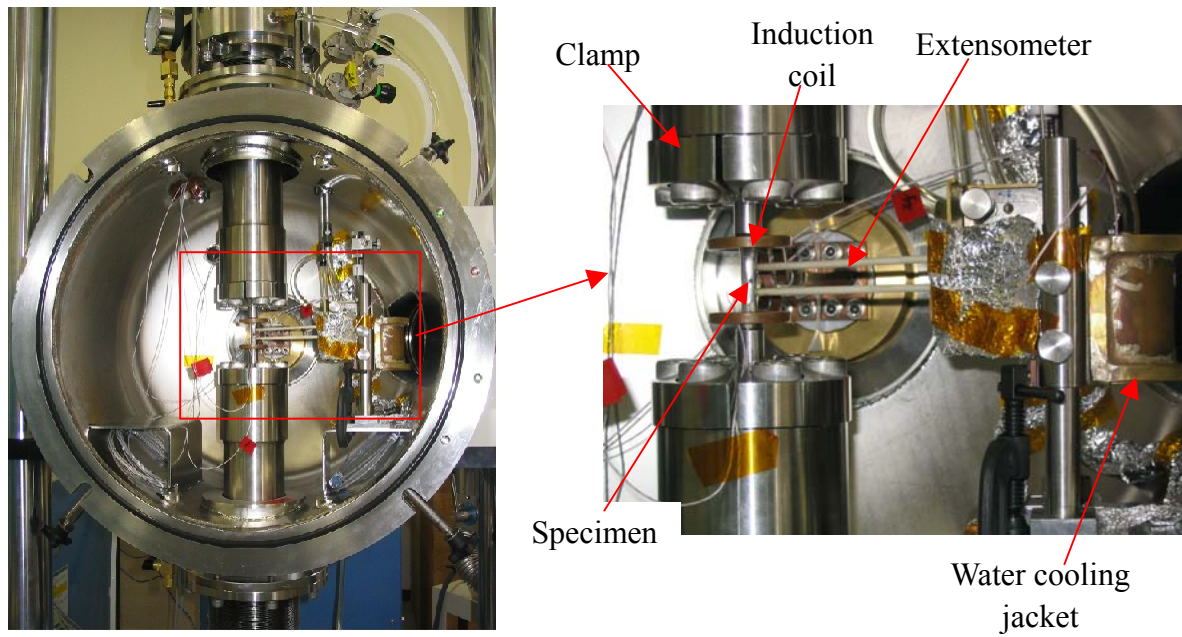


Fig 2.3-3 Inner equipment of vacuum chamber.

- **Induction heating system**

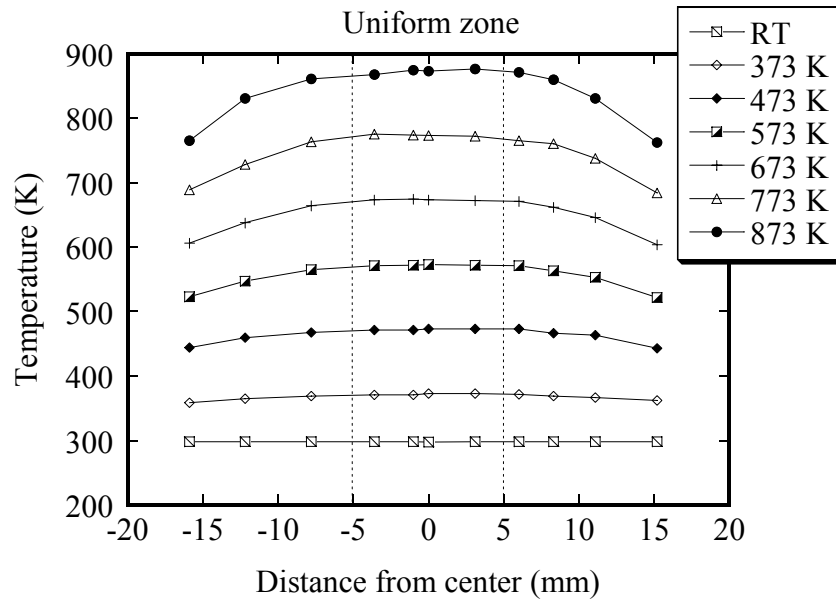


Fig 2.3-4 Power supply for induction heating device.

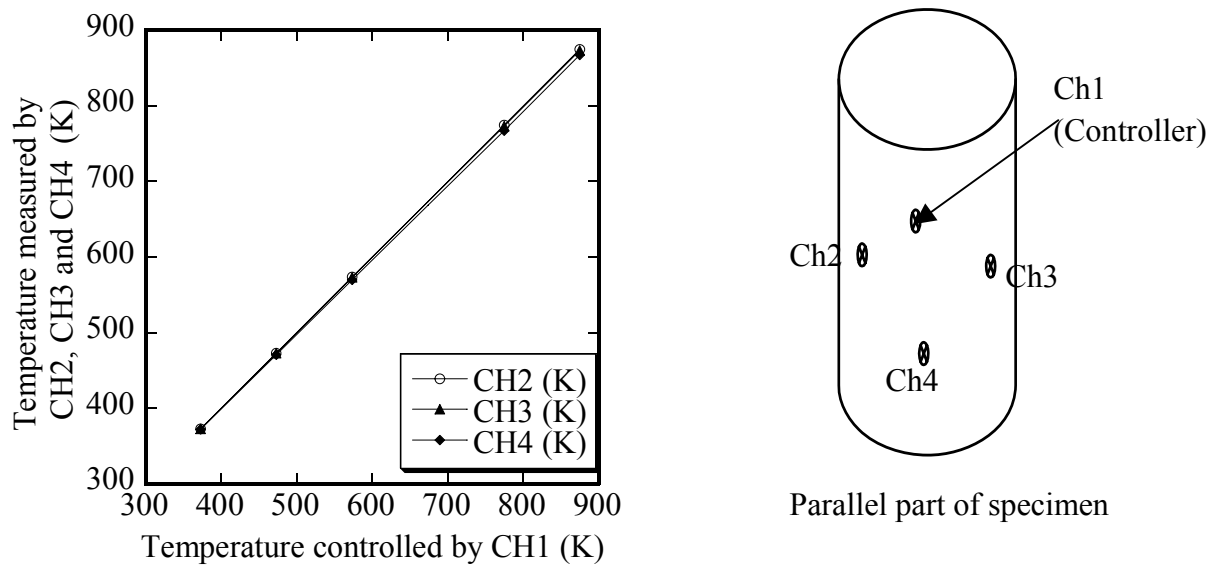
The power supply for induction heating device is shown in Fig 2.3-4. The parameter of heating system are 100 kW of input power, 100 kHz of induction frequency, and a capacity of form RT to 973 K with sensitivity of 0.1 K.

2.4 Temperature profile of specimen

The temperature control is the key to carry out the tensile and fatigue test at elevated temperature. Before the research, the temperature profile was obtained.



(a) Axial distribution along the parallel part of specimen.



(b) Circular distribution in temperature uniform zone.

Fig. 2.4. Temperature profile of specimen.

The temperature profile of specimen was measured from room temperature (RT) to 873 K by thermocouples (ϕ 0.32 mm) welded in axial and circular direction. Fig. 2.4 (a) shows the temperature distribution along axial direction. There is a temperature uniform zone (about 10mm in length) in the parallel part of specimen. The temperature distribution along the circular direction in the uniform zone is shown in Fig. 2.4. (b), channel 1 (Ch1) was the controller of which the signal was feedbacked. There was little difference among the data of Ch1, Ch2, Ch3, and Ch4.

Based on the temperature profile on the specimen, two thermocouples were welded in the gage length on the specimen for temperature control during tensile and fatigue tests. One thermocouple was used for the control of the temperature and the other was to monitor the temperature. The temperature difference in the two thermocouples was kept less than 3 K, which was satisfied with the requirement of ASTM standard (the greater of 2 K and 1% of test temperature).

2.5 Test procedure

- Tensile test

The detail procedure of tensile test is shown in Fig 2.5-1. Tensile specimens were polished in the longitudinal direction with #1500 emery paper to erase the circumferential machining marks. Tensile tests were carried out in vacuum ($\leq 5 \times 10^{-3}$ Pa) from RT to 873K at strain rates of 0.1%/s and 0.02%/s. The axial displacement of the specimens was measured by a Shinko 1501-93-20 extensometer from 0 to 1 mm, and then changed to stroke control until broken. The test data were stored in the Yokogawa DL 708 (sampling rate is 20 /s). At the same time, the load and displacement curves were drawn by Yokogawa 3023 X-Y recorder. Those data will be applied to design base of JLF-1.

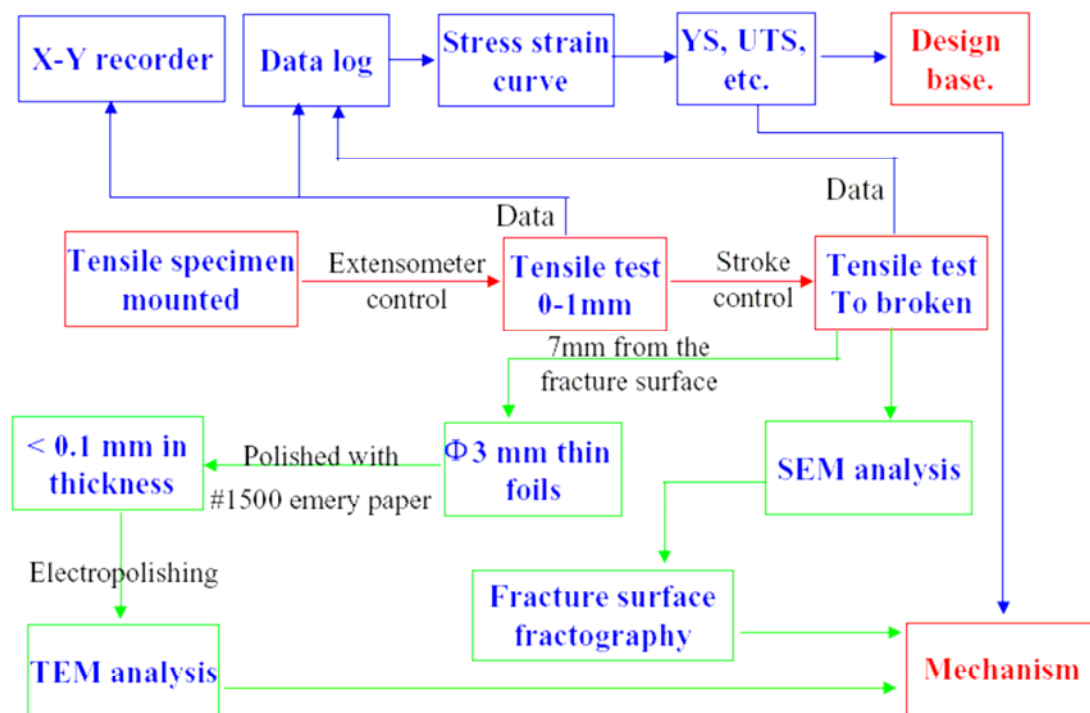


Fig. 2.5-1 Procedure of tensile test.

The fracture surface was observed with scanning electron microscopy (SEM). The ϕ 3mm thin foils for transmission electron microscopy (TEM) observation were prepared from

JLF-1 plate, and at 7 mm from the fracture surface of the tensile specimen to avoid the effect of necking. All thin foils were polished to less than 0.1 mm in thickness with #1500 emery paper, followed by electropolishing to perforation for TEM examination. So, the microstructure change during static loading would be applied to explain the mechanism of macro-phenomenon.

- Low cycle fatigue test

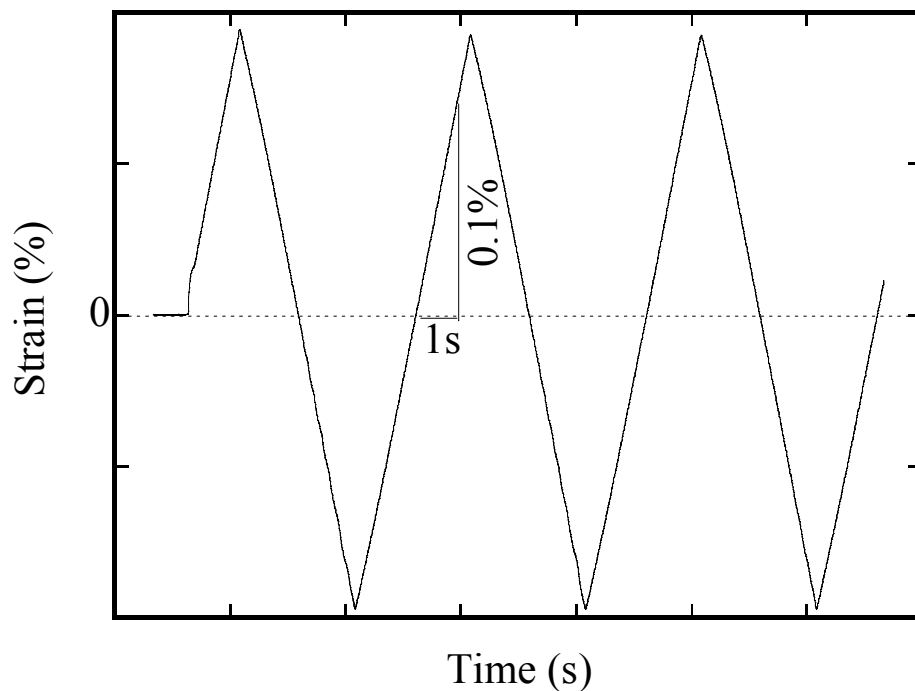


Fig. 2.5.2 Fully reversed push-pull triangular wave with an axial strain-control (0.1%/s).

Fatigue specimens were polished in the longitudinal direction with #1500 emery paper to erase the circumferential machining marks. LCF tests with total strain range of $\Delta\varepsilon_t=0.6\%\sim 2.4\%$ were carried out in vacuum ($\leq 5 \times 10^{-3}$ Pa) at RT, 673 K, and 873 K. A fully reversed push-pull triangular wave was applied with strain rate of 0.1 %/s (Fig. 2.5.2). The detail procedure is shown in Fig 2.5-3.

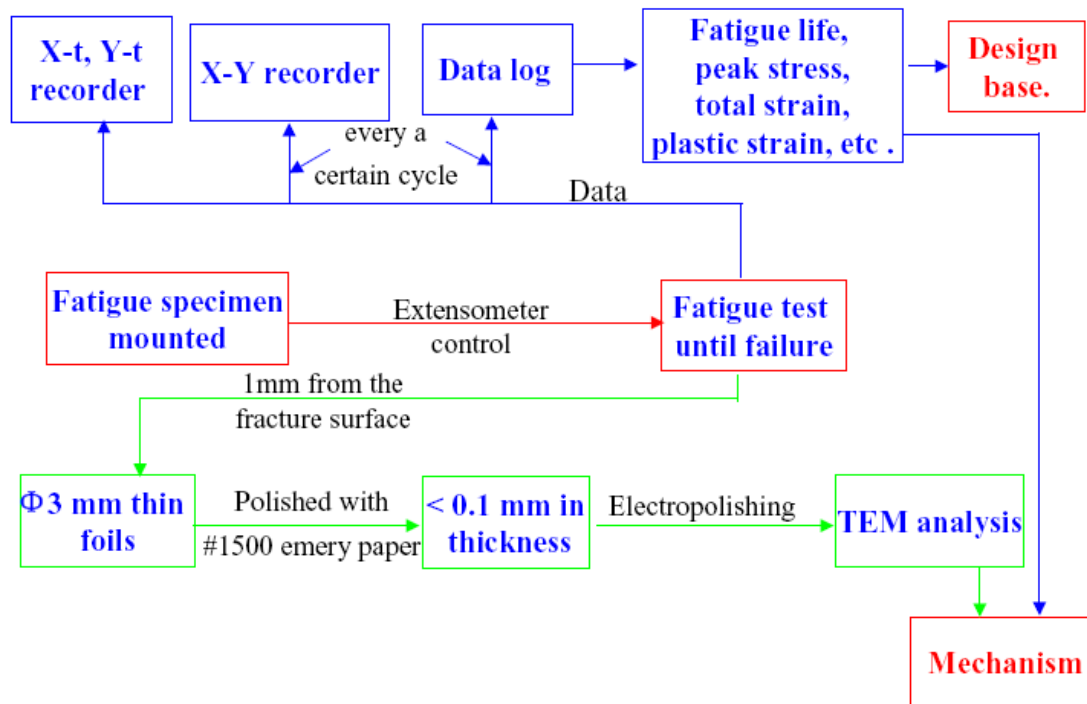


Fig. 2.5-3 Procedure of LCF test.

The temperature difference of the two thermocouples was kept less than 3 K. The number of cycles to failure is defined as either the cycle when the peak tensile stress decreased by over 25% from an extrapolation curve of the peak tensile stress against number of cycles (Fig. 2.5-4), or test signal becomes unstable. All the test data were recorded by Yokogawa LR 4210 recorder. The load and displacement data were stored at every a certain cycle in the Yokogawa DL 708 (sampling rate is 20/s). At the same time, the load and displacement hysteresis curve was drawn by Yokogawa 3023 X-Y recorder. Those data will be applied to design base of JLF-1.

To investigate the microstructure change during fatigue at elevated temperature, tests were terminated for some specimens at 10th and 500th cycle with total strain range of $\Delta\varepsilon_f=1.8\%$ at RT, 673 K and 873 K, and the thermal history simulating of LCF test of $\Delta\varepsilon_f=1.8\%$ at 673 K and 873 K was carried out in annealing furnace in vacuum.

The $\phi 3\text{mm}$ thin foils for transmission electron microscopy were prepared from JLF-1 plate, thermal history simulating specimen, and center part of the fatigue specimen. All the

thin foils were polished to less than 0.1 mm in thickness with #1500 emery paper, followed by electropolishing to perforation for TEM examination. The microstructure change during cyclic loading could be compared with that during static loading, and heat treatment. The mechanism of fatigue behavior would be discussed base on the microstructure analysis.

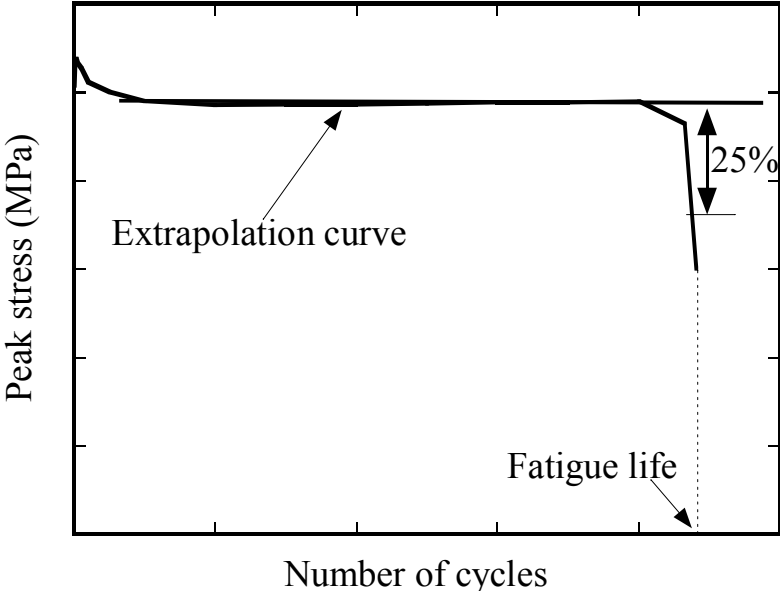


Fig. 2.5-4 Definition of fatigue life.

Chapter 3 Tensile Test and Microstructural Analysis

Tensile property of material at elevated temperature is one of the key issues for design [75, 92]. The tensile test results and microstructure analysis of JLF-1 steel at strain rate of 0.1%/s and 0.02%/s were studied from RT to 873 K to investigate the material static deformation behavior which is one of the important information to design a blanket component as a basic property data. To study the mechanism, the microstructural analysis was carried out with SEM and TEM. The tensile test and microstructure analysis items are listed in Table 3-1.

Table 3-1 Tensile test and microstructure analysis items.

	RT	373 K	473 K	573 K	673 K	773 K	873 K
0.1%/s	●▲■	—	●▲	●▲	●▲■	●▲	●▲■
0.02%/s	—	●▲	●▲	●▲	●▲	●▲	●▲

- Tensile test was carried out;
- ▲ Fracture surface fractography was observed with SEM;
- Microstructure was analyzed with TEM.

3.1 Tensile test results

3.1.1 Tensile behavior

The tensile stress-strain curves of JLF-1 steel at strain rate of 0.1%/s and 0.02%/s are shown in Fig. 3.1.1-1 and 3.1.1-2, respectively. The strain rate did not affect the stress-strain behavior of JLF-1 significantly. JLF-1 steel was elastic deformation first; then became plastic deformation at each temperature.

The strain hardening coefficient (θ), which means an increasing stress is required to produce additional plastic deformation when a metal is strained beyond the yielding point, could be expressed as,

$$\theta = \frac{\Delta\sigma}{\Delta\varepsilon} \quad (3.1.1-1)$$

where $\Delta\varepsilon$ is additional strain during plastic deformation, $\Delta\sigma$ is the increasing stress when

deformation is changed for $\Delta\varepsilon$ (Fig. 3.1.1-1). Little strain hardening was observed at 873 K at strain rate of both 0.1%/s and 0.02%/s.

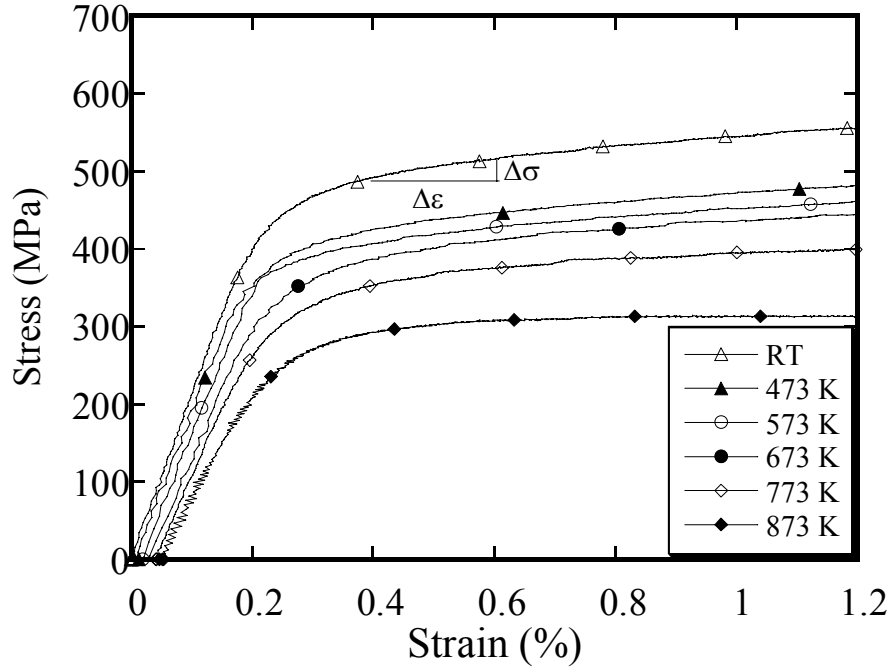


Fig. 3.1.1-1 Stress-strain curves of JLF-1 steel at strain rate of 0.1%/s.

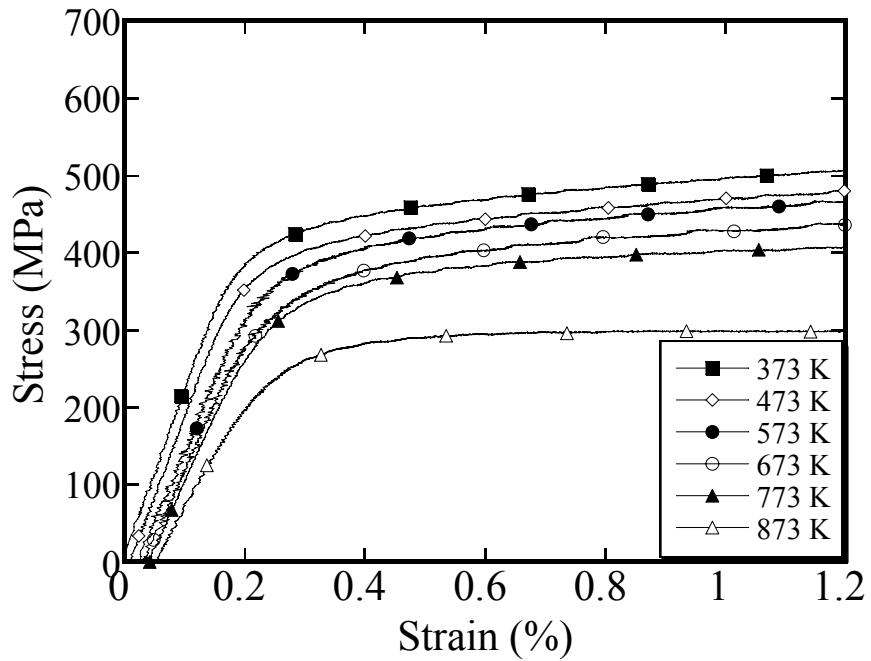


Fig. 3.1.1-2 Stress-strain curves of JLF-1 steel at strain rate of 0.02%/s.

The yield stress (YS) and ultimate tensile strength (UTS) are the important data for design, and the reduction in area (RA) corresponds to the ductility of material. The changes in YS, UTS, and RA of JLF-1 steel against test temperature are shown in Fig. 3.1.1-3 and 3.11-4. The strain rate did not affect the YS, UTS and RA significantly. The difference between YS and UTS decreased significantly above 773 K, which means strain hardening became smaller in this temperature region. Especially at 873 K, the UTS of JLF-1 dropped to about 300 MPa, very close to the YS. Corresponding to the decrease in strain hardening, the RA increased rapidly above 773 K.

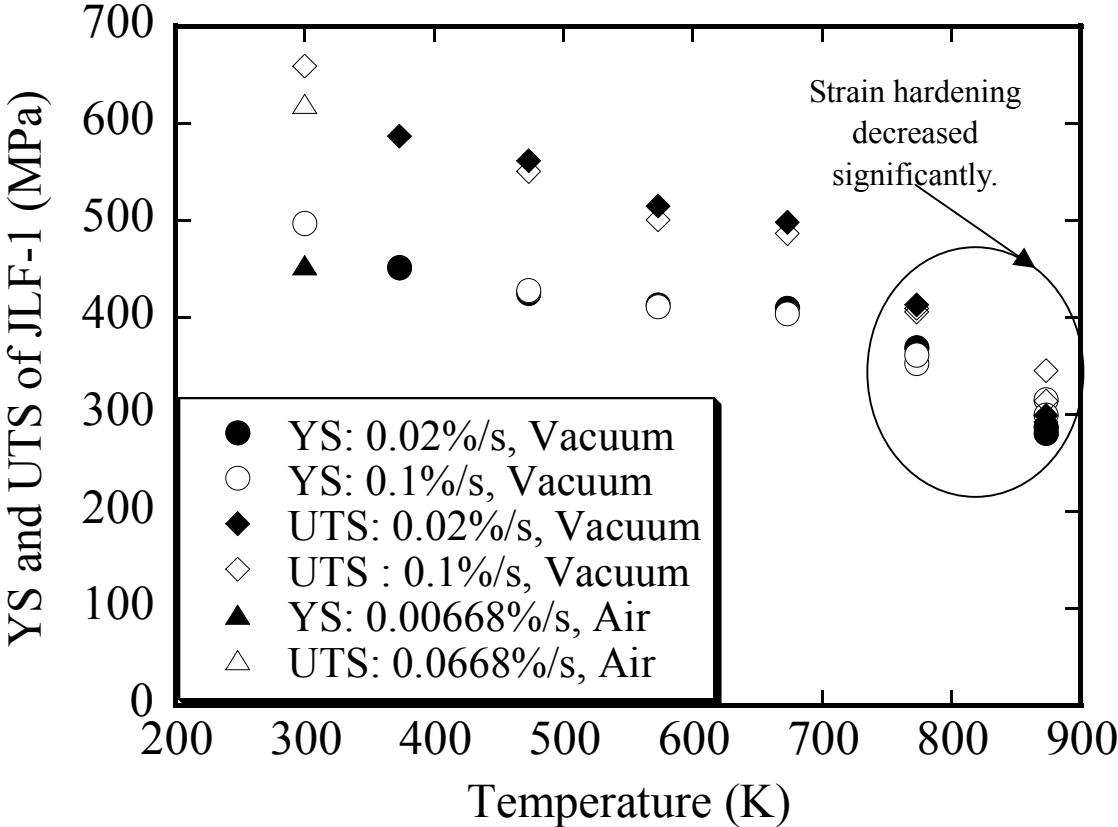


Fig.3.1.1-3 Change in YS and UTS against test temperature.

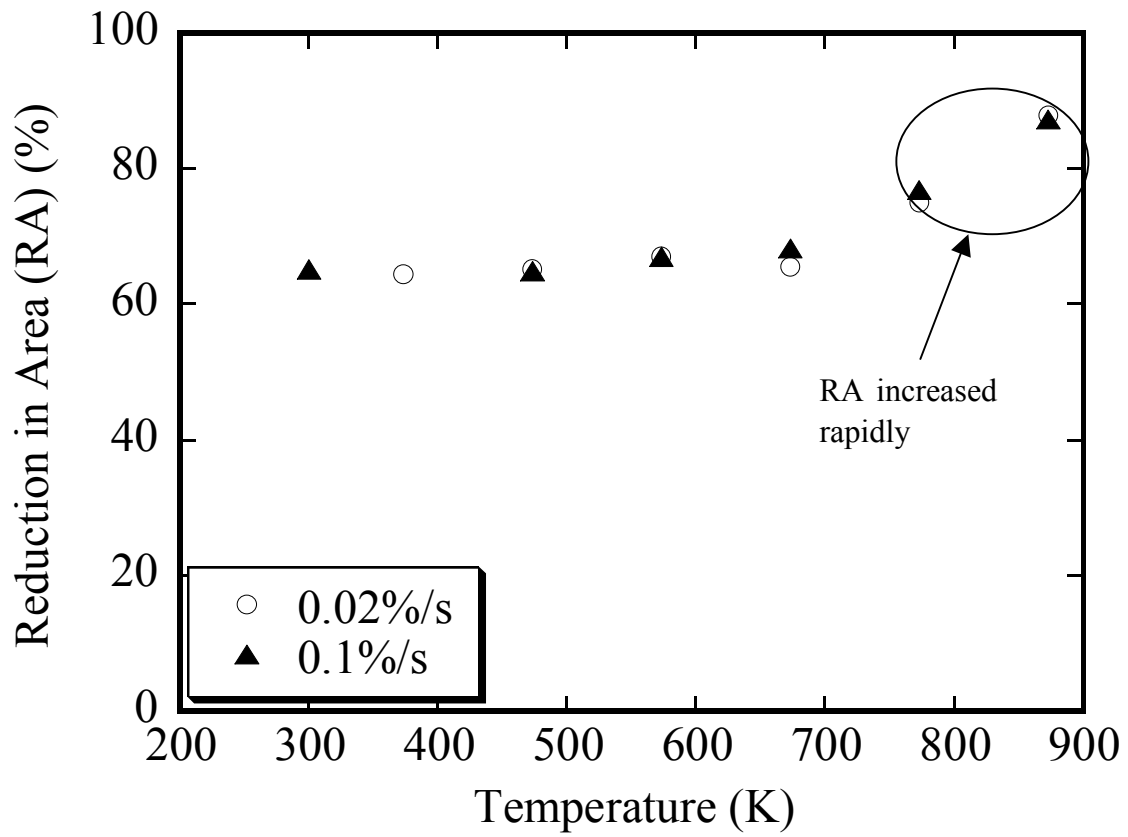
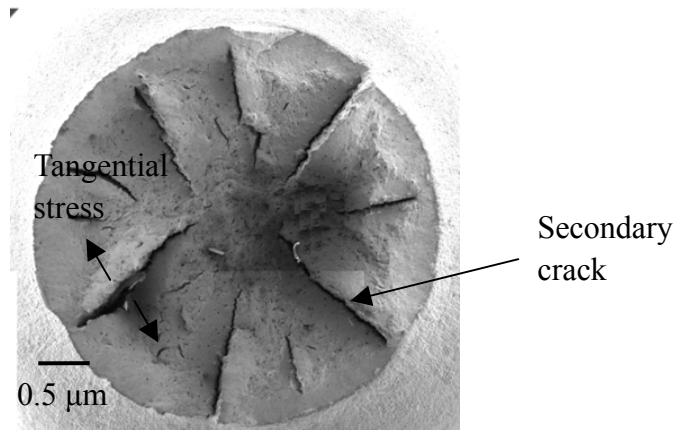


Fig.3.1.1-4 RA change against temperature.

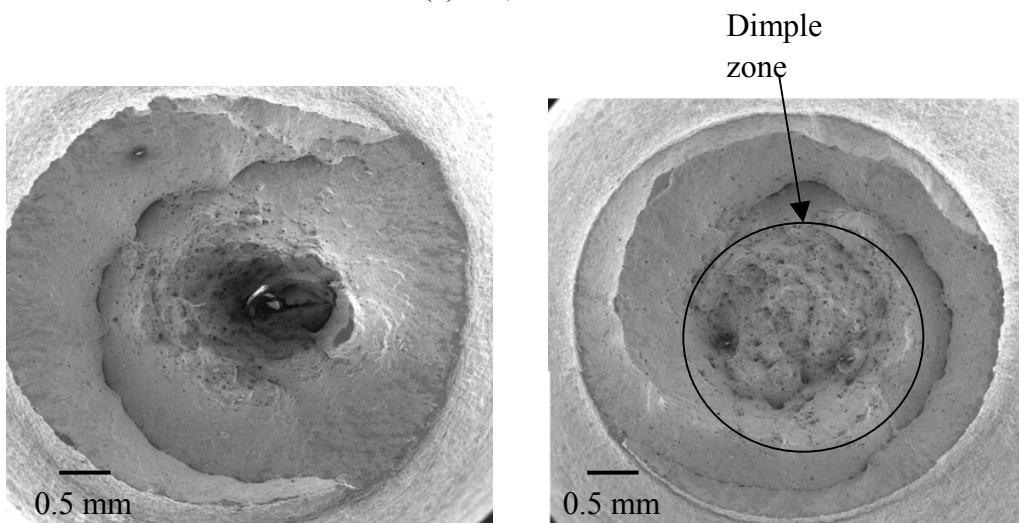
3.2 Effect of static deformation on microstructural change.

3.2.1 Fracture surface fractography

The fracture surface fractography of the tensile specimens after static deformation were observed with SEM. Fig. 3.2.1-1 shows the SEM images of fracture surfaces of the tensile specimens at strain rate of 0.1%/s at RT, 0.1% and 0.02%/s at 673 K and 873 K. Secondary cracks in the radial direction were observed on the broken surface at RT, which were formed by tangential stress during necking where the tri-axial stress happened [93]. Cup and cone fracture was observed in the specimens tested at high temperature. High density of dimples was observed at 873 K, implying enhanced ductility at high temperature.

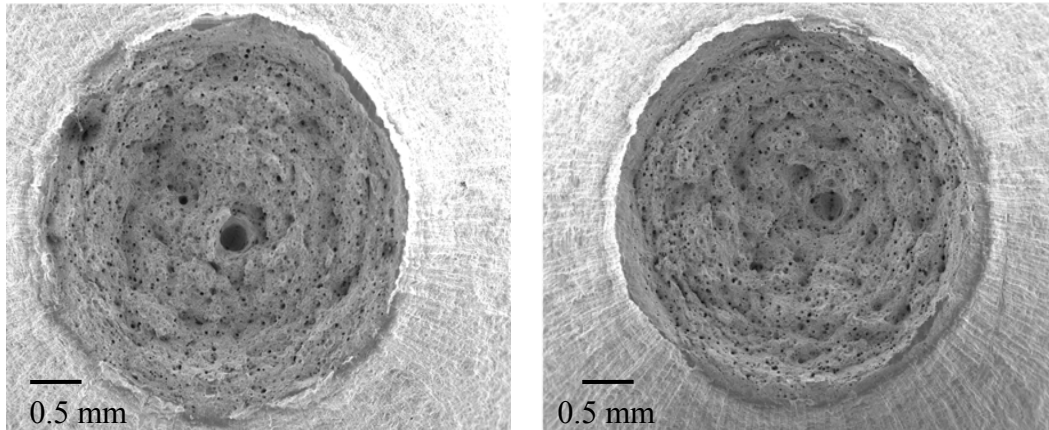


(a) RT, 0.1%/s.



(b) 673 K, 0.02%/s.

(c) 673 K, 0.1%/s.



(d) 873 K, 0.02%/s.

(e) 873 K, 0.1%/s.

Fig 3.2.1-1 SEM images of the fracture surfaces of the tensile specimens at RT, 673 K and 873 K.

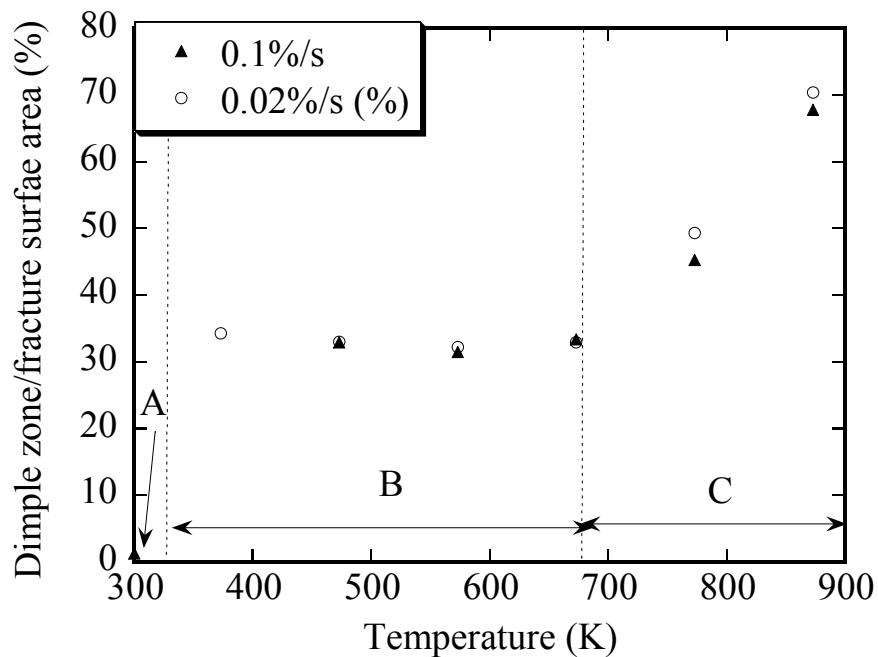


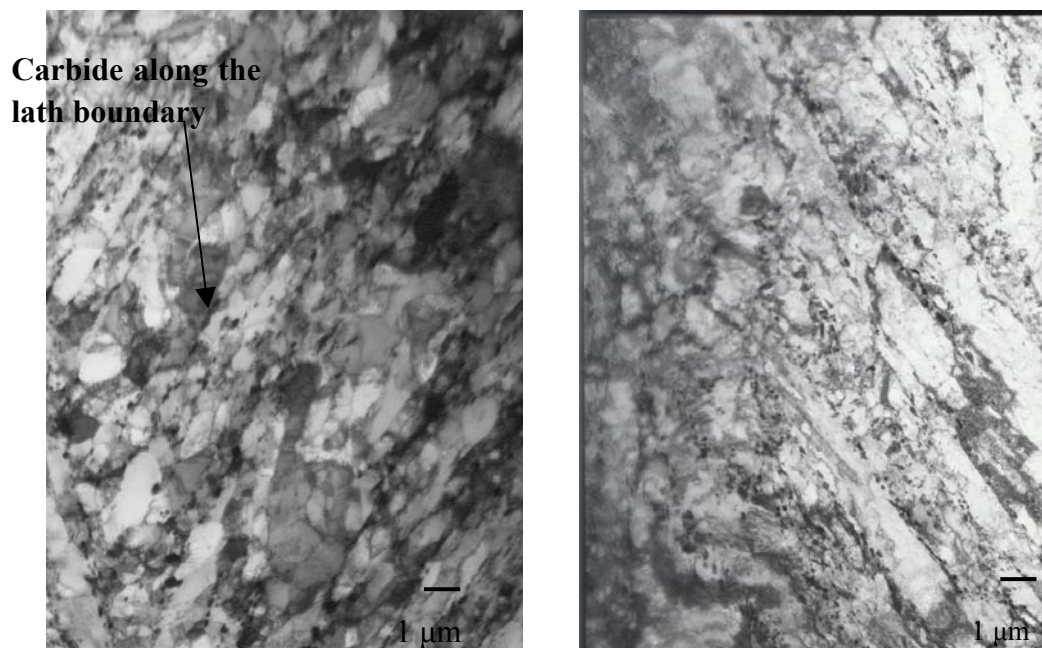
Fig 3.2.1-2 Change in the ratio of dimple zone to fracture surface area against temperature.

Fig 3.2.1-2 shows change in ratio of dimple zone to fracture surface area of tensile specimen; the dimple zone was measured as in Fig 3.2.1-1 (c). Three regions could be defined

according to the ratio change.

- Region A: Around RT, the dimple zone was small, so the secondary crack was observed Fig 3.2.1-1 (a).
- Region B: Below 673 K, the change in ratio was independent on temperature, shear fracture was dominant (Fig 3.2.1-1 (b) and (c)). Thus, the RA has no significant change in this region (Fig.3.1.1-4).
- Region C: Above 673 K, the change in ratio was very sensitive to temperature, dimple fracture was dominant (Fig 3.2.1-1 (d) and (e)). Thus, the RA increased rapidly in this region.

3.2.2 TEM image



(a) RT, before tensile test.

(b) RT, after tensile test.



(c) 673 K, after tensile test.



(d) 873 K after tensile test.

Fig 3.2.2-1 Effect of static deformation on microstructure of JLF-1 steel at RT, 673 K and 873 K.

The TEM images of JLF-1 steel before and after tensile tests are shown in Fig. 3.2.2-1. Before tensile test, JLF-1 steel consisted of a martensitic structure, with carbides distributed along the lath boundary (Fig 3.2.2-1 (a)). After tensile test at RT, the lath width became a little wider (Fig 3.2.2-1 (b)). With temperature increase, the lath width increased (Fig 3.2.2-1 (c) and (d)).

3.3 Discussion

3.3.1 Strain hardening

The comparison in YS and UTS between JLF-1 and F82H is shown in Fig 3.3.1-1. YS and UTS of JLF-1 were lower than that of F82H in low temperature. But at high temperature, the strengths difference between JLF-1 and F82H becomes narrow. That means the tensile property of JLF-1 steel is comparable to that of F82H at elevated temperature.

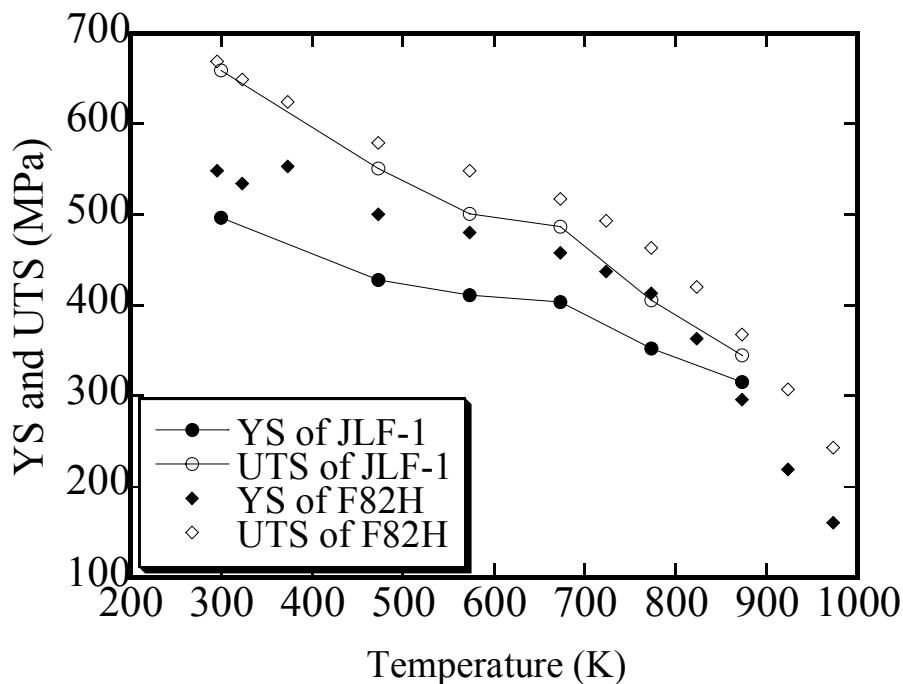


Fig. 3.3.1-1 YS and UTS of JLF-1 and F82H.

(Data of F82H was taken from [64])

Same as F82H and Eurofer 97 [58, 64, 67], strain hardening of JLF-1 steel decreased significantly above 673 K, this tendency was proved by the true stress-strain data of F82H [94]. The strain hardening of JLF-1 could be considered as the results of the interaction among dislocations during static deformation. Below 673 K, the interaction among dislocations was so strong that the strain hardening was pronounced. At 773 K and 873 K, the climbing of edge dislocation and cross gliding of screw dislocation happened, so the strain hardening was decreased, and little strain hardening was observed at 873 K.

Since the strain hardening decreased, the difference between YS and UTS decreased, further more, there was little strain hardening at 873 K (Fig.3.1.1-3); the RA also increased rapidly above 673 K (Fig. 3.1.1-4); and the surface fractography was changed from shear fracture below 673 K to dimple fracture at 773 K and 873 K (Fig. 3.2.1-1).

Thus, it can be conclude that with temperature increase, JLF-1 steel becomes near to be a perfect elastic-plastic body (without strain hardening) and ductility improved.

3.3.2 Relation between YS and lath width of JLF-1 at elevated temperature

As the macro-phenomenon is dominated by the microstructure, it is necessary to obtain the relationship between tensile property and microstructural change.

In tensile test at RT, the yield stress (σ_y) of martensitic can be separated into several components [95, 96],

$$\sigma_y = \sigma_0 + \sigma_b + \sigma_i, \quad (3.3.2-1)$$

where σ_0 is Peierls stress of bcc iron, which is the stress required to move dislocation through a perfect lattice; σ_b is the grain boundary strengthening; σ_i is the effect contribution of other mechanism, such as precipitate dispersion strengthening, solid solution effect, and the dislocation strengthening.

According to reference [95, 96], the martensite lath width is the dominant factor to contribute the grain boundary strengthening in tempered martensite structure. The relationship between grain boundary effect (σ_b) and lath width (d) is:

$$\sigma_b \propto d^{-1/2}. \quad (3.3.2-2)$$

However, there is no report about the YS and lath width relationship at high temperature tensile test. The YS and lath width of JLF-1 steel after tensile test are shown in Fig. 3.3.2-1. The lath width was estimated from TEM micrographs as an average separation of the boundaries [97]. The tendency shows the YS decreased and lath width increased with temperature. The YS and lath width could imply qualitative relationships with temperature.

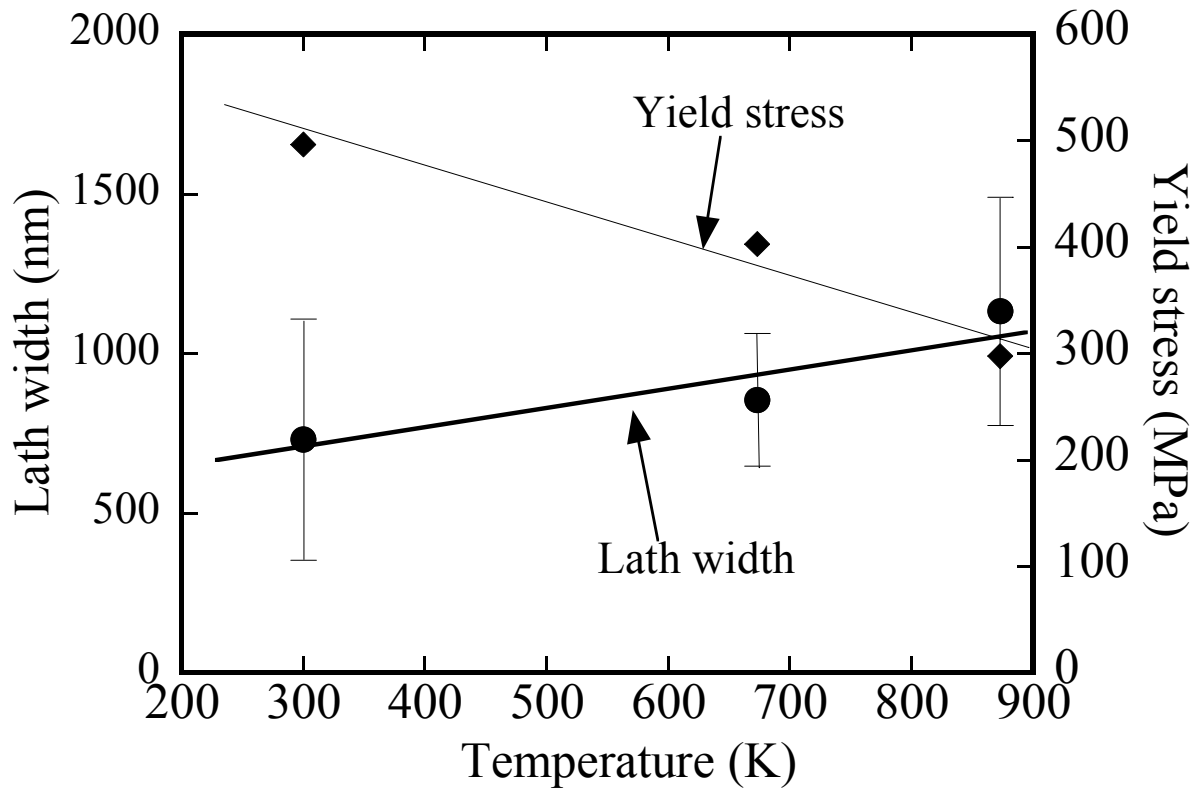


Fig. 3.3.2-1 Change in YS and lath width against temperature.

3.4 Summary

Tensile tests of JLF-1 steel was carried out at strain rate of 0.1%/s and 0.02%/s in vacuum at RT — 873 K. Results are summarized as follows:

- The strain rate does not affect YS, UTS and RA as far as the tests performed in this study. The tensile property of JLF-1 steel is comparable to that of F82H at elevated temperature.
- Strain hardening of JLF-1 steel decreased significantly above 673 K, which caused little difference of YS and UTS at 873 K. The mechanism is considered as the climbing of edge dislocation and cross gliding of screw dislocation become easy at high temperature.
- With strain hardening decreased, RA also increased rapidly above 673 K; and the surface fractography was changed from shear fracture below 673 K to dimple fracture at 773 K and 873 K. That means JLF-1 steel becomes near to be a perfect elastic-plastic body (smaller strain hardening) and ductility improved with temperature increase.
- The YS decreased and lath width increased with temperature. The YS and lath width could imply qualitative relationships with temperature.

Chapter 4 Fatigue Test and Microstructural Analysis

LCF tests of JLF-1 steel with total strain of $\Delta\varepsilon_t=0.6\%\sim 2.4\%$ were carried out in vacuum under a fully reversed push-pull triangular wave with strain rate of 0.1 %/s at RT, 673 K, and 873 K. According to the location of crack relative to the gage trace, three type crack can be defined (Fig. 4-1)[83]: Type A cracked inside the gage length and Type B cracked at the edge of the extensometer. Type C means a fatigue crack outside the gage length.

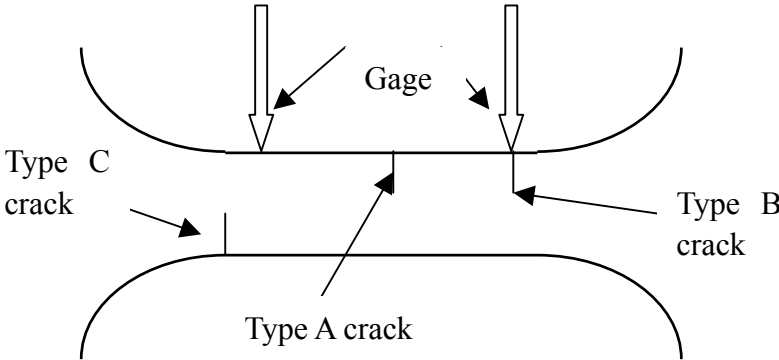


Fig. 4-1 Definition of crack type.

After LCF test, some specimens were selected to investigate the microstructural change with TEM. The LCF test, microstructure analysis items, and crack type are listed in Table 4-1.

Table 4-1 LCF test and microstructure analysis items.

Temp.	Total strain range						
	2.4%	2.0%	1.8%	1.4%	1.0%	0.8%	0.6%
RT	—	●A	●■A	—	●A	—	●A
673 K	●A	—	●■A	●A	●A	●A	●A
873 K	●A	—	●■A	●A	●A	●A	●A

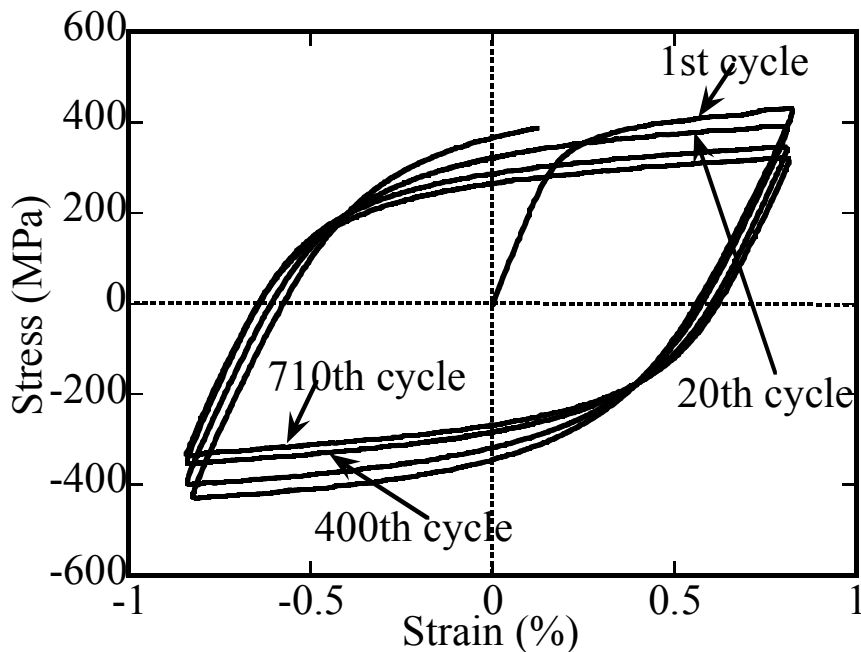
- LCF test was carried out;
- Microstructure was analysed with TEM.

4.1 Temperature effect on fatigue life and the mechanism

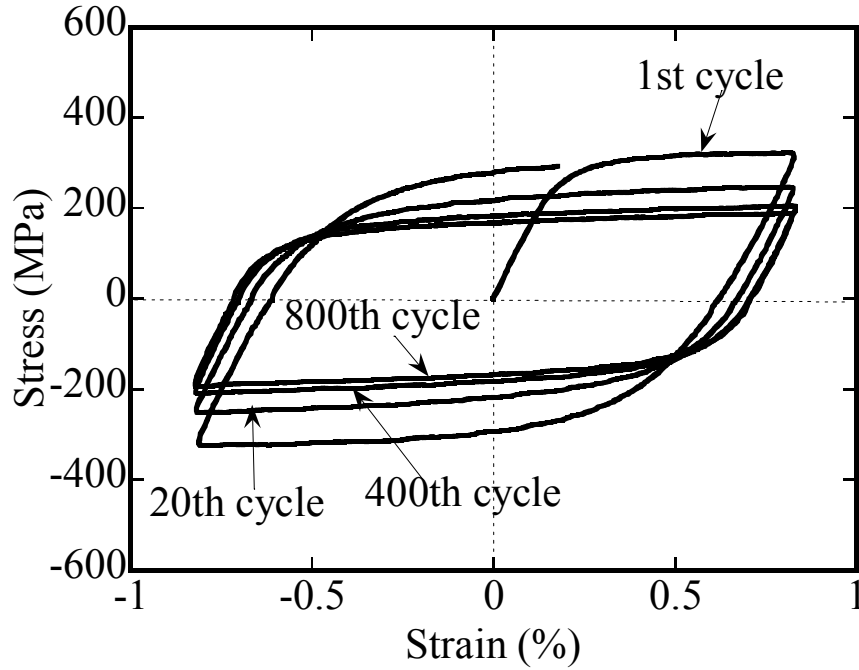
4.1.1 Fatigue stress-strain hysteresis curve

The stress-strain hysteresis curves of $\Delta\varepsilon_f=1.8\%$ at 673 K and 873 K are shown in Fig.4.1-1. The amplitude of stress range decreased and plastic strain range increased with fatigue test going at both temperatures. It means cyclic softening happened. The strain hardening also decreased with temperature, similar to tensile test, little strain hardening was observed at 873 K.

The difference of peak stress for 400th and 710th cycle was less than that for 1st and 20th cycle (the 400th cycle was around half life) at 673 K. Same phenomenon was also observed in Fig.4.1-1 (b). That means the “to-and-fro” moving of dislocation was stable after a certain cycles in the fatigue test. For this reason, the following analyses were focused on the around half life cycle of fatigue tests.



(a) 673 K.



(b) 873 K.

Fig. 4.1.1-1 Stress-strain hysteresis curves of $\Delta\varepsilon_t=1.8\%$ at 673 K (a) and 873 K (b).

4.1.2 Relationship between fatigue life and total strain range at high temperature

The relationships between fatigue life (N_f) vs. total strain range ($\Delta\varepsilon_t$), and stress range ($\Delta\sigma$) are shown from Fig. 4.1.2-1 and Fig. 4.1.2-2 (the data of “RT, 0.4 %/s, Air” were taken from [83]). The total strain range and stress range were obtained from hysteresis curves at around the half of fatigue life ($N_f/2$). The fatigue life at elevated temperature was almost same as that at RT when the life was plotted against the total strain range (Fig. 4.1.2-1). According to equation 1.5.1-5, the $\Delta\varepsilon_t - N_f$ regression curves of JLF-1 at RT, 673 K and 873 K were expressed as follows:

$$\text{RT [83]: } \Delta\varepsilon_t = 91.02 N_f^{(-0.5965)} + 1.023 N_f^{(-0.09462)} \quad (4.1-1)$$

$$673 \text{ K: } \Delta\varepsilon_t = 37.05 N_f^{(-0.4746)} + 0.7209 N_f^{(-0.08571)} \quad (4.1-2)$$

$$873 \text{ K: } \Delta\varepsilon_t = 36.05 N_f^{(-0.4382)} + 0.3809 N_f^{(-0.06148)} \quad (4.1-3)$$

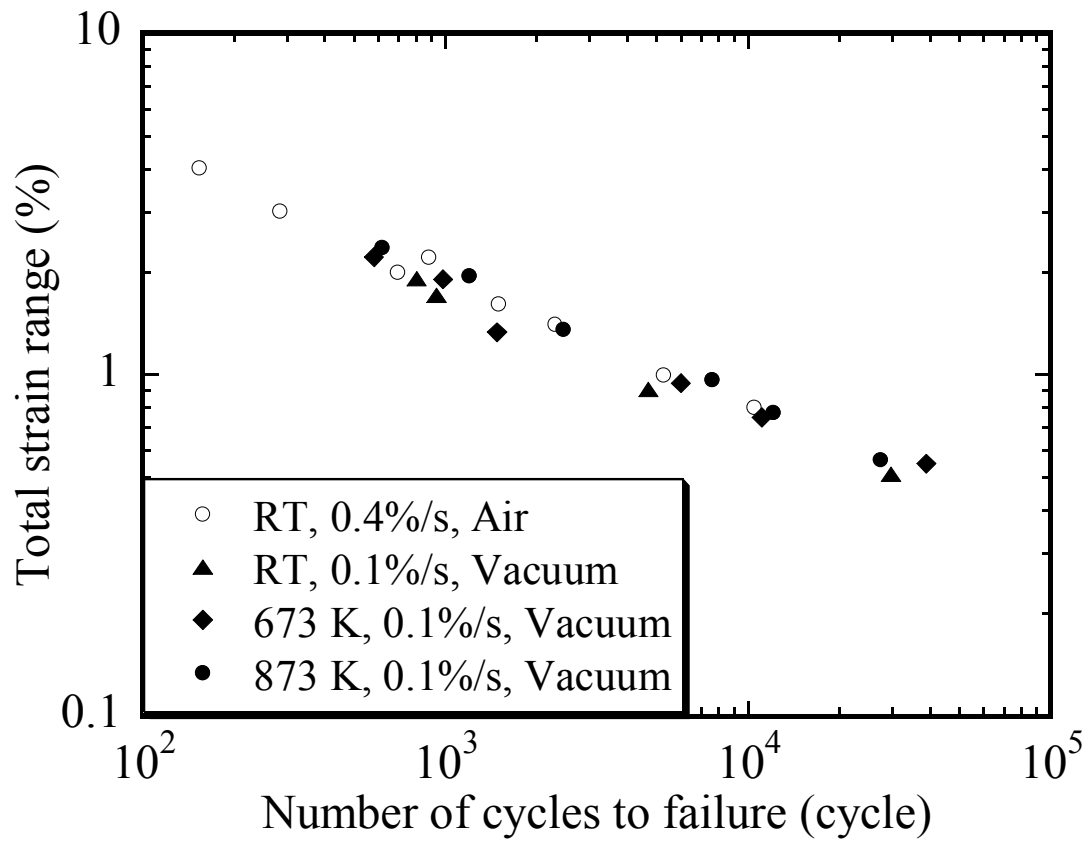


Fig.4.1.2-1 Fatigue life of JLF-1 at RT, 673 K and 873 K in vacuum.

When the life is plotted against the stress range (Fig.4.1.2-2), the temperature effect is clear. With increasing the temperature, the stress level decreased.

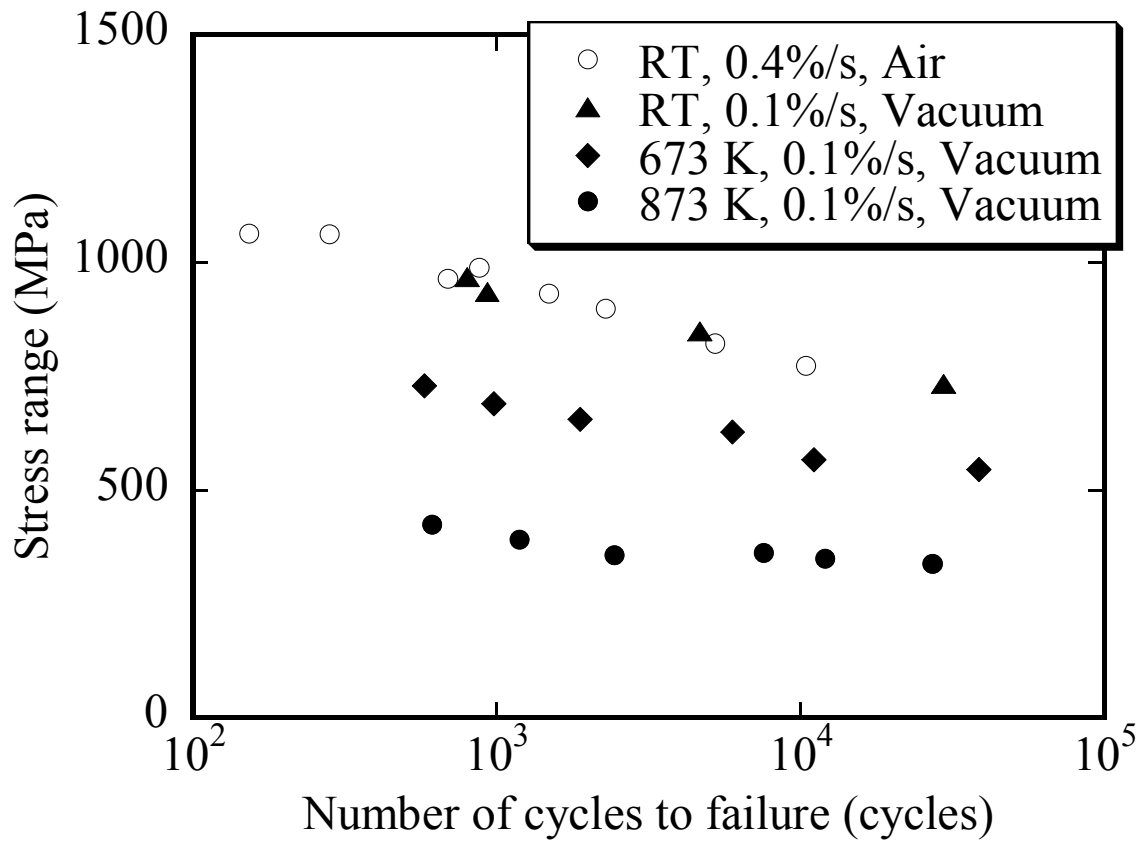


Fig.4.1.2-2 Relationship between stress range and fatigue life.

The comparison of fatigue life of JLF-1 and F82H, plotted against total strain range, was shown in Fig.4.1.2-3. The fatigue life of JLF-1 is comparable to that of F82H at elevated temperature. The $\Delta\varepsilon_t - N_f$ relationship of F82H was also temperature independence when temperature is below 773 K [81]. When temperature was above 873 K, a large reduction in fatigue life of F82H was observed. For JLF-1 steel, such reduction in fatigue life was not observed.

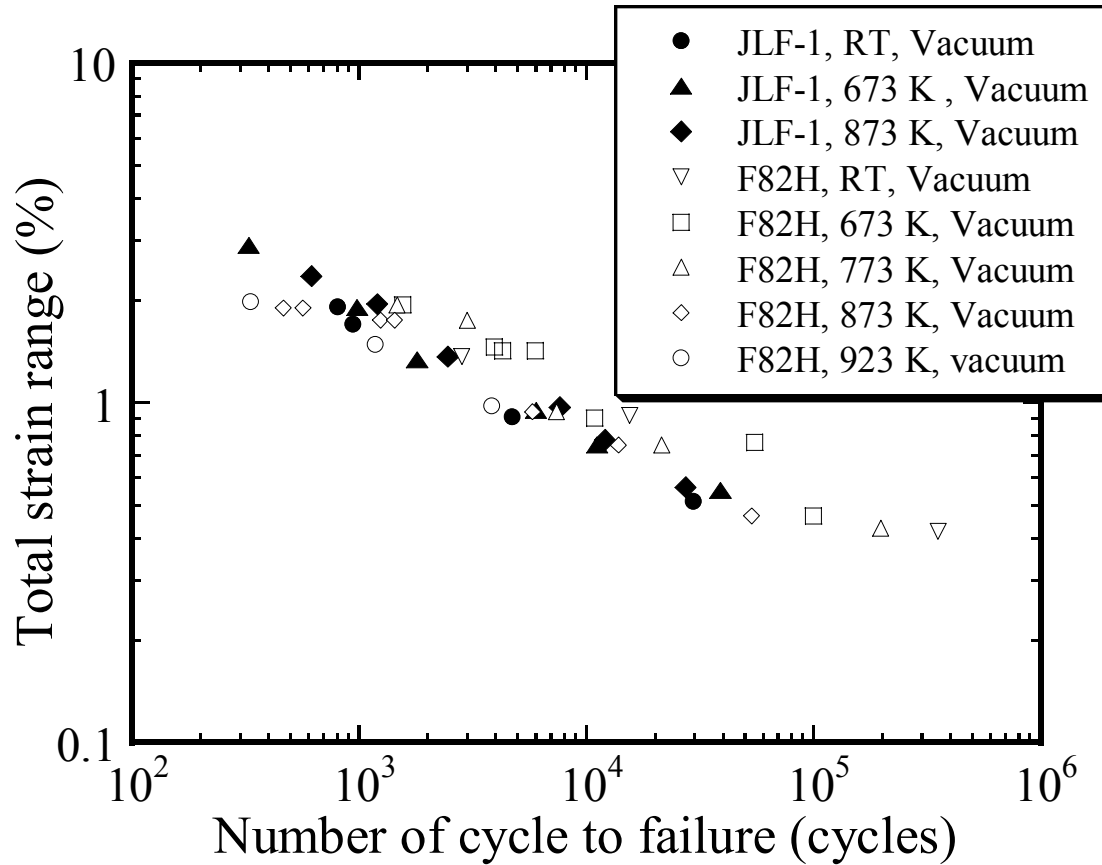


Fig.4.1.2-3 Comparison of fatigue life of JLF-1 and F82H [81] when plotted against total strain range at RT and elevated temperature.

4.1.3 Temperature effect on relationship between fatigue and plastic strain range

However, the temperature effect on the fatigue life of JLF-1 is significant when fatigue life is plotted against plastic strain range.

The static analysis of plastic strain range ($\Delta\varepsilon_p$) and fatigue life (N_f) of JLF-1 is performed according to [98], in which the fatigue life is assumed as log-normally distributed. The Manson-Coffin relationship can be expressed as

$$\log(N_f) = A + B \log(\Delta\varepsilon_p) \quad (4.1.3-1)$$

The recommended expression for estimating the variance (δ) of the normal distribution for $\log(N_f)$ is

$$\delta = \sqrt{\frac{\sum_{i=1}^k [\log(N_f)_i - \log(\hat{N}_f)_i]^2}{k-2}} \quad (4.1.3-2)$$

where k is the total number of test specimen, $\log(\hat{N}_f)_i$ is calculated for equation (4.1.3-1) when plastic strain range is $(\Delta\varepsilon_p)_i$.

The exact confidence band could be calculated using following equation:

$$A + B \log(\Delta\varepsilon_p) \pm t_p \delta \left[\frac{1}{k} + \frac{(\log(\Delta\varepsilon_p) - \overline{\log(\Delta\varepsilon_p)})^2}{\sum_{i=1}^k [\log(\Delta\varepsilon_p)_i - \overline{\log(\Delta\varepsilon_p)}]^2} \right]^{1/2} \quad (4.1.3-3)$$

in which the value of t_p is read from [98] for the desired value of P , the confidence level associated with the confidence interval, $\overline{\log(\Delta\varepsilon_p)}$ is the average value by

$$\overline{\log(\Delta\varepsilon_p)} = \sum_{i=1}^k \frac{\log(\Delta\varepsilon_p)_i}{k} \quad (4.1.3-4)$$

The 95% confidence band for the $\log(N_f) - \log(\Delta\varepsilon_p)$ relationship of JLF-1 steel at 673 K and 873 K is shown in Fig 4.1.3-1. The effect of temperature on fatigue life is beyond the 95% confidence band when fatigue life is plotted against the plastic strain range. That means the change in microstructure behavior with temperature has a significant effect on fatigue life.

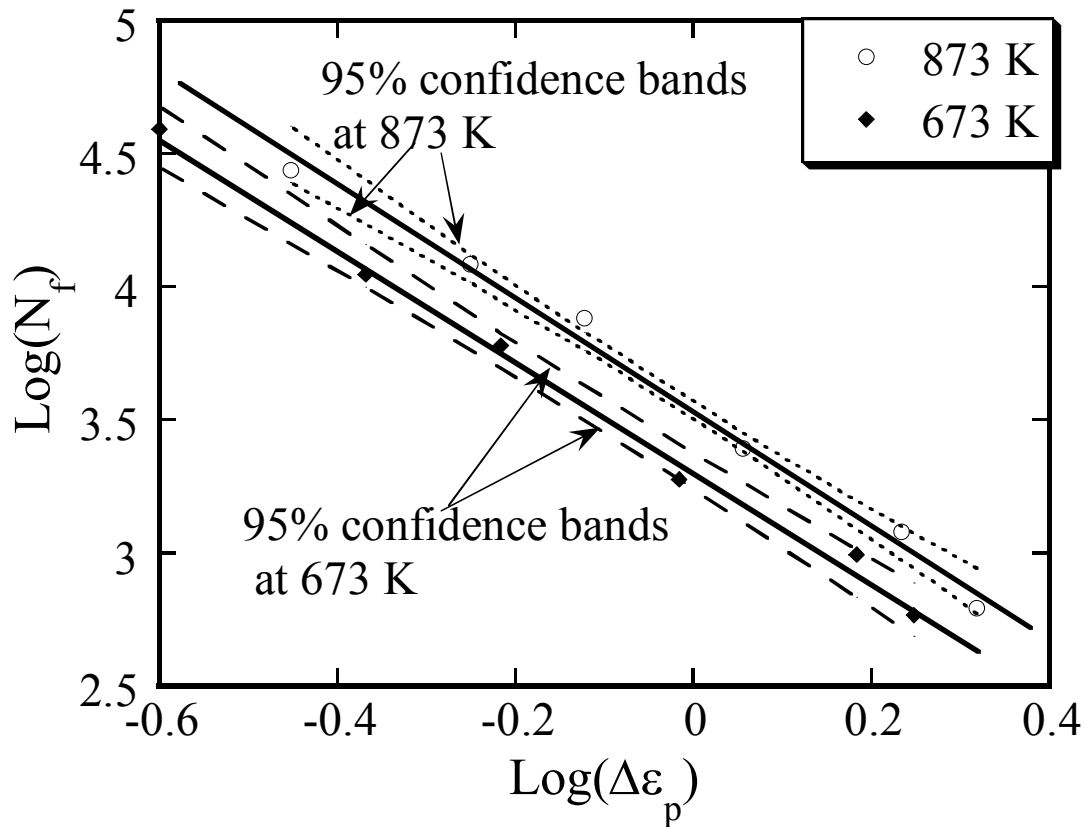


Fig 4.1.3-1 The 95% confidence band for the $\log(N_f)$ — $\log(\Delta\epsilon_p)$ relationship of JLF-1 steel at 673 K and 873 K.

When the fatigue life at RT is considered [83], the fatigue life curves for RT, 673K and 873 K of JLF-1 were on different lines when the life was plotted against the plastic strain range (Fig. 4.1.3-2). It looks that the fatigue life increased with temperature when the plastic strain range is same. This tendency is not agreement with Coffine's model which is independent on temperature when the fatigue life is plotted against the plastic strain range. Thus, it is necessary to investigate the mechanism of this unusual phenomenon.

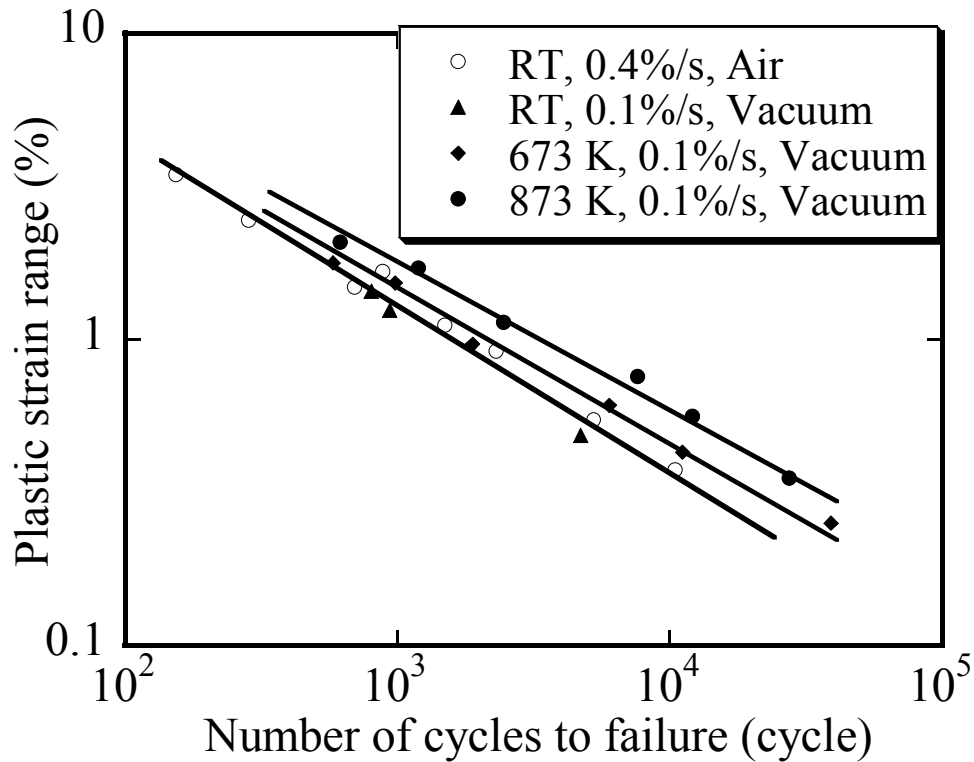


Fig. 4.1.3-2 Relationship between plastic strain range and number of cycles to failure.

4.1.4 Microstructure evolution during cycle plastic deformation

4.1.4.1 Crack initiation

The optical observation of specimen after cyclic plastic deformation at elevated temperature was shown in Fig. 4.1.4.1-1.

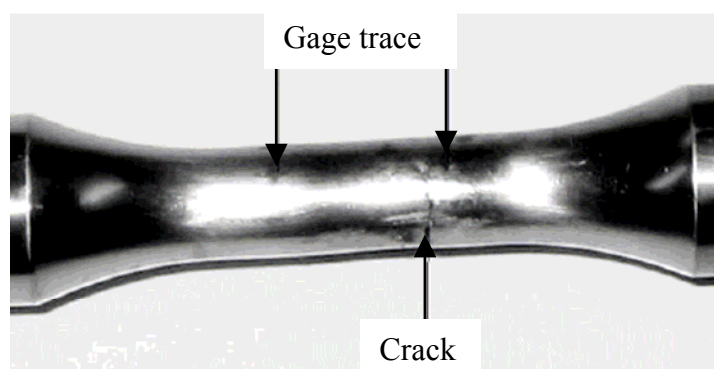
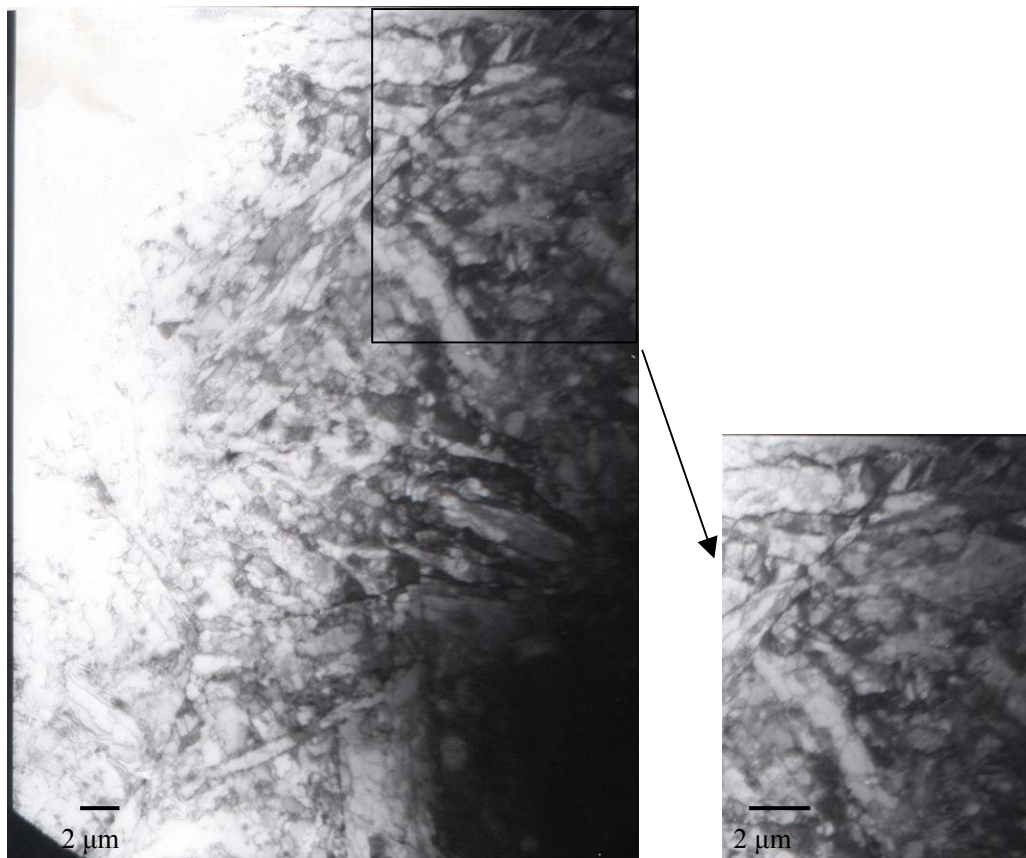


Fig. 4.1.4.1-1 Specimen tested at $\Delta\epsilon_t = 1.4\%$ at 673 K.

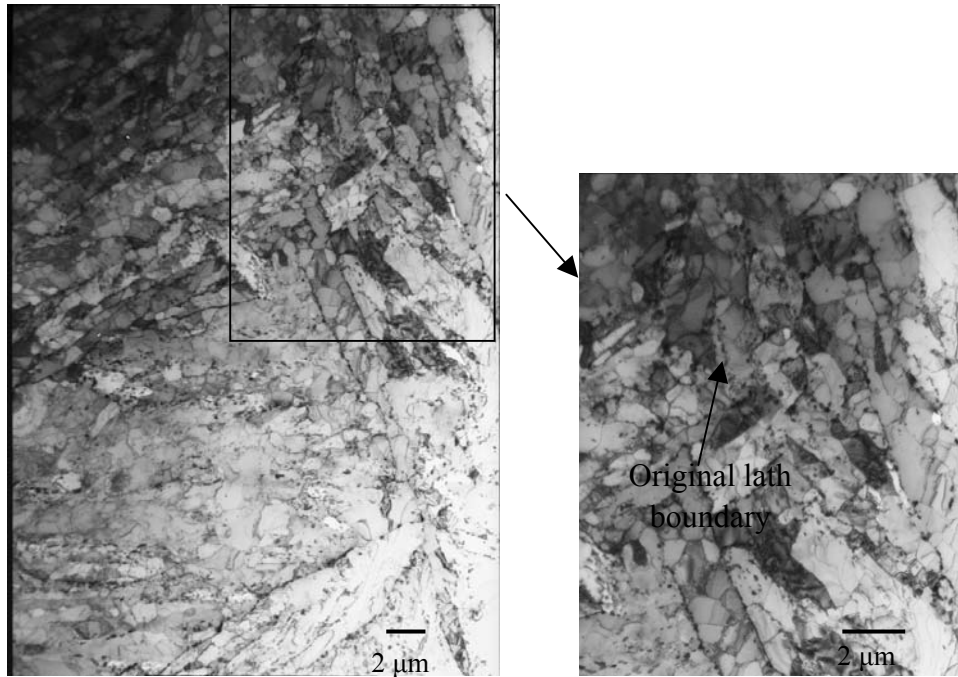
The crack initiated at surface of specimen, which was general phenomenon in fatigue test. So, there should be other reasons to correlate with Fig. 4.1.3-2.

4.1.4.2 Lath width after cyclic deformation

The TEM images of the specimen after fatigue tests of $\Delta\varepsilon_{\tau}=1.8\%$ at RT was shown in Fig.4.1.4.2-1. Compared with the microstructure of JLF-1 steel before fatigue test (Fig 3.2.2-1 (a)), the lath width became wider after fatigue at RT. Assuming that carbides inside the subgrains indicated the position of original lath boundary [99], the microstructures indicated that the partial annihilation of original lath boundary occurred during the cyclic deformation.



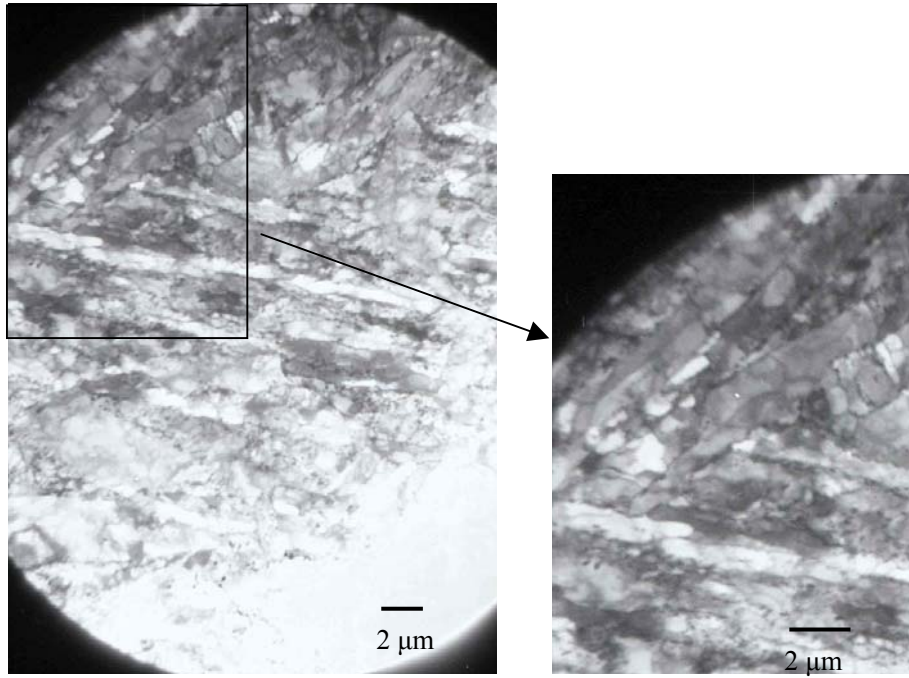
(a) Microstructure of 10th cycle



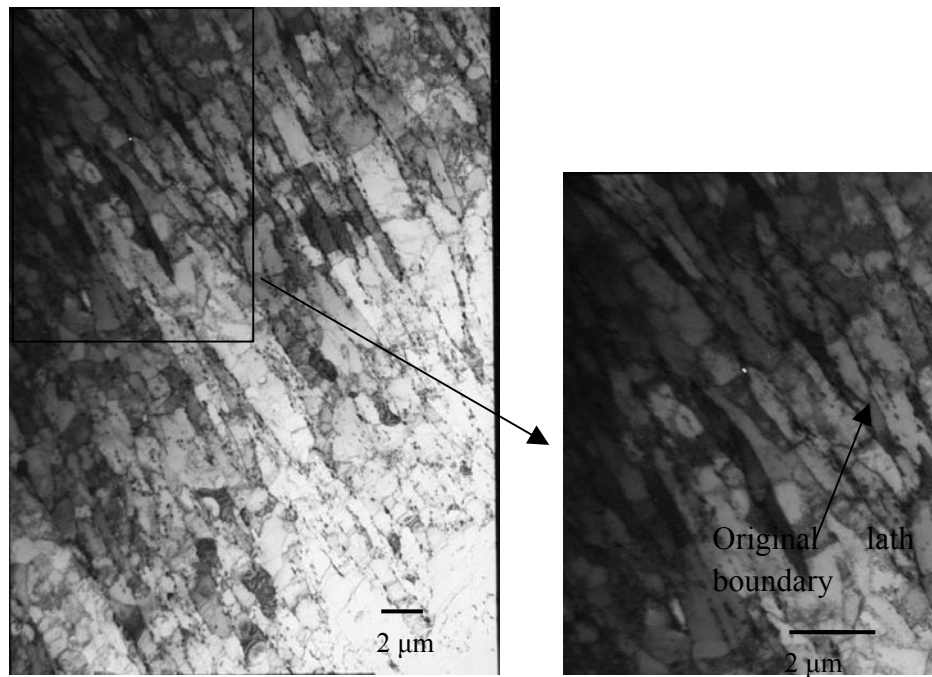
(b) Microstructure after failure

Fig.4.1.4.2-1 Effect of cyclic deformation on microstructure
at $\Delta\varepsilon_{\tau}=1.8\%$ at RT.

The effect of cyclic deformation on microstructure of total strain range $\Delta\varepsilon_{\tau}=1.8\%$ at 673 K was shown in Fig.4.1.4.2-2. The phenomenon of partial annihilation of original lath boundaries was observed obviously after the specimen was failure. Corresponding to this phenomenon, the lath width also increased with cycles.

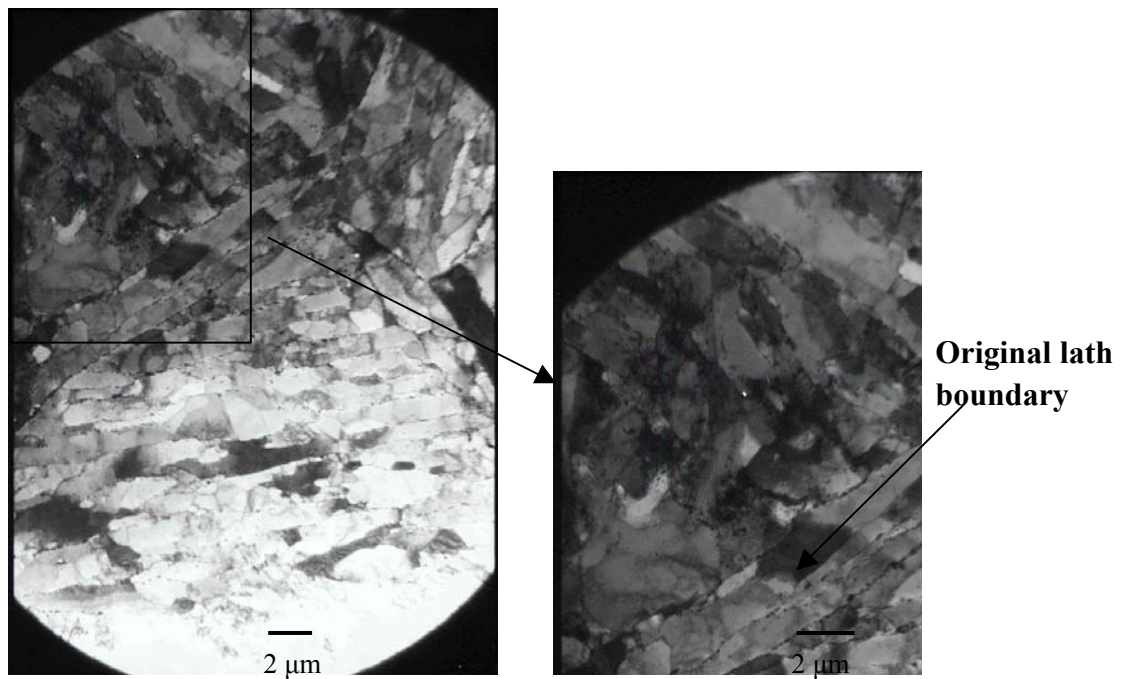


(a) Microstructure of 10th cycle

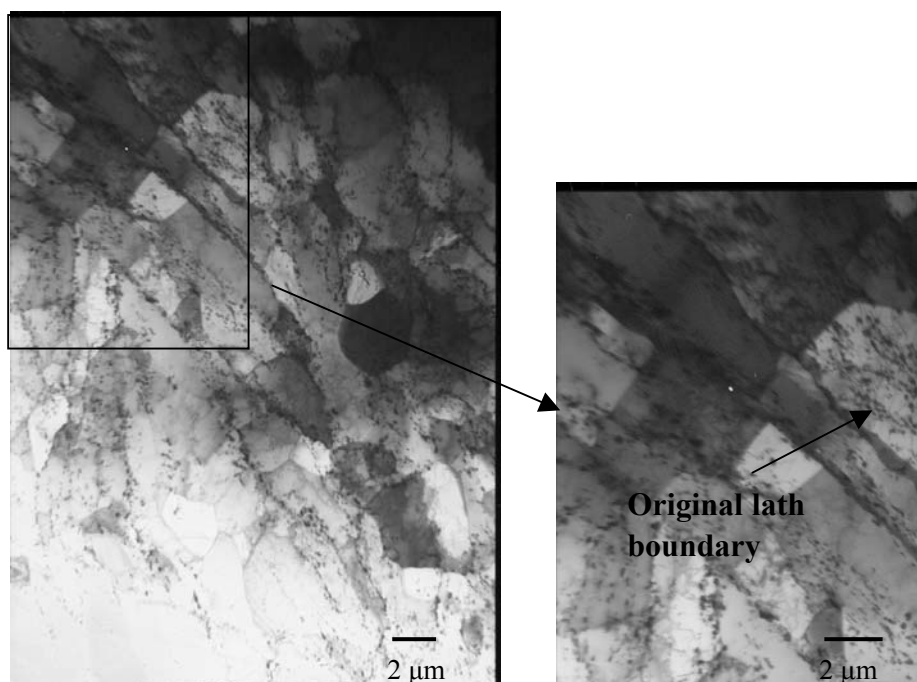


(b) Microstructure after failure.

Fig.4.1.4.2-2 Effect of cyclic deformation on microstructure
at $\Delta\epsilon_t=1.8\%$ at 673 K.



(a) Microstructure of 10th cycle



(b) Microstructure after failure.

Fig.4.1.4.2-3 Effect of cyclic plastic deformation on lath structure
at $\Delta\epsilon_t=1.8\%$ at 873 K.

The microstructure of JLF-1 steel after fatigue test at $\Delta\varepsilon_t=1.8\%$ at 873 K was shown in Fig.4.1.4.2-3. The phenomenon of partial annihilation of original lath boundaries was observed at 10th cycle, and it was enhanced with number of cycles. The lath width also increased with number of cycles.

From TEM images of $\Delta\varepsilon_t=1.8\%$ at RT, 673 K and 873 K, the tendency that partial annihilation of original lath boundaries and resulting increase in lath width was enhanced with temperature.

Beside the cyclic plastic deformation, temperature is the other factor to cause increase in lath width. The microstructure of the thermal history simulating of LCF test of $\Delta\varepsilon_t=1.8\%$, which was 9 hours at 673 K and 10 hours at 873 K, was shown in Fig. 4.1.4.2-4. Compared with Fig. 4.1.4.2-2 and 4.1.4.2-3, the change in lath width was not significant after the thermal history simulating of LCF test.

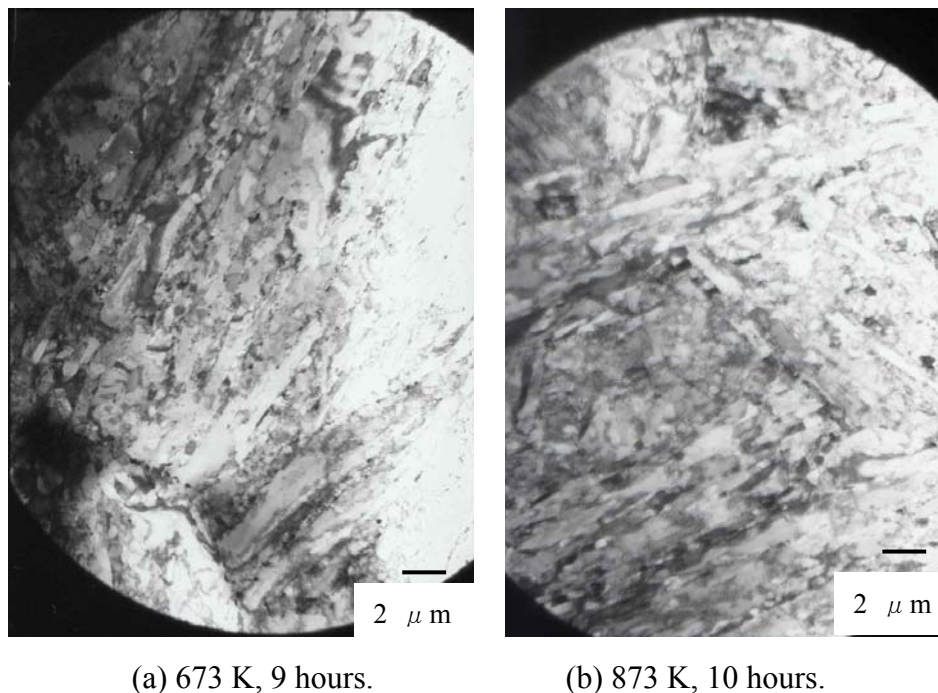
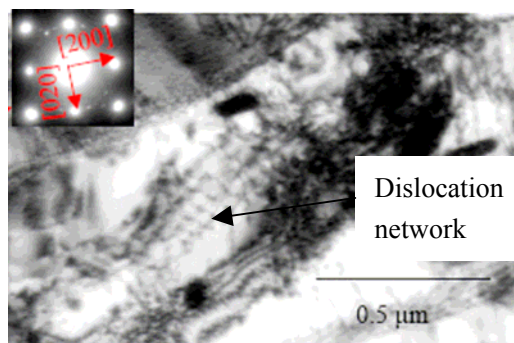


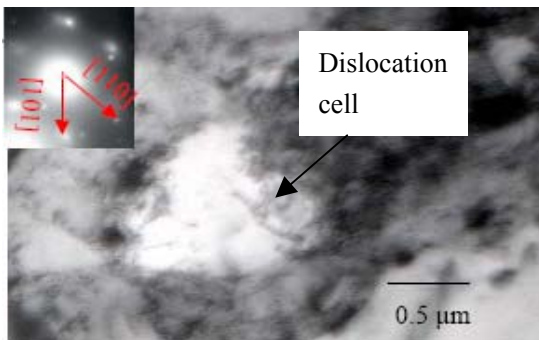
Fig. 4.1.4.2-4 Microstructure of JLF-1 steel after the thermal history simulating of LCF test of $\Delta\varepsilon_t=1.8\%$ at 673 and 873 K.

4.1.4.3 Dislocation structure and strain hardening

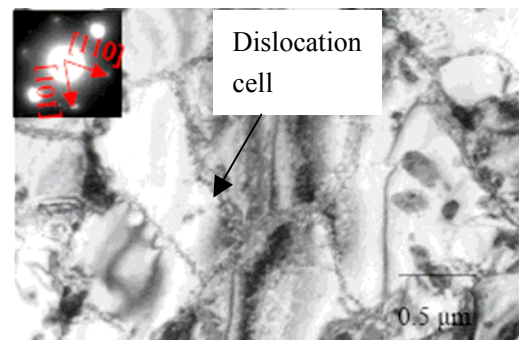
The TEM images of dislocations before and after fatigue at RT were shown in Fig. 4.1.4.3-1, the dislocation density was measured according to [100]. Before fatigue (Fig. 4.1.4.3-1 (a)), the dislocation network was observed, and the dislocation density was very high ($\rho \approx 6.4 \times 10^{14} \text{m}^{-2}$). After fatigue (Fig. 4.1.4.3-1(b) and (c)), the dislocation structure of JLF-1 steel changed from network to cell at RT. The dislocation density reduced with the cyclic deformation (dislocation forming cell structure was not included with counting).



(a) Before fatigue.
($\rho \approx 6.4 \times 10^{14} \text{m}^{-2}$)



(b) 10th cycle at RT, $\Delta \varepsilon_{\tau} = 1.8\%$.
($\rho \approx 1.0 \times 10^{14} \text{m}^{-2}$)



(c) 936th cycle at RT, $\Delta \varepsilon_{\tau} = 1.8\%$.
($\rho \approx 2.3 \times 10^{12} \text{m}^{-2}$)

Fig. 4.1.4.3-1. Effect of cyclic plastic deformation on dislocation structure of $\Delta \varepsilon_{\tau} = 1.8\%$ at RT.

Correlated to the change in dislocation, strong strain hardening was observed at 10th and

900th cycles from the stress-strain hysteresis curves (Fig. 4.1.4.3-2). That means the dislocation tangled to form cell structure during cyclic deformation at RT.

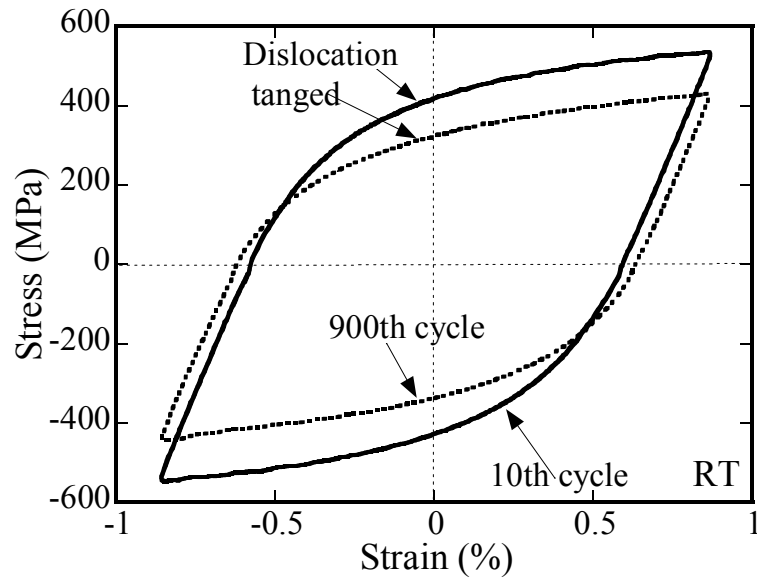
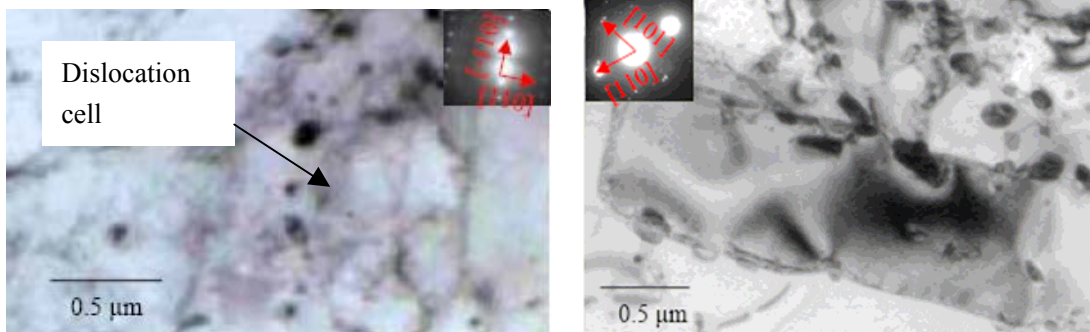


Fig. 4.1.4.3-2 stress-strain hysteresis curve of 10th and 900th cycle of $\Delta\varepsilon_t=1.8\%$ at RT



(a) 10th cycle at 673 K, $\Delta\varepsilon_t=1.8\%$;
($\rho\approx 1.9\times 10^{13}\text{m}^{-2}$)

(b) 716th cycle at 673 K, $\Delta\varepsilon_t=1.8\%$;
($\rho\approx 5.7\times 10^{12}\text{m}^{-2}$)

Fig. 4.1.4.3-3 Effect of cyclic plastic deformation on dislocation structure of $\Delta\varepsilon_t=1.8\%$ at 673 K.

The dislocation structure of 10th and 716th cycle at 673 K was shown in Fig. 4.1.4.3-3. Weak cell structure was observed at 10th cycle. However, the cell structure did not remain during the following fatigue and were observed at the TEM images at 500th cycle and the final

failure at 673 K. The dislocation density at 673 K (Fig. 4.1.4.3-3) was lower than that at RT (Fig. 4.1.4.3-1.), and also reduced by cyclic deformation.

The stress-strain hysteresis curve of 10th and 716th cycle at 673 K was shown in Fig. 4.1.4.3-4. Strain hardening decreased during cyclic plastic deformation, and little strain hardening at 700th cycle. Based on dislocation structure change at 673 K (Fig. 4.1.4.3-3), the dislocation behavior was tangled to form cell structure at original few cycles, then pass through the lath during cyclic plastic deformation.

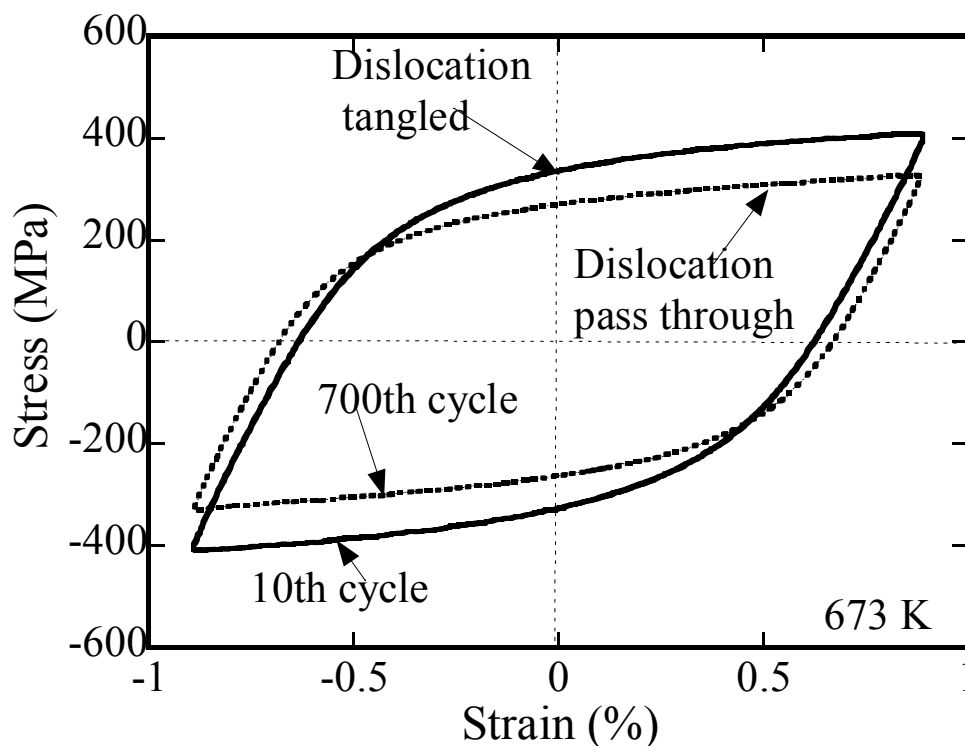
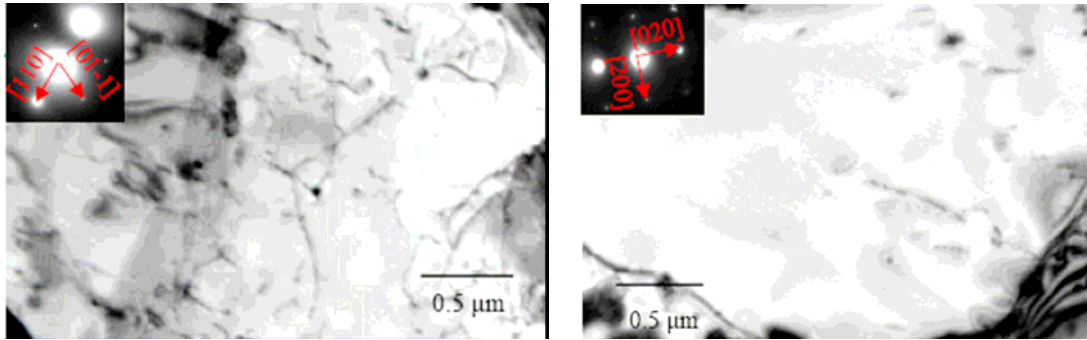


Fig. 4.1.4.3-4 stress-strain hysteresis curve of 10th and 700th cycle of $\Delta\varepsilon_i=1.8\%$ at 673 K.

At 873 K, the cell structure was not observed (Fig. 4.1.4.3-5). The dislocation density decreased with cycles, and was lower than that of 673 K (Fig. 4.1.4.3-3).

The stress-strain hysteresis curve of 10th and 800th cycle at 873 K was shown in Fig. 4.1.4.3-6. Little strain hardening was observed at 10th and 800th cycle. Based on the dislocation structure change (Fig. 4.1.4.3-5), the dislocation pass through the lath during cyclic deformation at 873 K.



(a) 10th cycle at 873 K, $\Delta\epsilon_{\dot{\tau}}=1.8\%$.
 $(\rho \approx 1.1 \times 10^{13} \text{m}^{-2})$

(b) 851st cycle at 673 K, $\Delta\epsilon_{\dot{\tau}}=1.8\%$.
 $(\rho \approx 1.3 \times 10^{12} \text{m}^{-2})$

Fig. 4.1.4.3-5 Effect of cyclic plastic deformation on dislocation structure of $\Delta\epsilon_{\dot{\tau}}=1.8\%$ at 873 K.

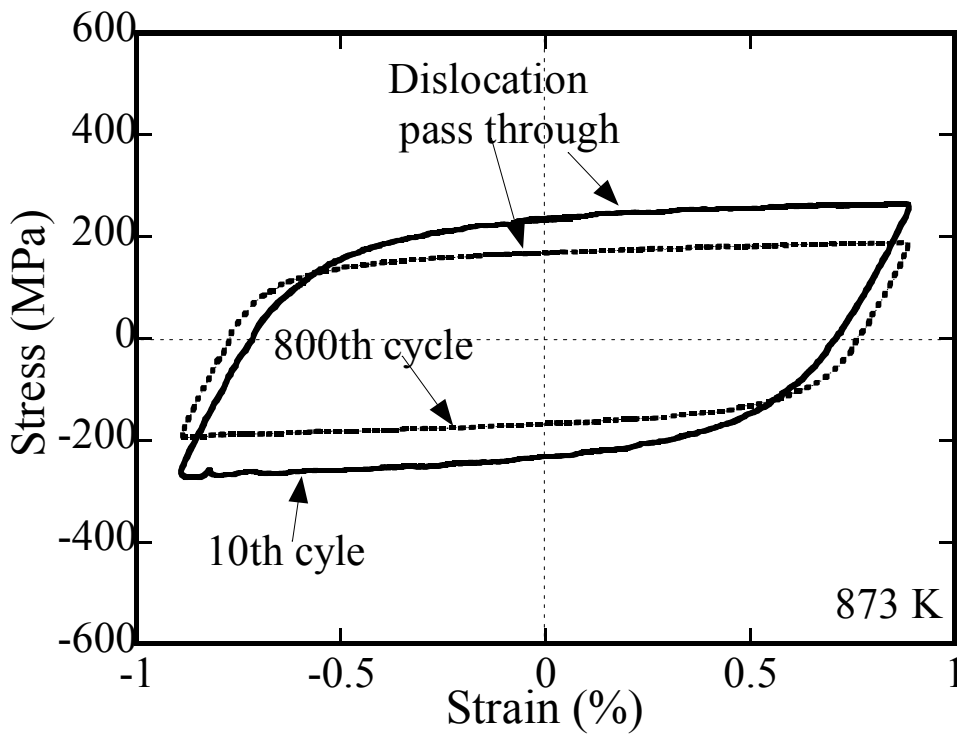


Fig. 4.1.4.3-6 stress-strain hysteresis curve of 10th and 800th cycle of $\Delta\epsilon_{\dot{\tau}}=1.8\%$ at 873 K.

4.1.4.4 mechanism of temperature effect on $\Delta\varepsilon_p - N_f$ relationship

The microstructure evolution during cyclic deformation can be summarized as:

1) Dislocation interaction is dependent on temperature. The change in dislocation density during cyclic plastic deformation at RT, 673 K and 873 K is shown in Fig. 4.1.4.4-1.

At RT, dislocation rearrangement to form cell structure and keeping high density.

At 673 K, dislocation density decreases to medium level.

At 873 K, dislocation decreases to level.

2) Lath width increases with temperature during cyclic plastic deformation.

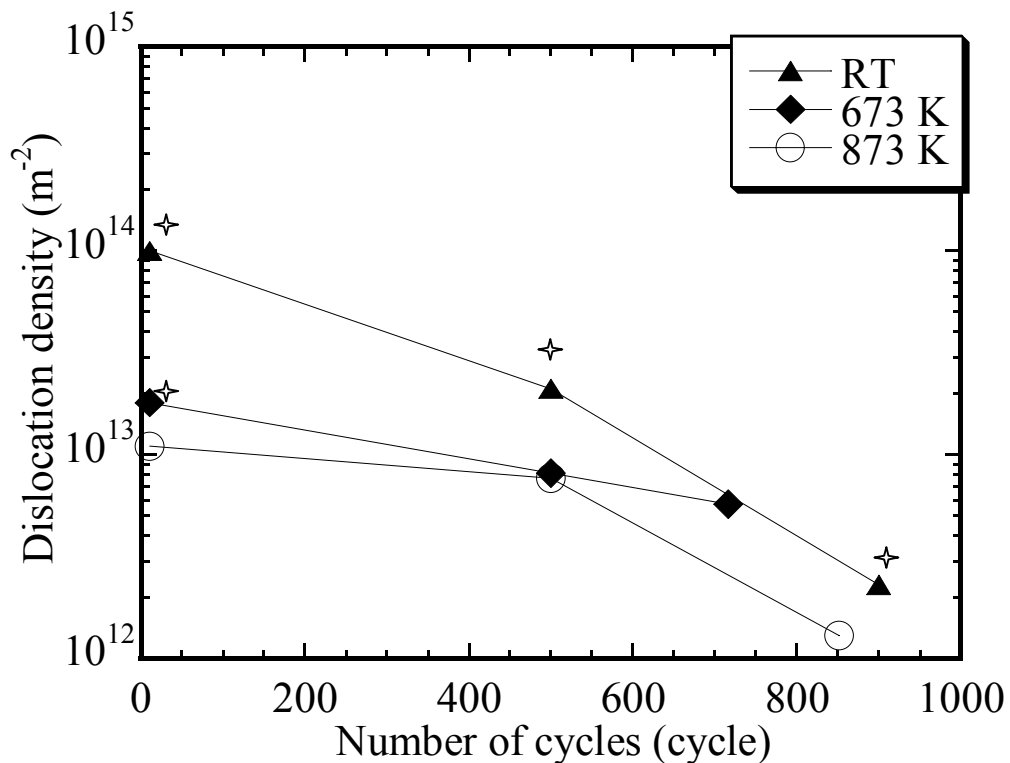


Fig. 4.1.4.4-1 Change in dislocation density during cyclic plastic deformation of $\Delta\varepsilon_t=1.8\%$ at RT, 673 K and 873 K (\star means dislocation cell was observed).

Based on the results of microstructure analysis, it is concluded that the loss of dislocation pile up will result in reduction of strain hardening at high temperature. Thus, the fatigue life is

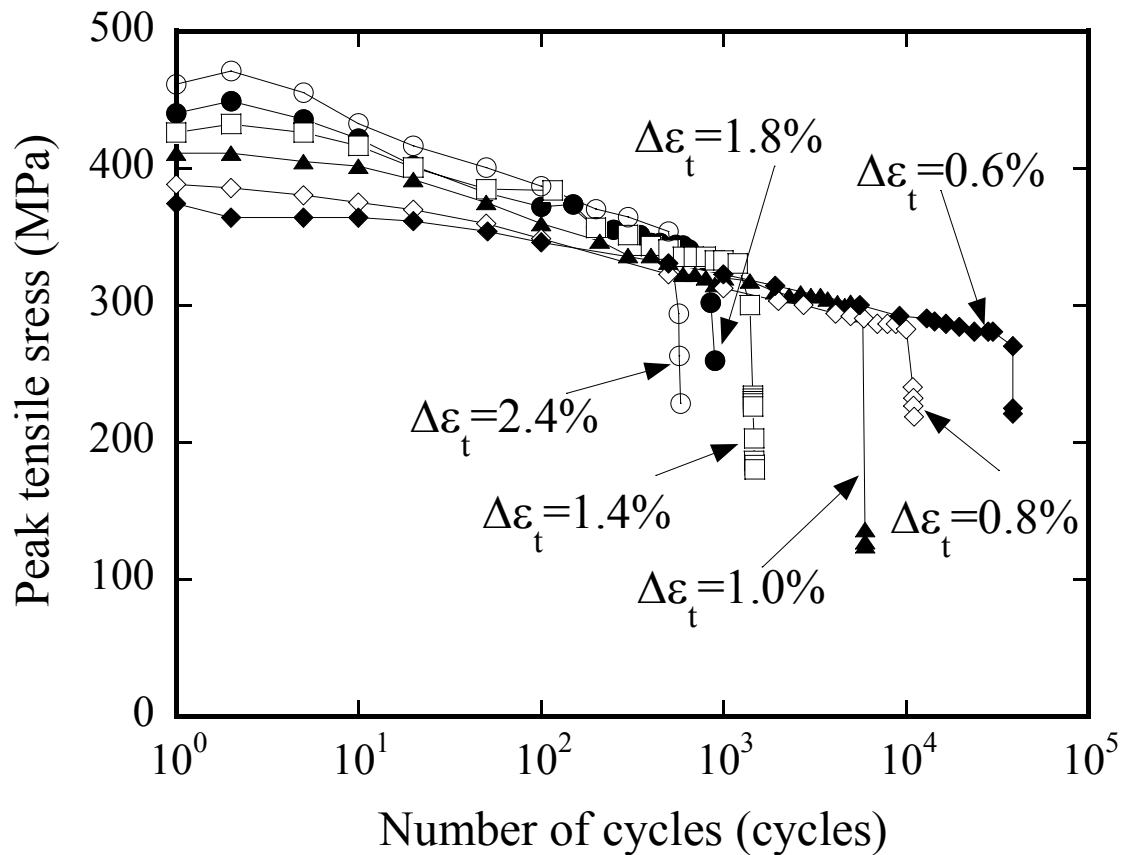
longer at high temperature when plotted against the plastic strain range (Fig. 4.1.3-2).

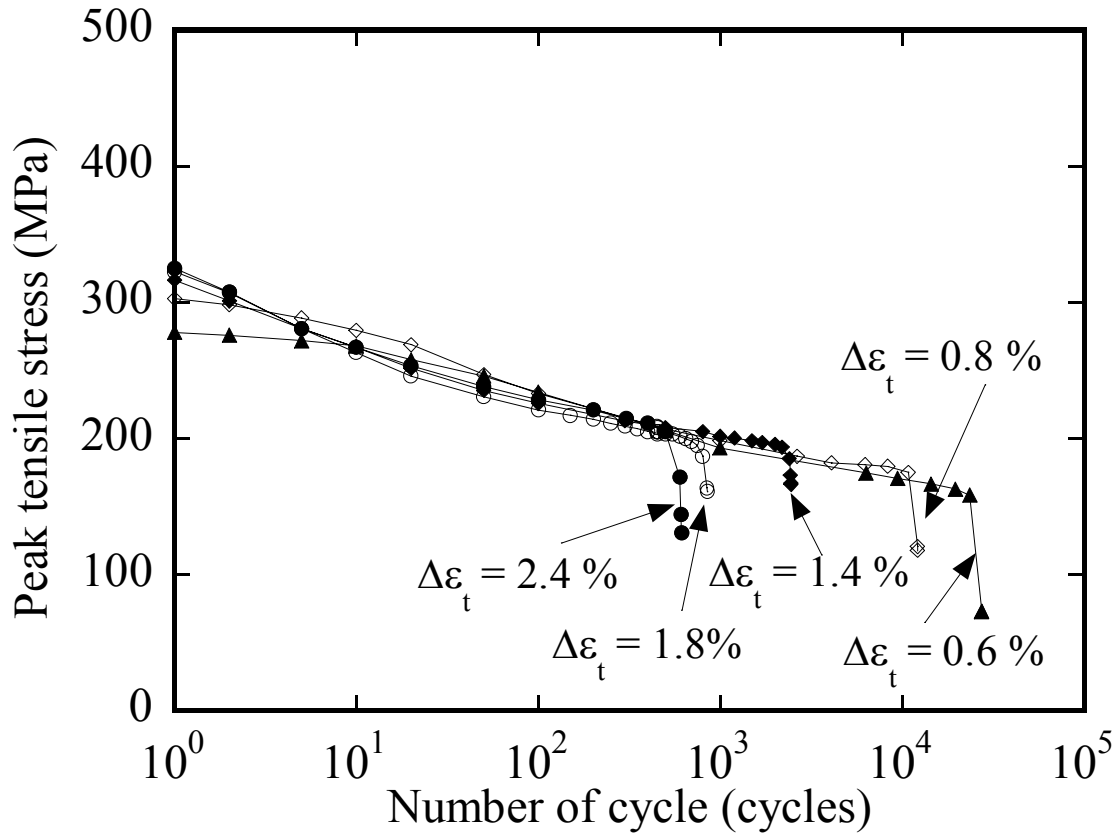
The total strain range ($\Delta\varepsilon_t$) is the sum of plastic strain range ($\Delta\varepsilon_p$) and elastic strain range ($\Delta\varepsilon_e$). With regards to fatigue lives, the $\Delta\varepsilon_e - N_f$ and $\Delta\varepsilon_p - N_f$ relationship depend on temperature. If the temperature effect on $\Delta\varepsilon_p - N_f$ relationship can be compensated by that on $\Delta\varepsilon_e - N_f$ relationship, the $\Delta\varepsilon_t - N_f$ relationship does not depend on temperature. Thus, little effect of temperature on $\Delta\varepsilon_t - N_f$ relationship of JLF-1 steel was obtained in Fig .4.1.2-1.

4.2 Cyclic softening and the mechanism

Similar to F82H [81] and Eurofer 97 [78], JLF-1 showed cyclic softening at RT, 673 K (after initial cyclic hardening) and 873 K during LCF test in vacuum.

The change in tensile peak stresses during the fatigue process at 673 K and 873 K was shown in Fig. 4.2-1. The peak stresses increased initially and then decreased gradually until the final failure at 673 K when $\Delta\varepsilon_t$ was over 1.4% (Fig. 4.2-1 (a)), which demonstrated the initial cyclic hardening and followed by cyclic softening. This phenomenon was also reported in case of JLF-1 at RT in air, which was considered to be due to dislocations piled up with tangling [83]. At 873 K, only cyclic softening was observed (Fig. 4.2-1 (b)).





(b) 873 K.

Fig. 4.2-1 Change in tensile peak stresses during fatigue tests at 673 K (a) and 873 K (b).

Change in peak tensile stress during fatigue test at RT, 673 K and 873 K at a total strain range $\Delta\epsilon_t=1.8\%$ is shown in Fig. 4.2-2. In section 4.1.4, TEM images of JLF-1 steel, before and after fatigue test at $\Delta\epsilon_t=1.8\%$ at RT, 673 K and 873 K, showed that the cyclic plastic deformation caused the change in microstructure, such as the increment of lath width and partial annihilation of original lath boundary, reduction of dislocation density, and formation and loss of cell structure. The change in microstructure will affect the cyclic softening property of material [95, 96, 101-103]. Thus, the effect of lath width, dislocation density and cell structure on cyclic softening should be investigated.

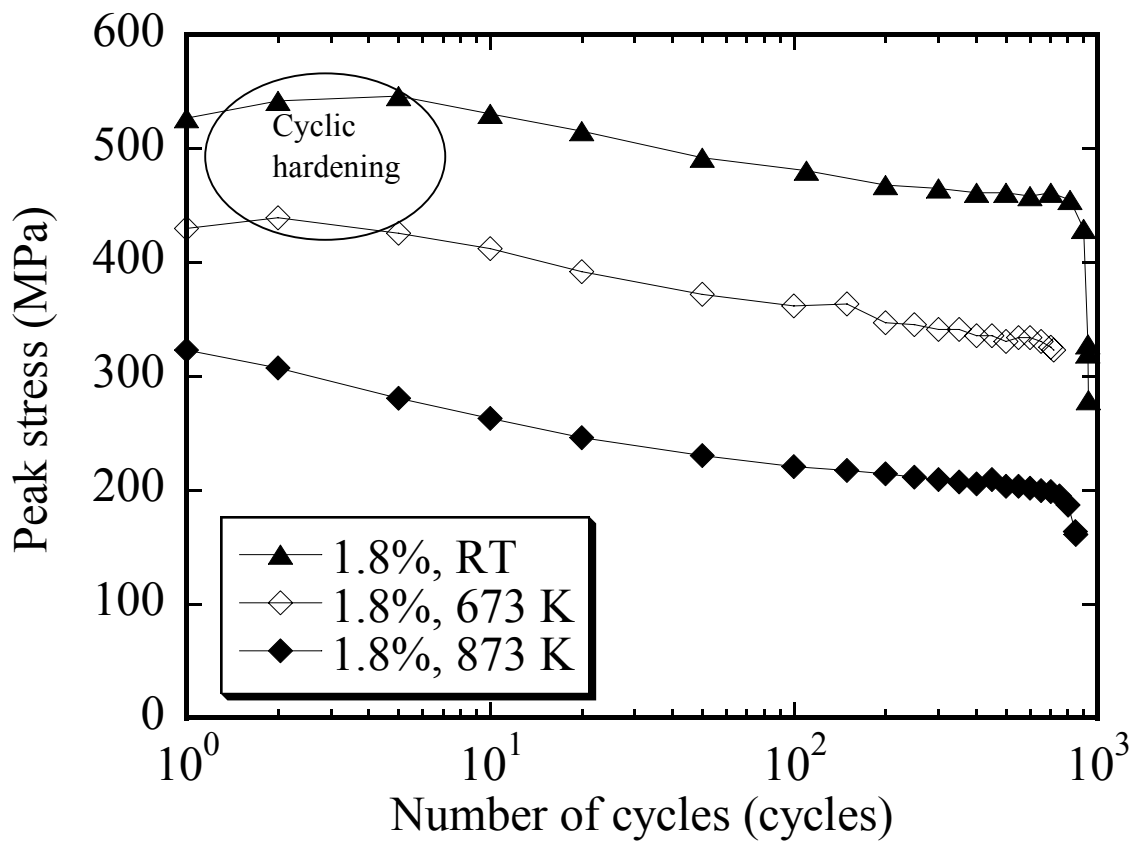


Fig. 4.2-2 Change in peak stress during fatigue at RT, 673 K and 873 K at a total strain range $\Delta\epsilon_t=1.8\%$.

4.2.1 Lath width and dislocation cell structure effect on cyclic softening

The effect of tensile, fatigue and thermal history simulation on lath width was shown in Fig. 4.2.1-1. Among the static plastic deformation, cyclic plastic deformation and temperature, the cyclic plastic deformation has the strongest effect on increase in lath width.

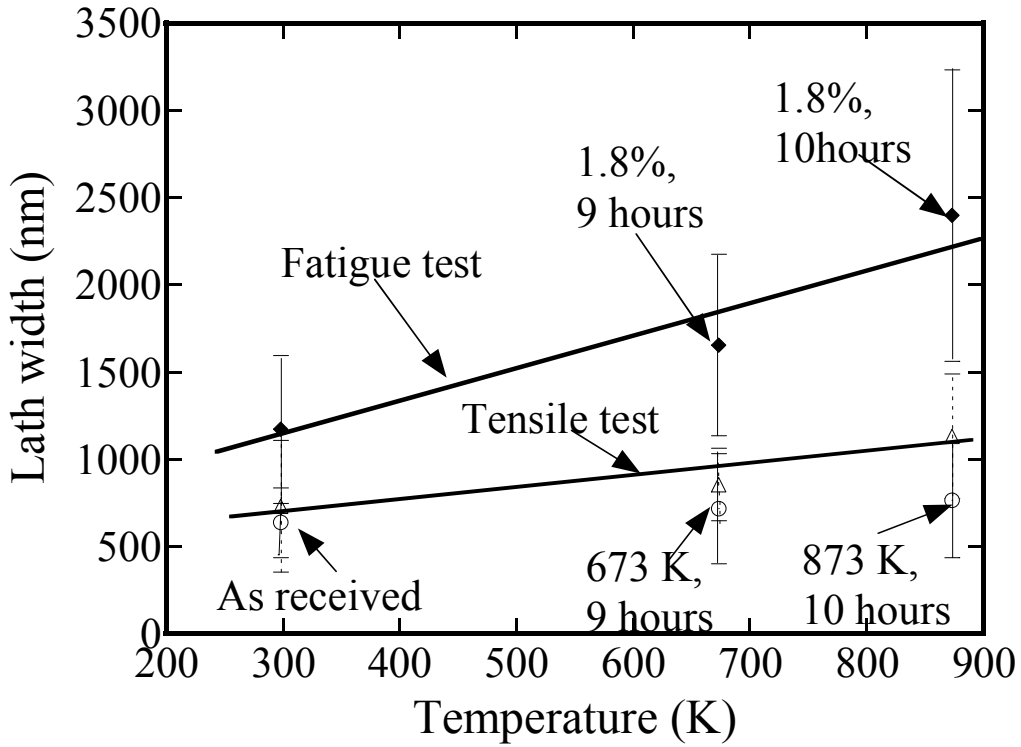


Fig. 4.2.1-1 Change in lath width against temperature after tensile and fatigue at RT, 673 K and 873 K, and thermal history simulating of LCF test at 673 K and 873 K.

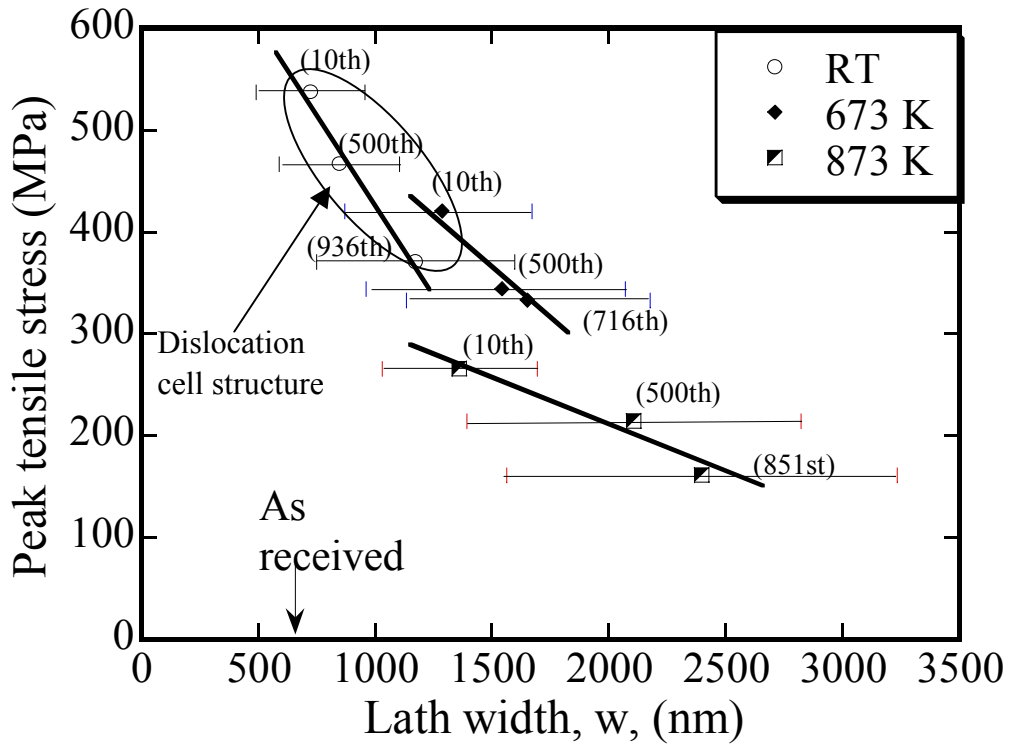


Fig. 4.2.1-2 Peak tensile stress as a function of lath width at $\Delta\epsilon_t=1.8\%$ at RT, 673 K and 873 K.

The change in peak tensile with lath width at $\Delta\varepsilon_t=1.8\%$ at RT, 673 K and 873 K was shown in Fig. 4.2.1-2. The data showed a tendency for the peak stress to decrease with lath width increasing during a fatigue test. The peak tensile stress and lath width appeared to correlate with the number of cycles at RT, 673 K and 873 K. Thus, cyclic softening is correlated with lath width

In present study, the dislocation cell structure also deformed by the cyclic plastic deformation (formed at RT, formed and lost at 673 K, and not formed at 873 K). The evolution of dislocation cell structure also affected the cyclic softening in Fig. 4.2.1-2.

4.2.2 Dislocation density effect on cyclic softening

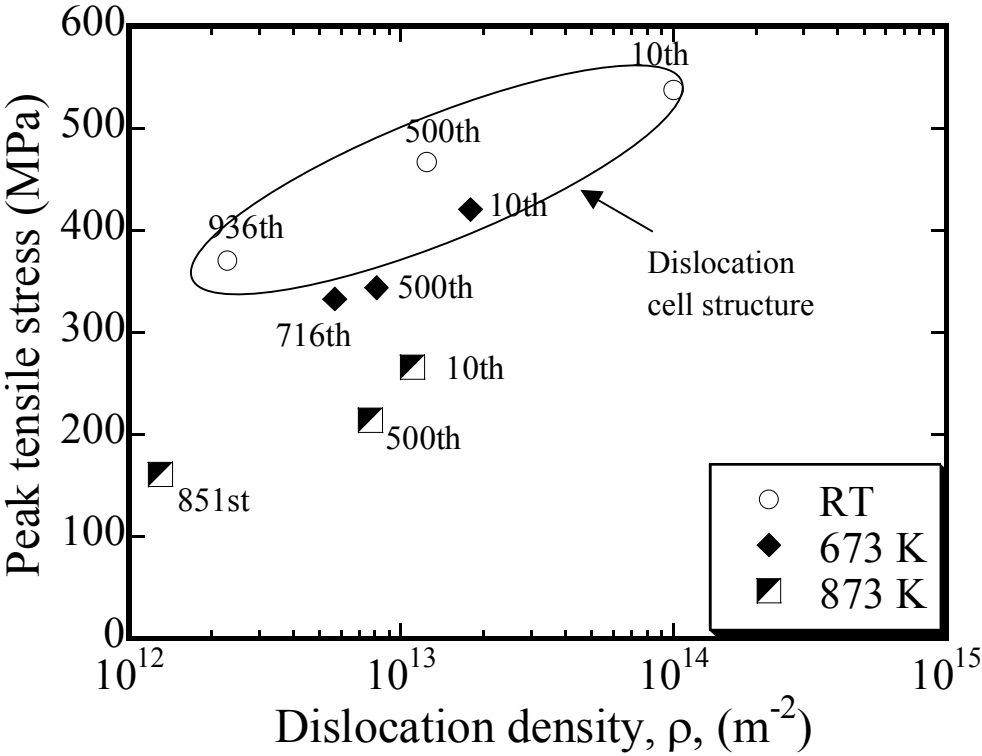


Fig. 4.2.2-1 Change in peak stress with dislocation density at $\Delta\varepsilon_t=1.8\%$ at RT, 673 K and 873 K.

The change in peak stress with dislocation density at $\Delta\varepsilon_t=1.8\%$ at RT, 673 K and 873 K was shown in Fig. 4.2.2-1. The peak tensile stress decreased with decrease in dislocation density during cyclic deformation. That means decrease in dislocation density is another

reason for cyclic softening.

Based on the above analysis, it could be concluded that cyclic softening of JLF-1 is caused by reduction in dislocation density, formation and loss of cell structure, and increment of lath width.

4.3 Hardness test results

Mechanical properties of materials are originated by their microstructure. The microscopic mechanism on mechanical properties is useful for getting opinions to improve the materials. “Vickers Hardness” is the common property to be correlated with microstructures using dislocation mechanism. Thus correlation of “Vickers Hardness” and microstructure for the present experiment is investigated to get mechanistic understanding on the mechanical property change such as fatigue life and cyclic softening.

Neutron irradiation produces significant changes in the mechanical and physical properties of RAF/M steel raising feasibility question and design limitation because neutron irradiation induces atomic displacement and subsequent defect formation and microstructure evolution, which induce change in the mechanical property. Thus, the correlation between microscopic mechanisms on mechanical property change is also benefic to understand radiation effects on mechanical property of the material and get opinions to develop radiation-resistant materials.

Vickers Hardness test of JLF-1 steel was performed with 1 kg in load and 30 seconds in holding time at RT.

The lath width effect on hardness was shown in Fig. 4.3-1. The hardness correlated the lath width in the case of no cell structure. The dislocation cell structure influenced the hardness when it existed.

The relationship between hardness and dislocation density was shown in Fig. 4.3-2. Decrease in dislocation density caused the reduction in hardness.

Thus, the lath width, dislocation density, and dislocation cell structure will correlate to Vicker hardness.

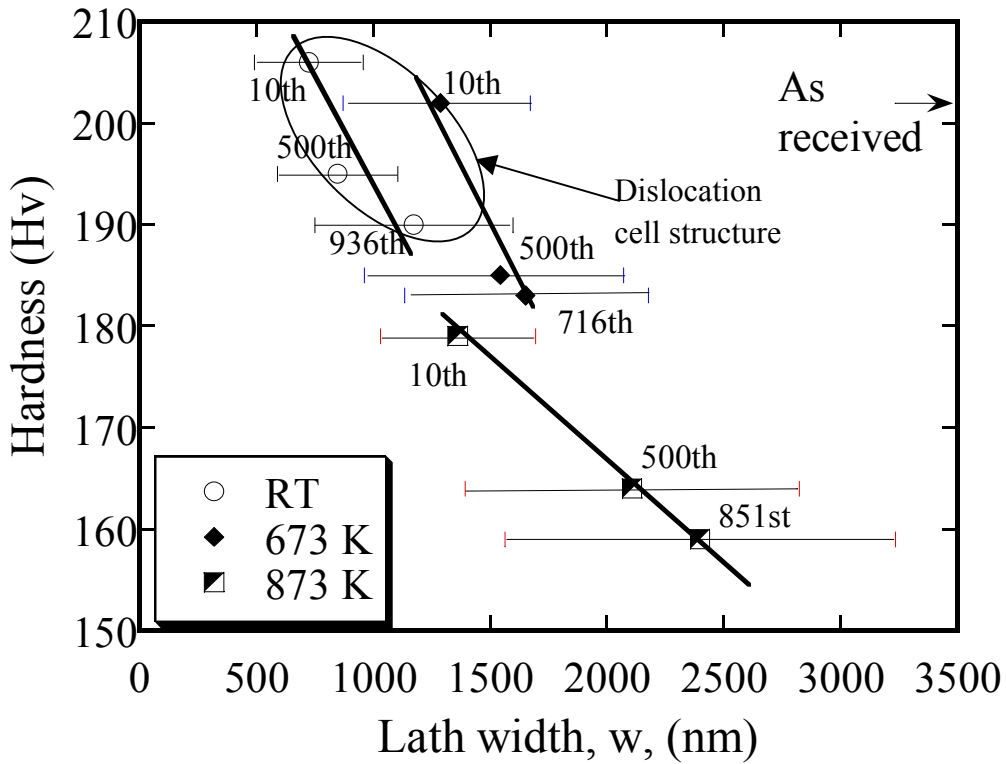


Fig. 4.3-1 Relationship between hardness and lath width at $\Delta\epsilon_t=1.8\%$ at RT, 673 K and 873 K.

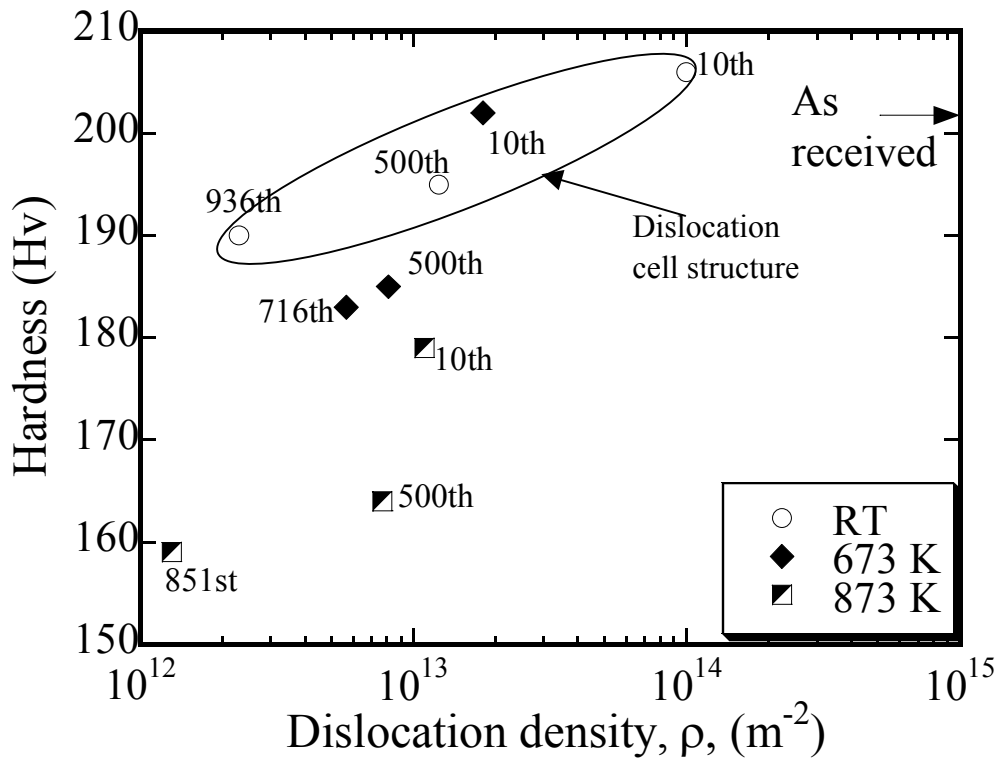


Fig. 4.3-2 Relationship between hardness and dislocation density at $\Delta\epsilon_t=1.8\%$ at RT, 673 K and 873 K.

According to reference [104], the relationship between hardness (Hv) and yield stress (σ_y) will be expressed as follows;

$$Hv = C\sigma_y \propto \sigma_y \quad , \quad (4.3-1)$$

where C is about 3.

According to dislocation theory, the contribution of change in dislocation density (ρ) to the change in yield stress can be expressed as Orowan type equation [95, 96],

$$\Delta\sigma_y = \beta\alpha\mu b\Delta\sqrt{\rho} \propto \Delta\sqrt{\rho} \quad , \quad (4.3-2)$$

where β is Talor factor (about 3), α is barrier factor, μ is shear modules, and b is Bergers vector.

The contribution of change in grain size (D) to the change in yield stress can be expressed as Hall-Petch's equation [95, 96],

$$\Delta\sigma_y = k\Delta\frac{1}{\sqrt{D}} \propto \Delta\frac{1}{\sqrt{D}} \quad , \quad (4.3-3)$$

where is k material constant.

For rough estimation, D is substituted by w (lath width), or D is substituted by d (dislocation cell size). So, the contribution from lath and dislocation cell can be estimated as follows.

$$\Delta\sigma_y \propto \Delta\frac{1}{\sqrt{w}} \quad . \quad (4.3-3a)$$

$$\Delta\sigma_y \propto \Delta\frac{1}{\sqrt{d}} \quad . \quad (4.3-3b)$$

Thus, change in hardness (ΔHv) can be express as

$$\Delta Hv = \alpha_1(\Delta\sqrt{\rho}) + \alpha_2(\Delta\frac{1}{\sqrt{w}}) + \alpha_3(\Delta\frac{1}{\sqrt{d}}) \quad , \quad (4.3-4)$$

where α_1 , α_2 and α_3 are constant.

In the present study, ΔHv , $\Delta\sqrt{\rho}$, $\Delta\frac{1}{\sqrt{w}}$ and $\Delta\frac{1}{\sqrt{d}}$ were calculated from the fatigued

specimen and as received JLF-1 steel.

$$\Delta H_{v_i} = H_{v_i} - H_{v_0} \quad , \quad (4.3-5a)$$

$$(\Delta\sqrt{\rho})_i = \sqrt{\rho_i} - \sqrt{\rho_0} \quad , \quad (4.3-5b)$$

$$\left(\Delta\frac{1}{\sqrt{w}}\right)_i = \frac{1}{\sqrt{w_i}} - \frac{1}{\sqrt{w_0}} \quad , \quad (4.3-5c)$$

$$\left(\Delta\frac{1}{\sqrt{d}}\right)_i = \frac{1}{\sqrt{d_i}} - \frac{1}{\sqrt{d_0}} \quad , \quad (4.3-5d)$$

where subscript i means the data taken from the fatigued specimen, subscript 0 means the data taken from the as received material. For the case of no dislocation cell structure, the equation (4.3-5d) is assumed to be zero.

Based on at least square theory, the relationship between change in hardness and dislocation density, lath width and dislocation cell structure size can be expressed as follows:

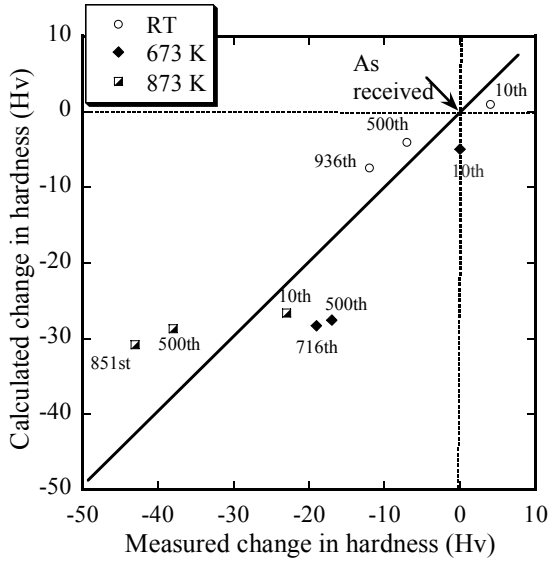
(1) Cell structure existing

$$\Delta H_v = 1.0 \times 10^{-6} (\Delta\sqrt{\rho}) + 9.1 \times 10^{-3} \left(\Delta\frac{1}{\sqrt{w}}\right) + 1.9 \times 10^{-2} \left(\Delta\frac{1}{\sqrt{d}}\right) \quad (4.3-6a)$$

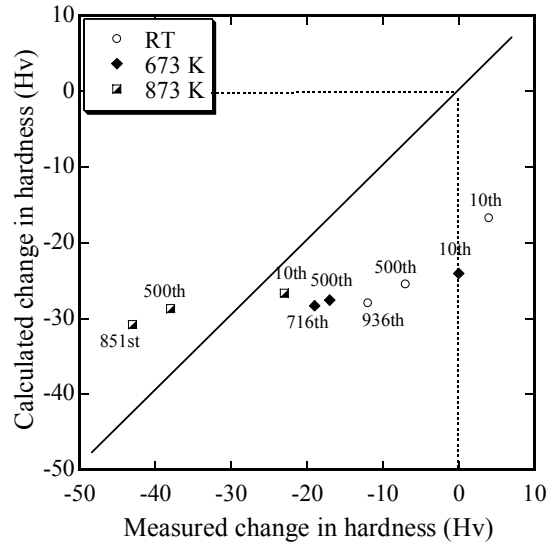
(2) No cell structure

$$\Delta H_v = 1.0 \times 10^{-6} (\Delta\sqrt{\rho}) + 9.1 \times 10^{-3} \left(\Delta\frac{1}{\sqrt{w}}\right) \quad (4.3-6b)$$

Fig. 4.3-3 (a) shows relationship between the measured and calculated change in hardness, all data can be fit to equation (4.3-6a) and (4.3-6b). The dislocation cell structure has a significant effect on change in hardness. There would be a big difference in measured and calculated data of existing cell structure when the effect of dislocation cell size were omitted (Fig. 4.3-3(b)).



(a) Dislocation cell structure is considered.



(b) Cell structure is not considered.

Fig. 4.3-3 Comparison of calculated and measured change in hardness.

4.4 Summary

Low cycle fatigue tests of JLF-1 steel was carried out at strain rate of 0.1%/s in vacuum at RT, 673 K and 873 K. Results are summarized as follows

- The fatigue life of JLF-1 steel is independent on temperature when plotted against the total strain range. The $\Delta \varepsilon_t - N_f$ regression curves of JLF-1 are expressed as follows:

$$673 \text{ K: } \Delta \varepsilon_t = 37.05 N_f^{-0.4746} + 0.7209 N_f^{-0.08571}$$

$$873 \text{ K: } \Delta \varepsilon_t = 36.05 N_f^{-0.4382} + 0.3809 N_f^{-0.06148}$$

The fatigue life of JLF-1 is almost as same as that of F82H at elevated temperature.

- The fatigue life curves of JLF-1 at RT, 673 K and 873 K were on different lines when plotted against the plastic strain range. This is not in agreement with Coffin's model. The loss of strain hardening will be responsible for the increase of fatigue life at high temperature when plotted against the plastic strain range.
- Cyclic softening was observed during fatigue test at RT, 673 K and 873 K. TEM analysis showed cyclic softening is caused by reduction of dislocation density, formation and loss of dislocation cell structure, and increment of lath width.
- The relationship between change in hardness and microstructure of JLF-1 steel can be expressed as follows.

(1) Cell structure existing

$$\Delta H_v = 1.0 \times 10^{-6} (\Delta \sqrt{\rho}) + 9.1 \times 10^{-3} \left(\Delta \frac{1}{\sqrt{w}} \right) + 1.9 \times 10^{-2} \left(\Delta \frac{1}{\sqrt{d}} \right)$$

(2) No cell structure

$$\Delta H_v = 1.0 \times 10^{-6} (\Delta \sqrt{\rho}) + 9.1 \times 10^{-3} \left(\Delta \frac{1}{\sqrt{w}} \right).$$

Chapter 5 Consideration for design base

According to ASME Boiler and Vessel Code, Sec.III, there is a stress limit for design which linear elastically calculated stress should not exceed. Thus, the deformation of system remains in elasticity. However, when the earthquake happens and/or strain concentration occurs, the stress will be beyond the allowable stress, the elastic-plastic properties of material must be considered.

5.1 Effect of strain hardening on the design base

Material deformation behavior is one of the important information for blanket design [105, 106]. Thus, it is necessary to consider the effect of strain hardening on plastic design analysis as the strain hardening shows the deformation resistance when the applied stress exceeds the yield stress.

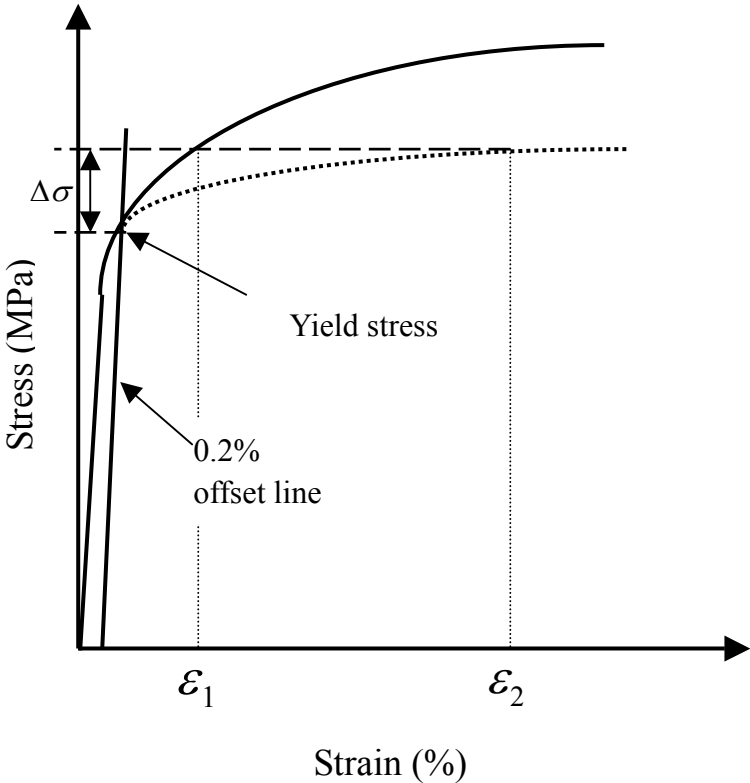


Fig. 5.1-1 Relation between the strain hardening and deformation.

The effect of strain hardening on deformation is shown in Fig. 5.1-1. When stress is

about $\Delta\sigma$ higher than the yield stress, the deformation is dependent on the strain hardening. In the case of strong strain hardening (solid line in Fig 5.1-1), the deformation is ε_1 ; in the case of weak strain hardening (dot line in Fig 5.1-1), the deformation is ε_2 . It is clear that the smaller in strain hardening will cause larger deformation when the external stress is beyond the yield stress.

Since strain hardening of JLF-1 decreased rapidly at 773 K and 873 K, the plastic deformation design should be careful.

5.2 Effect of cyclic softening on the fatigue design base

For unexpected dynamic service condition, such as earthquake, analysis of system in terms of strain is appreciate. Strain controlled low cycle fatigue tests are meant to indicate whether the plastic deformation during cyclic loading should be admissible. As mentioned in section 4, cyclic softening occurred in the LCF test of JLF-1 steel, which will reduce the deformation resistance.

Fig. 5.2-1 shows the static stress-strain curves of tensile test and the hysteresis curves of LCF tests at around half life at 673 K. According to reference [83], if the peak tensile stresses in hysteresis curves were connected, the cyclic stress-strain curve could be obtained.

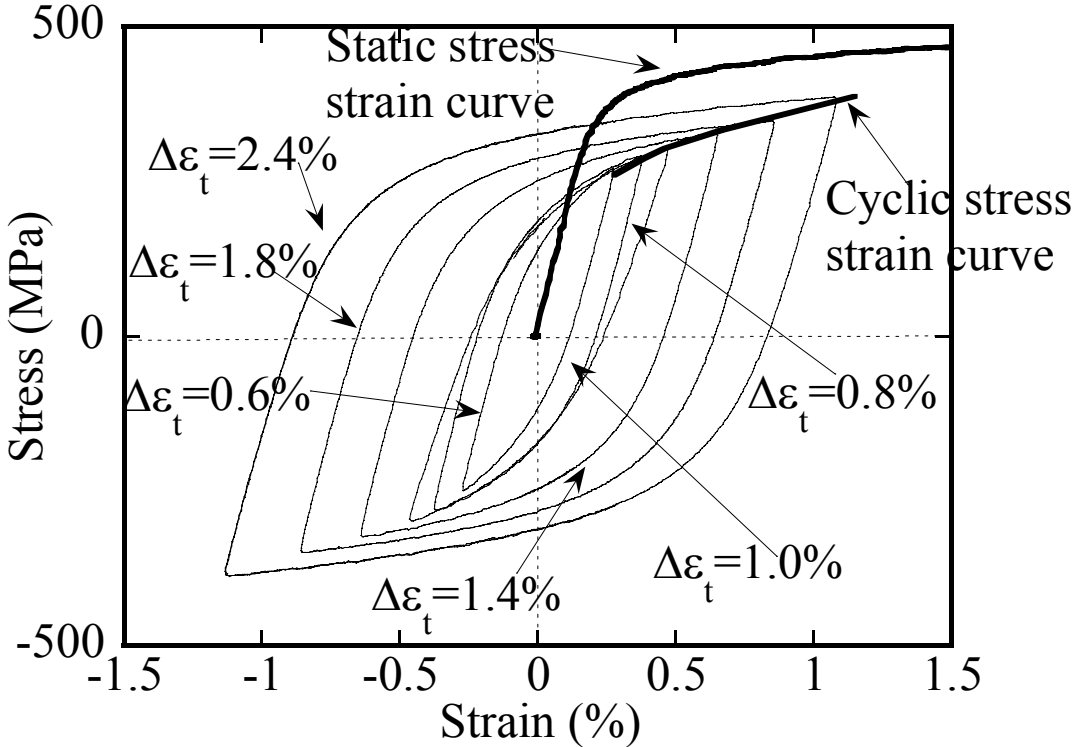


Fig. 5.2-1 Tensile stress-strain curve and fatigue hysteresis curves at around half life at 673 K.

The static and cyclic stress-strain curves of JLF-1 steel at RT, 673 K and 873 K are shown in Fig. 5.2-2. Due to cyclic softening, the cyclic curve was lower than the static one at elevated temperature. The difference between the static and cyclic curves increased with

temperature. Especially at 873 K, same as in the tensile test, there was little strain hardening in the cyclic stress-strain curve. Similar to tensile test, if a cyclic yield stress point was defined as 0.2% strain off-set stress point from zero of cyclic stress-strain curves, the cyclic yield stress could be determined.

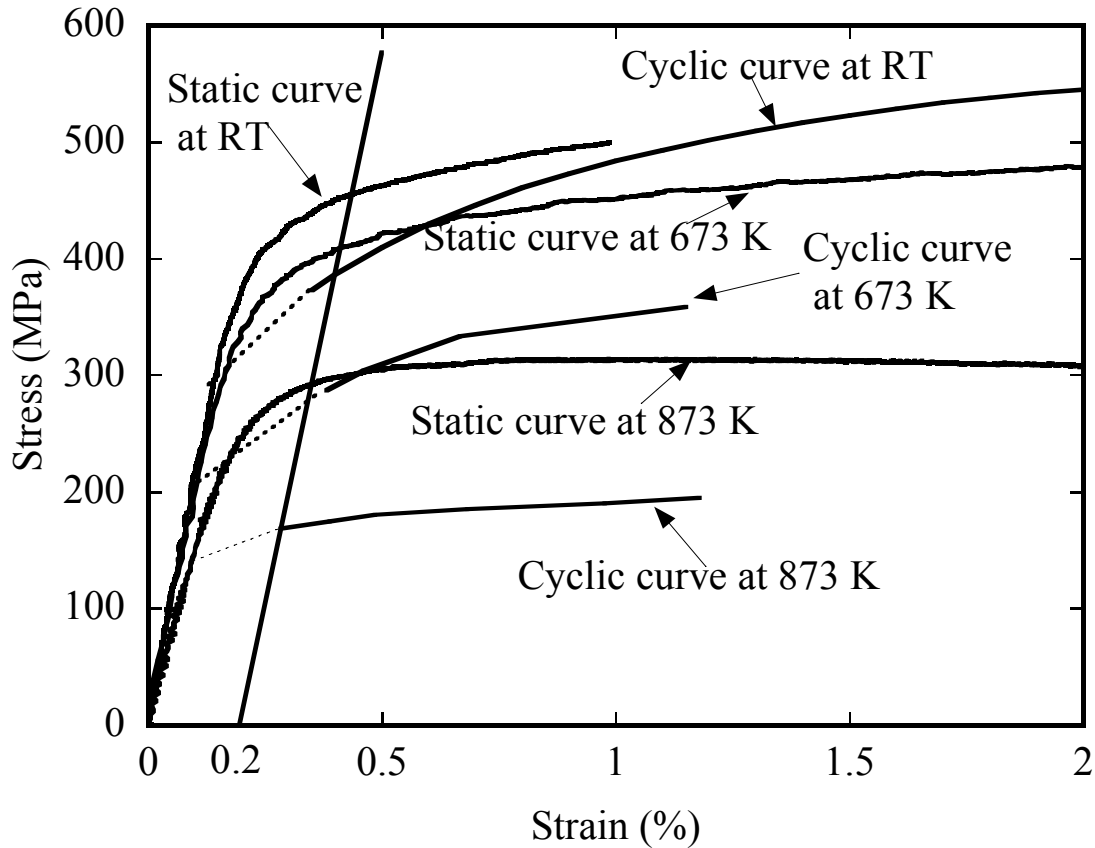


Fig. 5.2-2 Static and cyclic stress-strain curves at RT, 673K and 873K.

In reference [75], a stress for design, S_m , is defined, which is given for instance by

$$S_m = \min \left\{ \frac{2}{3} \sigma_y, \frac{1}{3} \sigma_{UTS} \right\}. \quad (5.2-1)$$

The allowable stresses are

$$P_m \leq S_m. \quad (5.2-2)$$

Based on the equation 5.2-1, the stress for design of JLF-1 steel at elevated temperature could be calculated from Fig. 3.1.1-3.

Fig. 5.2-3 shows the change in static yield stress, cyclic yield stress and stresses for design of JLF-1 steel against the temperature. The reduction in design margin is significant

when the cyclic softening happens in cyclic deformation. In practical structure, the combined the mechanical and thermal cyclic stresses may exceed the stress for design. From the viewpoint of static deformation analysis, the structure is safety if the exceeding stress is below the static yield stress curve. But as a result of cyclic softening, when the exceeding stress is over cyclic yield stress curve even it is still below the static yield stress curve, the structure will be deformed. If the exceeding in stress happened at 873 K, as there is little strain hardening, the deformation will cause disaster.

Thus, the phenomenon of cyclic softening and decrease in strain hardening of JLF-1 steel is a critical issue for design; the cyclic yield stress curve is a base for design and safety analysis. The design stress of $\frac{\sigma_{UTS}}{3}$ is acceptable at 873 K.

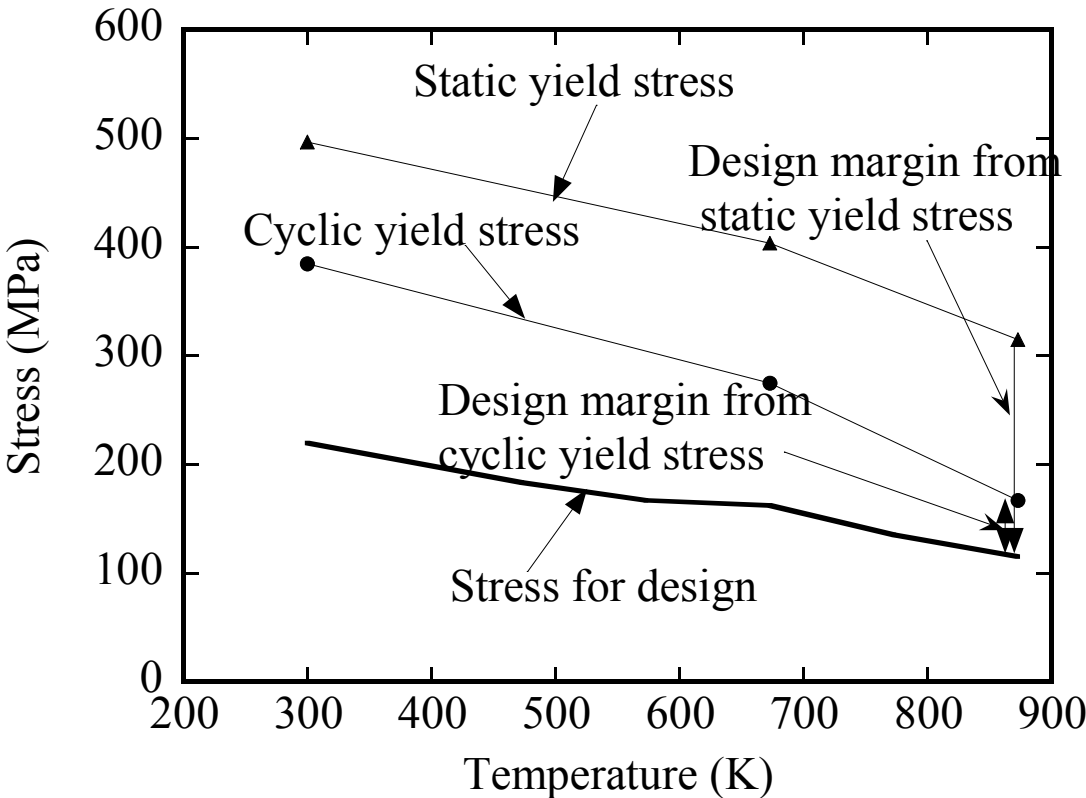


Fig. 5.2-3 Change in static yield stress, cyclic yield stress and stresses for design of JLF-1 steel against the temperature.

5.4 Summary

- Smaller in strain hardening will cause larger deformation when the external stress is beyond the yield stress. The plastic design of JLF-1 steel at 773 K and 873 K should be careful.
- The phenomenon of cyclic softening of JLF-1 steel is a critical issue for design, which will cause the reduction in design margin significantly. The cyclic yield stress curve is a base for design and safety analysis. The design stress of $\sigma_{UTS}/3$ is acceptable at 873 K.

Chapter 6 Conclusions

Development of reactor materials and power generating blankets is a critical issue for early realization of fusion energy. Among the three kinds of materials for fusion applications (RAF/M, V-alloy, and SiC/SiC), the RAF/M steel is considered as the leading candidate structural material for the first wall in fusion reactor. The low cycle fatigue properties at elevated temperature are the basic for design of blanket components. The objective of this research is to study the LCF behavior of a candidate material of the first wall, JLF-1 steel, at elevated temperature with engineering size specimens in vacuum. To obtain basic information of RAF/M at elevated temperature, the tensile test was also carried out.

The tensile tests and microstructure analysis of JLF-1 steel at strain rate of 0.1%/s and 0.02%/s were conducted from RT to 873 K to investigate the material static deformation behavior. The results were concluded as:

- The strain rate does not affect YS, UTS and RA as far as the tests performed in this study. The tensile property of JLF-1 steel is comparable to that of F82H at elevated temperature.
- Strain hardening of JLF-1 steel decreased significantly above 673 K, causing little difference of YS to UTS at 873 K. The mechanism is considered as the climbing of edge dislocation and cross gliding of screw dislocation become dominant at high temperature. As the smaller in strain hardening will cause larger deformation when the external stress is beyond the yield stress, the plastic deformation design at 773 K and 873 K should be careful.
- With strain hardening decreased, RA also increased rapidly above 673 K; and the surface fractography was changed from shear fracture below 673 K to dimple fracture at 773 K and 873 K. That means JLF-1 steel becomes near to be a perfect elastic-plastic body (smaller strain hardening) and ductility improved with temperature increase.

LCF tests of JLF-1 steel with total strain of $\Delta\varepsilon_t=0.6\%\sim 2.4\%$ were carried out in vacuum under a fully reversed push–pull triangular wave with strain rate of 0.1 %/s at RT, 673 K, and 873 K. Results are concluded as follows:

- The fatigue life of JLF-1 steel is independent of temperature when plotted against the total strain range. The $\Delta\varepsilon_t-N_f$ regression curves of JLF-1 are expressed as follows:

$$673 \text{ K: } \Delta\varepsilon_t = 37.05 N_f^{-0.4746} + 0.7209 N_f^{-0.08571}$$

$$873 \text{ K: } \Delta\varepsilon_t = 36.05 N_f^{-0.4382} + 0.3809 N_f^{-0.06148}$$

The fatigue life of JLF-1 is almost as same as that of F82H at elevated temperature.

- The fatigue life curves of JLF-1 at RT, 673 K and 873 K were on different lines when plotted against the plastic strain range. This is not in agreement with Coffin's model. The loss of strain hardening will be responsible for the increase of fatigue life at high temperature when plotted against the plastic strain range.
- Cyclic softening was observed during fatigue test at RT, 673 K and 873 K. TEM analysis showed cyclic softening is caused by reduction of dislocation density, formation and loss of dislocation cell structure, and increment of lath width.
- The relationship between change in hardness and microstructure of JLF-1 steel can be expressed as follows.

(1) Cell structure existing

$$\Delta H_v = 1.0 \times 10^{-6} (\Delta \sqrt{\rho}) + 9.1 \times 10^{-3} \left(\Delta \frac{1}{\sqrt{w}} \right) + 1.9 \times 10^{-2} \left(\Delta \frac{1}{\sqrt{d}} \right)$$

(2) No cell structure

$$\Delta H_v = 1.0 \times 10^{-6} (\Delta \sqrt{\rho}) + 9.1 \times 10^{-3} \left(\Delta \frac{1}{\sqrt{w}} \right)$$

- The cyclic yield stress curve is a base for design and safety analysis. The design stress of $\frac{\sigma_{UTS}}{3}$ is acceptable for JLF-1 steel.

REFERENCE

- [1] J. Goldemberg, Energy Policy, 32 (2004) 711-714.
- [2] D. L. Klass, Energy Policy, 31 (2003) 353-367.
- [3] R. Toschi, Fus. Engin. Des. 36 (1997) 1-8.
- [4] Everett E. Bloom, J. Nucl. Mater. 258-263 (1998) 7-17
- [5] ITER homepage [http:// www.iter.org](http://www.iter.org).
- [6] The promise of fusion energy, http://fusioned.gat.com/images/pdf/promise_of_fusion.pdf.
- [7] D. Finkenthal, R. Lee, S. Rodecker, et al, Fusion — Nature's Fundamental Energy Source, General Atomics, 1996
- [8] C. C. Baker, R. W. Conn, F. Najmabadi, et al, Energy, Vol.23 (7/8) 1998 649-694.
- [9] Jiming Chen, Doctor thesis 2005, The Graduate University for Advanced Studies.
- [10] Zhenyu Yao, Doctor thesis 2005, The Graduate University for Advanced Studies.
- [11] C. Neumeyer, P. Heitzenroeder, C. Kessel, et al, Fus. Engin. Des. 66-68 (2003) 139-145.
- [12] M. D. Williams, Fus. Engin. Des. 36 (1997) 135-142.
- [13] E. Bertolini, Fus. Engin. Des. 36 (1997) 119-133.
- [14] J. P. Sharpe, P.W. Humrickhouse, C.H. Skinner, et al, J. Nucl. Mater. 337-339 (2005) 1000-1004.
- [15] Y. Shimomura, Fus. Engin. Des. 81 (2006) 3-11.
- [16] E. Di Pietro, R. Andreani, D. Maisonnier, et al, Fus. Engin. Des. 81 (2006) 59-67.
- [17] M. Mori, Fus. Engin. Des. 81 (2006) 69-77.
- [18] V.A. Belyakov, Fus. Engin. Des., 81 (2006) 79-86.
- [19] N. R. Sauthoff, Fus. Engin. Des., 81 (2006) 87-92.
- [20] K.M. Feng, C.H. Pan, G.S. Zhang ,et al, Fus. Engin. Des. 81 (2006) 1219-1224.
- [21] R. Aymar, J. Nucl. Mater. 307-311 (2002) 1-9.
- [22] R. Aymar, Fus. Eng. Des. 61-62 (2002) 5-12.
- [23] Y. Shimomura, J. Nucl. Mater. 329-333 (2004) 5-11.
- [24] M. Seki, M. Guseva, G. Vieider, et al, J. Nucl. Mater. 179-181 (1991) 1189-1192.
- [25] F. Elio, K. Ioki, L. Bruno, et al, Progress in the ITER Blanket Design, http://www-ferp.ucsd.edu/raffray/publications/SOFE/17_SOFE_Elio.pdf.

- [26] A. R. Raffray, M. Akiba, V. Chuyanov et al, J. Nucl. Mater. 307-311 (2002) 21-30.
- [27] G. Kalinin, V. Barabash, S. Fabristiev, et al, Fus. Engin. Des. 55 (2001) 231-246.
- [28] G. Kalinin, W. Gauster, R. Matera, et al, J. Nucl. Mater. 233–237 (1996) 9-16.
- [29] T. Muroga, T. Tanaka, S. Sagara, Fus. Engin. Des. 81 (2006) 1203-1209.
- [30] L.V. Boccaccini, L. Giancarli, G. Janeschitz, et al, J. Nucl. Mater. 329-333 (2004) 148-155.
- [31] M. Enoeda, M. Akiba, S. Tanaka, et al, Fus. Eng. Des. 81 (2006) 415-424.
- [32] F. Najmabadi, Fus. Engin. Des. 41 (1998) 365-370.
- [33] K. Ehrlich, E.E. Bloom, T. Kondo, J. Nucl. Mater. 283-287 (2000) 79-88.
- [34] D. L. Smith, C. C. Baker, D. K. Sze, et al, Fus. Tech. 8 (1985) 10-44.
- [35] R. L. Klueh, D. R. Harries, High-Chromium Ferritic and Martensitic Steels for Nuclear Application, ASM Stoch, Number: Mono 03.
- [36] R. L. Klueh, K. Ehrlich and F. Abe, J. Nucl. Mater. 191–194 (1992) 116-124.
- [37] S.J.Zinkle, M.Victoria and K.Abe, J. Nucl. Mater. 307-311(2002) 31-42.
- [38] K. Ehrlich, Fus. Engin. Des., 56-57 (2001) 71-82.
- [39] Zhang Wen, Doctor thesis 1999, CIAE Beijing.
- [40] B. van der Schaaf, E. Diegele, R. Laesser, et al, Fus. Engin. Des. 81(2006) 893-900.
- [41] T. Muroga, M. Gasparotto, S.J. Zinkle, Fus. Engin. Des. 61-62 (2002) 13-25.
- [42] T.Muroga, T.Nagasaka, K.Abe, et al, J. Nucl. Mater. 307-311 (2002) 547-554.
- [43] R.J. Kurtz, K.Abe, VM Chernov, et al, J. Nucl. Mater. 329-333 (2004) 47-55.
- [44] J.M. Chen, T.Muroga, W.G. Huang, et al, , J. Nucl. Mater. 329-333 (2004) 401-405.
- [45] E.E. Bloom, S.J. Zinkle, F.W. Wiffen, J. Nucl. Mater. 329-333 (2004) 12-19.
- [46] R.L.Klueh, D.S.Gelles, S.Jitsukawa, et al, J. Nucl. Mater. 307-311(2002) 455-465.
- [47] S.Jitsukawa, A.Kimura, A.Kohyama et al, J. Nucl. Mater. 329-333 (2004) 39-46.
- [48] K.Shiba, M.Enoeda, S.Jitsukawa. J. Nucl. Mater. 329-333 (2004) 243-247.
- [49] M. Sato, Y. Miura, S. Takeji, et al, J. Nucl. Mater. 258-263 (1998) 1253-1258.
- [50] T. Nakayama, M. Abe, T. Tadokoro, et al, J. Nucl. Mater. 271-272 (1999) 491-495.
- [51] D. R. Harries, G. J. Butterworth, A. Hishinuma, et al, J. Nucl. Mater. 191-194 (1992) 92-99.
- [52] A. Kohyama, A. Hishinuma, D. S. Gelles, et al, J. Nucl. Mater. 233-237 (1996) 138-147.

- [53] R. L. Klueh, D. J. Alexander, *J. Nucl. Mater.* 233-237 (1996) 336-341.
- [54] A. Kimura, M. Narui, T. Misawa, et al, *J. Nucl. Mater.* 258-263 (1998) 1340-1344.
- [55] M. Tamura, H. Hayakawa, M. Tanimura, et al, *J. Nucl. Mater.* 141–143 (1986) 1067-1073.
- [56] M. Tamura, H. Hayakawa, A. Yoshitake, et al, *J. Nucl. Mater.* 155–157 (1988) 620-625.
- [57] A. Kohyama, Y. Kohno, K. Asakura, et al, *J. Nucl. Mater.* 212–215 (1994) 684-689.
- [58] A. Kohyama, Y. Kohno, M. Kuoda, et al, *J. Nucl. Mater.* 258–263 (1998) 1319-1323.
- [59] K. Ehrlich, S. Kelzenberg, H. -D. Röhrig, et al, *J. Nucl. Mater.* 212–215 (1994) 678-683.
- [60] R. L. Klueh, D. S. Gelles, A. Lechtenberg, *J. Nucl. Mater.* 141–143 (1986) 1081-1087.
- [61] A. Alamo, J. C. Brachet, A. Castaing, et al, *J. Nucl. Mater.* 258–263 (1998) 1228-1235.
- [62] J. Pan, J. Tong, M. Tian, *Fundamental of Material Science*, Tsinghua Univ. Press., Beijing 1998.
- [63] M. Ahlers, *The Martensitic Transformation*, *Revista Matéria*, 9 (2004) 169-183.
- [64] K. Shiba, A. Hishinuma, A. Tohyama, et al, *JEARI-Tech* 97-038.
- [65] S. Jitsukawa, M. Tamura, B. van der Schaaf, et al, *J. Nucl. Mater.* 307-311 (2002) 179-186.
- [66] A. -A. F. Tavassoli, J. -W. Rensman, M. Schirra, et al, *Fus. Engin. Des.* 61-62 (2002), 617-628.
- [67] R. Lindau, M. Schirra, *Fus. Engin. Des.* 58-59 (2001), 781-785.
- [68] R. Lindau, A. Moslang, M. Schirra, *Fus. Engin. Des.* 61-62 (2002), 659-664.
- [69] P. Fernandez, A.M. Lancha, J. Lapena, et al, *Fus. Engin. Des.* 58-59 (2001), 787-792.
- [70] Y. Kohno, A. Kohyama, T. Hirose, et al, *J. Nucl. Mater.* 271-272 (1999) 145-150.
- [71] F. Abe, S. Nakazawa, *Metall. Trans. A*, Vol.23A, Nov. 1992, 3025-3034.
- [72] M. Klesnil, P. Lukas, *Fatigue of metallic materials*, Elsevier scientific publishing company 1980.
- [73] L. F. Coffin, *Proc. Instn. Mech. Engrs.*, Vol 188 (1974) 109-126.
- [74] J. Wareing, A.-A. Tavassoli, *SmiRT-13*, Porto Alegre, Brazil, Aug. 13-18, 1995, 563-574.
- [75] D. Munz, E. Diegele, *Fus. Engin. Des.* 16 (1991) 45-57.
- [76] C. Petersen, *J. Nucl. Mater.* 258–263 (1998) 1285-1290.
- [77] A. Ziemann, V. Rybin, C. Petersen, et al, *J. Nucl. Mater.* 264 (1999) 234.
- [78] A.F. Armas, C. Petersen, R. Schumitt, et al, *J. Nucl. Mater.* 307-311 (2002) 509-513.

- [79] G. Filacchioni, E. Casagrande, U. De Angelis, et al, J. Nucl. Mater. 329-333 (2004) 263-267.
- [80] L. A. Belyaeva, A. A. Zisman. C. Petersen, et al, J. Nucl. Mater. 283-287 (2000) 461-464.
- [81] T. Ishii, K. Fukaya, Y. Nishiyama, et al, J. Nucl. Mater. 258–263 (1998) 1183-1186.
- [82] J.F. Stubbins, D.S. Gelles, J. Nucl. Mater. 233-237 (1996) 331-335.
- [83] A. Nishimura, T. Nagasaka. N. Inoue, et al, J. Nucl. Mater. 283-287 (2000) 677-680.
- [84] T. Hirose, H. Sakasegawa, A. Kohyma, et al, J. Nucl. Mater. 283-287 (2000) 1018-1012.
- [85] H. Sakasegawa, T. Hirose, A. Kohyma, et al, Fus. Eng. Des., 61-62 (2002) 671-6765.
- [86] A. F. Armas, M. Avalos, I. A. Armas, et al, J. Nucl. Mater. 258-263 (1998) 1204-1208.
- [87] H. Tanigawa, T. Hirose, M. Ando, et al, J. Nucl. Mater. 307-311 (2002) 293-298.
- [88] H.K. Yoon, S.P. Lee, B.H. Min, et al, Fus. Eng. Des., 61-62 (2002) 677-682.
- [89] ASTM E 8M-00, Annual book of ASTM, ASTM, Philadelphia
- [90] ASTM E 21-92, Annual book of ASTM, ASTM, Philadelphia.
- [91] ASTM E 606-92, Annual book of ASTM, ASTM, Philadelphia.
- [92] A. -A. F. Tavassoli, J. Nucl. Mater. 258-263 (1998) 85-96.
- [93] A. Nishimura, N. Inoue, T. Muroga, J. Nucl. Mater. 258-263 (1998) 1242-1247.
- [94] K. Shiba, T. Hirose, Fus. Eng. Des., 81 (2006) 1051-1055.
- [95] Q. Li, Mater. Sci. and Engin., A 361 (2003) 385-391.
- [96] T. Nagasaka, H. Yoshida, K. Fukumoto, et al, Mater. Trans., JIM, 41 (2000) 170-177.
- [97] N. Inoue, T. Muroga, A. Nishimura, et al., J. Nucl. Mater. 258-263 (1998) 1248-1252.
- [98] ASTM, Manual on Fitting Straight Lines, STP 313, ASTM, 1962.
- [99] A. F. Armas, C. Peterson, R. Schmitts, et al, J. Nucl. Mater. 329–333 (2004) 252-256.
- [100] J. Pesika, R. Kluzer, A. Dronhofer, et al, Acta materialia 51 (2003) 4847-4862.
- [101] N. Mebarki, D. Delagnes, P. Lamesle, et al, Mater. Sci. and Engin. A 387-389 (2004) 171-175.
- [102] H. J. Chang and J. J. Kai, J. Nucl. Mater. 191–194 (1992) 836-840.
- [103] Y. Ei-Madhoun, A. Mohamed, M. N. Bassim, Mater. Sci. and Engin. A 359 (2004) 220-227.
- [104] J. T. Busby, M. C. Hash, G. S. Was, J. Nucl. Mater. 336 (2005) 267-278.
- [105] A. –A. F. Tavassoli, J. Nucl. Mater. 302 (2002) 73-88.

[106] Y. I. Moon, *Fus. Eng. Des.*, 65 (1981) 431-436.

LIST of PAPERS

1. H. LI, A. NISHIMURA, Z. LI, T. NAGASAKA, T. MUROGA, Low Cycle Fatigue Behavior of JLF-1 Steel at Elevated Temperature, *Fusion Engineering and Design*, 81 (2006) 241-245
2. H. LI, A. NISHIMURA, T. MUROGA, T. NAGASAKA, Microstructural Analysis on JLF-1 Steel Tested by Fatigue Deformation, *Journal of Nuclear Materials*, to be published.
3. H. LI, A. NISHIMURA, T. NAGASAKA, T. MUROGA, Stress-Strain Behavior on Tensile and Low Cycle Fatigue Tests of JLF-1 Steel at Elevated Temperature in Vacuum, *Fusion Engineering and Design*, to be published.
4. H. LI, A. NISHIMURA, T. MUROGA, T. NAGASAKA, Fatigue Life and Cyclic Softening Behavior of JLF-1 Steel, *Fusion Engineering and Design*, to be published.

LIST OF PRESENTATION

1. H. LI, A. NISHIMURA, T. NAGASAKA, T. MUROGA, Low Cycle Fatigue Behavior of JLF-1 Steel at High Temperature in Vacuum, 8th Japan-China Symposium on Materials for Advanced Energy Systems and Fission & Fusion Engineering (JCS-8), Oct. 4-8, 2004, Sendai, Japan.
2. H. LI, A. NISHIMURA, Z. LI, T. NAGASAKA, T. MUROGA, Low Cycle Fatigue Behavior of JLF-1 Steel at Elevated Temperature, 7th International Symposium on Fusion Nuclear Technology (ISFNT-7), May 22-27, 2005, Tokyo, Japan.
3. H. LI, A. NISHIMURA, T. MUROGA, T. NAGASAKA, Microstructure Analysis on JLF-1 Steel Tested by Tensile and Fatigue Deformation, 12th International Conference on Fusion Reactor Materials (ICFRM-12), Dec. 4-9, 2005, Santa Barbara, California, USA.
4. H. LI, A. NISHIMURA, T. NAGASAKA, T. MUROGA, Stress- Strain Behavior on Tensile and Low Cycle Fatigue Tests of JLF-1 Steel at Elevated Temperature in Vacuum, 15th International Toki Conference “ Fusion & Advanced Technology”, Dec. 6-9, Toki, Japan.
5. H. LI, A. NISHIMURA, T. NAGASAKA, T. MUROGA, Study on the Tensile Behavior of JLF-1 Steel at Elevated Temperature in Vacuum, 第6回核融合エネルギー連合講演会, 2006年6月13-14日, 富山, 日本.
6. H. LI, A. NISHIMURA, T. MUROGA, T. NAGASAKA, Fatigue Life and Cyclic Softening Behavior of JLF-1 Steel, 24th Symposium on Fusion Technology, 11th -15th Sept., 2006, Warsaw, Poland.

ACKNOWLEDGEMENTS

At first, I would like to express the appreciation to my supervisor — Prof. Arata NISHIMURA, of National Institute for Fusion Science (NIFS) and The Graduate University of Advanced Studies (Sokendai) in Japan, for his aborative guidance and elaborate discussions on my study, and kindly helps on my living in Japan.

I am thankful to Prof. Takeo MUROGA and Associated Prof. Takuya NAGASAKA of NIFS for their guided advices and powerful helps on this study.

I am also thankful Prof. Jiming Chen of South West Institute of Plasma for his kindly helps and comments in my studying and living.

I wish to thanks Prof. N. Noda of NIFS for his guided comments, and Dr. Tanaka and Mr. Sugito of NIFS for their great helps and collaborations on this study. I also express my thanks to other member of Fusion Engineering Research Center (FERC) of NIFS for their kindly helps.

I also thank Mr. K. Matsuura, Ms. S. Urushihara, Mr. A. Hibino and Ms. K. Mizuno of NIFS for their studio work to Sokendai affairs.

I am also thankful to Dr. LI Baiwen, Dr. Yao Zhenyu, Mr. LI Zaixin, Mr. XU Qi and Mr. LI Bin as classmates of Sokendai for their helps and friendships.

Finally, I would like to express the best appreciations to my wife (FENG Minjuan) and son (LI Zhiyu) for their support with endless love during my Ph.D study for three years.

Huailin LI
Sept. 15, 2006